Washington University in St. Louis

Washington University Open Scholarship

All Theses and Dissertations (ETDs)

January 2009

Aerosol Filtration And Separation

Tachih Hsiao
Washington University in St. Louis

Follow this and additional works at: https://openscholarship.wustl.edu/etd

WASHINGTON UNIVERSITY IN ST. LOUIS

School of Engineering and Applied Science

Department of Energy, Environmental & Chemical Engineering

Dissertation Examination Committee
Pratim Biswas, Chair
Ramesh Agarwal
Richard L. Axelbaum
Da-Ren Chen, Advisor
Jay R. Turner
David Y.H. Pui

AEROSOL FILTRATION AND SEPARATION

by

Ta-Chih Hsiao

A dissertation presented to the
Graduate School of Arts and Sciences
of Washington University in
partial fulfillment of the
requirements for the degree
of Doctor of Philosophy

July. 2009

Saint Louis, Missouri

ABSTRACT OF THE DISSERTATION

Aerosol Filtration and Separation

by

Ta-Chih Hsiao

Doctor of Philosophy in Energy, Environmental, & Chemical Engineering

Washington University in St. Louis, 2009

Professor Da-Ren Chen, Advisor

Particle control technologies are essential in many manufacturing industries (chemical, electronic, mineral, and food and beverages) as well as in pollution abatement and environmental control (for example, clean rooms and post processing of power plant emissions). A variety of particle control technologies using different physical forces and various collection substrates have been developed over the last 100 or so years. Among these technologies, filtration is known as the most economical means for submicron aerosol particles with low concentration, and cyclones are superior to other devices for supermicron particles with high concentration. The overall objective of this dissertation is to advance our current knowledge on these two particle control technologies. Accordingly, it has two major topics: (1) Aerosol Filtration – Liquid-coated Particle Loading, and (2) Inertial Separation – Axial Flow Cyclone. For the first part, Aerosol Filtration, a system which is able to generate stable liquid-coated particles is developed, and series of filter loading experiments are performed to study the behavior of filters loaded with liquid-coated particles, which exhibit transition behavior between those of

solid and those of liquid particles. Different effects, including filter media, coated particle size, and coating liquid properties, on the transition behavior are explored. Moreover, an empirical model for predicting the loading curves for particles coated with liquids of different viscosity is proposed. For the second part, Inertial Separation, a cascade multistage axial cyclone which is capable of classifying particles from 10 μm to 40 nm is developed and evaluated. The characteristics of the axial flow cyclone are also investigated, and a semi-empirical model is established to predict the cyclone collection efficiency curve. These works do not only enhance researchers' understanding of the specific particle control technologies, but also help engineers to develop better devices for solving current environmental problems or fulfilling industrial needs.

Dedicate to my parents, Yao-Hui Hsiao and Su-Sai Huang,

my wife, Hsiao-Hsi Chang,

my daughter, Jasmine Hsiao, and my son, Ethan Hsiao.

Table of Contents

List of Figures

List of Tables

"It is difficult to find any important engineering enterprise in which filtration and separation is not involved."

- Granular Filtration of Aerosols and Hydrosols

Dr. Chi Tien, 1989

Chapter 1

Introduction and Overview

1. Introduction to Particle Control Technology

In various industrial production processes, particulate contaminants are an important issue that must be resolved. For example, in semiconductor manufacturing, the deposition of a foreign particle on the wafer could kill the chips if it is greater than one-half the minimum device feature size. More generally, much particulate pollution is generated, and emitted during the production and transportation processes, and is must to be controlled under the regulation. Particulate pollution is typically an air-suspended mixture of microscopic solids and liquid droplets, and made up of a number of components, including acids (such as nitrates and sulfates), organic compounds, metals, dust particles, allergens (such as fragments of pollen or mold spores) and even bacteria or viruses. Based on their aerodynamic size, particles larger than 2.5 μm are generally defined as coarse particles, and particles equal or less than 2.5 μm ($PM_{2.5}$) are referred to as fine particles.

Numerous epidemiological studies have shown a significant association between exposure to fine particles and premature death from heart or lung disease, especially for older people [1, 2]. Recently, a comprehensive review on the health effects of particulate air pollution by Pope and Dockery (2006) [3] further concludes that long-term particulate matter (PM) exposure is associated with increased cardiovascular mortality, various blood markers of cardiovascular risk, histopathological markers of subclinical chronic inflammatory lung injury, and subclinical atherosclerosis. Short-term exposures are also associated with cardiovascular mortality and hospital admissions, stroke mortality and hospital admissions, myocardial infarctions, evidence of pulmonary and systematic inflammation and oxidative stress, altered cardiac autonomic function, and arterial

vasoconstriction. In response to scientific understanding of particulate pollution, on July 18 1997, the US Environmental Protection Agency has promulgated a $PM_{2.5}$ standard of 15 micrograms per cubic meter. However, in addition to protecting our natural environment and public health from particulate pollution, the industry still needs to remain economically viable. Therefore, to meet perceived needs for industrial particulate product collection, particulate contaminant abatement, and environmental pollution control, a variety of emission control technologies have been developed over the last 100 or so years [4].

Based on the different physical forces and the various collection substrates used, these particle control technologies can be grouped into six categories: liquid impingement (e.g., scrubbers), solid plate impaction (e.g. impactor), virtual impaction, centrifugal impaction (e.g., cyclones), filtration, and the use of external force fields (e.g., electrical precipitators and magnetic filters) [5]. Among these categories, filtration is known as the most economical means for achieving high removal efficiency of submicrometer aerosol particles with low concentration [6]. On the other hand, for supermicron particles with high concentration, cyclones (centrifugal impaction) are essentially superior to the other devices applying solid plate impaction, because they are less susceptible to overloading and particle bouncing, and also have high-volume treatment potential and low operating and maintenance costs.

The overall objective of this dissertation is to advance our current knowledge on these two particle control technologies. Accordingly, it has two major topics: (1) Aerosol Filtration – Liquid-coated Particle Loading, and (2) Inertial Separation – Axial Flow Cyclone.

2. PART I: Aerosol Filtration – Liquid Coated Particle Loading

From the industrial point of view, filters are the most cost-effective way to remove submicron airborne particles with low concentration. The pressure drop and the filtration efficiency of filter media are key parameters to characterize the performance of filters. The best filter combines high collection efficiency with low pressure drop. However, filtration efficiency and pressure drop are normally at the ends of a seesaw. A critical pressure drop is generally used as an indicator for replacing the filter. Therefore, understanding filter loading behavior under different conditions would help us to design a filter with better performance or a filter with a longer lifetime. In this dissertation, the main attention is on the filter pressure drop evolution (an indicator for energy consumption) during the dynamic filtration process.

An increasing number of articles have appeared in the literature concerning filters loaded with solid particles. In contrast, fewer works have so far have been dedicated to the filtration of liquid particles in gas streams, which form a considerable part of the air pollution produced by mechanical (cutting fluid mists) and agricultural (phytosanitary products) industries [7]. However, in reality, in industrial workplaces this so-called mist may not be pure liquid aerosol. It could be a solid particle coated with a thin film of liquid, normally greasy oil. For example, the particles emitted from internal combustion engines and those generated in the crankcases, as well as the metal working fluid (MWF) aerosols formed during the grinding and milling operations, are all liquid-coated particles. These liquid coated particles have recently caught public attention for their potential adverse health effects. Two studies [8, 9] indicated that more polycyclic aromatic

hydrocarbons (PAH) species were found in crankcase emissions than in tailpipe emissions, and the crankcase emissions may contribute to in-cabin PM. For metal working fluid (MWF) aerosols, growing evidence shows that the risk of adverse respiratory health effects increases with increasing MWF aerosol exposure [10-12]. Therefore, more filters are expected to be used to remove these liquid-coated particles.

In addition to the public health interest, there is an engineering motivation to study filter loading behavior under liquid-coated particle loading. The pressure drop evolution curve of a filter loaded with these liquid-coated particles could be very different from filters loaded with pure solid particles or pure liquid droplets, due to their different physical properties. In other words, the lifetime and the capacity of the filter for collecting liquid-coated particles would differ from its original design values for collecting solid or liquid particles.

To study the loading behavior of filters loaded with liquid coated particles, we tested two liquid-coated particle generation methods which can produce particles coated with different liquid film thicknesses. Moreover, from the pure liquid particle loading tests by Contal et al. (2004) [13], it is known the surface tension and viscosity of the liquid particles can play an important role in the liquid particle loading behavior. Unfortunately, Contal et al. [13] could not make further conclusions based on their observations. In this dissertation, the influences of the surface tension and viscosity of the coating fluid on the loading behavior were further experimentally explored.

For the first part of the dissertation, Aerosol Filtration – Liquid Coated Particle Loading, there are three major objectives:

1   to study the behavior of filters loaded with liquid coated particles of different solid/liquid volume fractions;

2   to explore the effects of liquid properties (surface tension and viscosity) on filters loaded with liquid coated particles; and

3   to establish a model for predicting the loading behavior of filters loaded with liquid coated particles.

3. PART II: Inertial Separation – Axial Flow Cyclone

Cyclones are particle collectors which utilize the centrifugal force created by the flow vortexes inside the devices to capture particles of high inertia. Because of the low cost of manufacturing, operating, and maintaining cyclones, they are widely used in a variety of industrial sectors, as well as in academic studies. In addition, because of thier simple and robust design, cyclones have the potential to treat high volumes and could be employed under high temperature or extreme pressure conditions. Further, compared to other inertial separators, such as impactors, cyclones are less prone to particle bounce and overloading, while maintaining low pressure drop.

In general, there are two typical designs: tangential flow cyclones and axial flow cyclones [14]. A conventional cyclone is generally a tangential flow cyclone, so few people recognize an axial flow cyclone (also called a swirling tube). The principal difference between these two designs is the relative directions of the cyclone's incoming and outgoing flows. For tangential flow cyclones, the aerosol inlet is perpendicular to the aerosol outlet, and the incoming flow is introduced tangentially into the cyclone body. For axial flow cyclones, the inlet and outlet are parallel to each other; that is, the air flow

enters and exits axial flow cyclones axially. This flow arrangement makes axial flow cyclones relatively easy to connect with other devices in line. Furthermore, a series of axial flow cyclones can be cascaded to form a multistage cyclone to sequentially classify particles in several different size ranges. However, to apply a centrifugal force for particle separation in the axial flow cyclone body, an additional vane section or helix channel needs to be installed to generate vortexes, which creates complexities in the flow field.

Although the basic cyclone configuration is simple, the particle motion inside a cyclone is still too complex to be exactly analyzed [15]. Semi-empirical expressions are usually utilized to predict the cyclone performance (the collection efficiency curve or the cutoff particle diameter, d_{50}). Moreover, these semi-empirical expressions are generally applicable only for the tangential cyclones with certain geometric dimensional ratios or within narrow dimensional variations. For axial flow cyclones, very few experimental results and models have been published, and thus the prediction of axial flow cyclone's performance is even more difficult than for a tangential cyclone. In addition, up to date systematic studies have not been published on the effect of different cyclone dimensions on axial flow cyclone performances.

In engineering applications, both tangential and axial flow cyclones are normally used to separate particles in the supermicron size range. Tsai et al. (2004) [14] first investigated the performance of the axial flow cyclone under a pressure of a few torr, and demonstrated the feasibility of cyclones for collecting particles in the nano-size range. In the second part of this dissertation, the performance of an axial flow cyclone is optimized, and a predictive model for collection efficiency is established. Furthermore, a multistage

axial cyclone is also developed to separate particles from 10 μm down to 40 nm. It is believed that this multistage axial cyclone is the second cascaded axial flow cyclone ever built, following the five-stage cascaded axial cyclone developed by Liu and Rubow (1984) [16], and it is the first cascaded cyclone that can reach a collection size range below 100 nm. Due to the multistage configuration, it can be applied for particle classification and collection at the same time and will be used by NASA for classification of Lunar and Martian dust simulants for health studies. Furthermore, by incorporating particle counting instruments, such as a condensation particle counter or aerosol electrometer, the multistage cyclone has the potential ability to measure particle size distribution.

For the second part of the dissertation, Inertial Separation – Axial Flow Cyclone, there are four objectives:

1   to investigate different configurations, including adding a upside-down cup, varying the vortex finder length, and different base geometries for the axial flow cyclone;

2   to establish a semi-empirical model for predicting axial flow cyclone collection efficiency curves;

3   to experimentally evaluate the separation efficiency of the multistage axial cyclone; and

4   to create an empirical model for the cutoff sizes of axial cyclone stages under different Reynolds numbers.

4. Dissertation Structure

In addressing its two major components, the whole dissertation contains seven chapters. The first part, including chapters 2, 3 and 4, focuses on the pressure drop

evolution of filter loaded with liquid-coated particle. The second part, including chapters 5 and 6, focuses on the performance and semi-empirical models of single and cascaded axial flow cyclones. Brief descriptions of each chapter follow.

In chapter 1, an overview of particle control technologies and their needs, applications, and challenges is presented. A general introduction, background information, and research objectives for the two particle control technologies - aerosol filtration and inertial separation - are given.

In chapter 2, selected models of filter loading behavior under solid and liquid particle loading are reviewed and summarized. Concepts and methods are applied to analyze and model our experimental data of on filters loaded with liquid-coated particles.

In chapter 3, two different experimental systems and methods, the heating-evaporation-condensation method and the co-solvent method, for generating polydisperse liquid-coated particles in submicron size range are developed, and their advantages and disadvantages are described. The effect of the filter surface property is also studied under the experimental system using the co-solvent method.

In chapter 4, experimental data are presented for two fibrous filter media, glass fiber and cellulose filters, loaded with particles coated with four different oils, dioctyl sebacate (DEHS), light mineral oil, castor oil and glycerol. Liquid-coated particles were produced by the co-solvent method, and two different particle size distributions were tested. The effect of filter media, liquid properties (surface tension and viscosity), face velocity, and particle size are discussed. An empirical model for predicting the filter loading curve is established.

In chapter 5, the particle collection efficiencies of axial flow cyclones with eight different geometric configurations, operated at 50 lpm aerosol flowrate, are evaluated and their effects are discussed. The geometric variation of test cyclones includes the optional addition of an upside-down cup, two vortex finder lengths, and two cyclone base shapes. A simple model is proposed to predict the particle collection efficiency curve of the optimal axial flow cyclone among those tested.

In chapter 6, a multi-stage axial cyclone is developed for NASA to classify Lunar and Martian dust simulants for health studies, and the performance of each stage is carefully calibrated. The multistage cyclone is comprised with six stages. The first stage is an impactor, and the other five stages are cyclones of axial flow design. An analysis including the flow Reynolds number and Stokes number is used to characterize the axial cyclone performance. The effect of the pressure in the cyclone body on the cutoff size is also explored.

In chapter 7, the accomplishments of this dissertation are summarized, and the issues and challenges that deserve future research efforts are addressed.

5. References

[1]   Seaton, A., MacNee,W., Donaldson, K., and Godden, D. (1995) Particulate air pollution and acute health effects. *The Lancet* 345, 176-178.

[2]   Pope, C.A., Bates, D. V., and Raizenne, M. E. (1995) Health effects of particulate air pollution: time for reassessment? *Environmental Health Perspectives* 103, 472-480.

[3]   Pope, C. A. and Dockery, D. W. (2006) Health effects of fine particulate air pollution: lines that connect. *J. Air & Waste Manage. Assoc.* 56, 709-742.

[4]   Golesworthy, T. (2009) A review of industrial flue gas cleaning *Filtration*, 9:23-33.

[5]   Pastuszka, J. S. (1997) Inertial Impaction, in Advances in Aerosol Filtration, Spurny, K.R., ed., Lewis Publishers, Amsterdam, 437-440.

[6]   Hinds, W.C. (1999) Aerosol technology: properties, behavior, and measurement of airborne particles. J. Wiley, New York.

[7]   Frising, T. et al. (2005) Clogging of fibrous filters by liquid aerosol particles: Experimental and phenomenological modelling study. *Chem. Eng. Sci.* 60, 2751-2762.

[8]   Hill, L. B. , Zimmerman, N. J., Gooch, J. A. (2005) A Multi-city Investigation of the Effectiveness of Retrofit Emissions Controls in Reducing Exposure to Particulate Matter in School Buses. *Clean Air Task Force*; Boston.

[9]   Zielinska, B., Campbell, D., Lawson, D. R., Ireson, R. G., Weaver, C. S., Hesterberg, T. W., Larson, T., Davey, M., and Liu, L-J (2008) Detailed Characterization and Profiles of Crankcase and Diesel Particular Matter Exhaust Emissions Using Speciated Organics. *Environ. Sci. Technol.*, 42: 5661–5666.

[10]   Kennedy, S. M., Greaves, I. A., Kriebel, D., Eisen, E. A., Smith, T. J., and Woskie, S. R. (1989) Acute pulmonary responses among automobile workers exposed to aerosols of machining fluids. *Am. J. Ind. Med.,* 15: 627–641.

[11]   Greaves, I. A., Eisen, E. A., Smith, T. J., Pothier, L. J., Kriebel, D., Woskie, S. R., Kennedy, S. M., Shalat, S., and Monson, R. R. (1997) Respiratory health of automobile workers exposed to metalworking fluid aerosols: respiratory symptoms. *Am. J. Ind. Med.,* 32: 450–459.

[12]   Calvert, G. M., Ward, E., Schnorr, T. M., and Fine, L. J. (1998) Cancer Risks Among Workers Exposed to Metalworking Fluids: A Systematic Review. *Am. J. Ind. Med.,* 33: 282–292.

[13]   Contal, P. et al. (2004) Clogging of fibre filters by submicron droplets: Phenomena and influence of operating conditions. *J. Aerosol Sci.* 35, 263-278.

[14]   Tsai, C. J. et al. (2004) Theoretical and experimental study of an axial flow cyclone for fine particle removal in vacuum conditions. *J. Aerosol Sci.* 35, 1105-1118.

[15]   Friedlander, S. K. (2000) Smoke, dust, and haze: fundamentals of aerosol dynamics. Oxford , New York.

[16]   Liu, B. Y. H., & Rubow, K. L. (1984). A new axial flow cascade cyclone for size characterization of airborne particulate matter., in Aerosols, Liu, B. Y. H., Pui, D. Y., & Fissan, H. J., ed., Elsevier Publishers, Amsterdam, 115–118.

Chapter 2

Review of Models of Filter Loading Behavior

1. Introduction

Filtration is a dynamic process. The filtration efficiency continuously improves as particles are trapped in the filter matrix or deposited on the filter surface. While the particle collection efficiency improves, the pressure drop across fibrous filters monotonically increases with the formation of particle dendrites on the filter fibers. The increase in pressure drop is undesirable, as it either reduces the filtration velocity or increases the load on the air movers, and a critical pressure drop is generally used as an indicator for replacing the filter. Therefore, understanding filter loading behavior is an important issue for filtration researchers and engineers. Macroscopically, filter loading behavior is characterized by the filter pressure drop ratio as a function of loaded mass or volume. The filter pressure drop ratio is defined as the ratio of the loaded-filter pressure drop (ΔP) to the filter initial pressure drop (ΔP_0). The loading mass/volume at the critical pressure drop is then defined as the loading capacity of the filter.

Previous studies [1-13] have shown that filter loading behavior (i.e., the pressure drop vs. the loaded particle mass/volume per unit filter area) is influenced by the structure of the filter medium (e.g., fibrous filter, fabric filter, granular filter, and membrane filter), the physical properties of particles (e.g., particle size, concentration, distribution broadness, particle phase, and charging status), the filtration face velocity, and environmental factors (e.g., relative humidity). For a low efficiency fibrous filter loaded with solid particles, the loading phase generally progresses through three different stages: depth filtration, a transition regime, and surface filtration (Fig. 2.1). Initially, particles load onto the filter fibers, forming dendrites, and the pressure drop gradually increases in a linear manner (depth filtration). As the loading continues, the filter pressure

drop starts a steeper increase, into the transition regime. In the last stage (surface filtration), the dendrites join together and create a dust cake on the front of the filter. The pressure drop again linearly increases until either the dust cake is mechanically re-structured by the large pressure drop, or the filter clogs. Two distinct linear slopes can be observed from the pressure drop evolution curves [3, 4]. The initial slope describes the loading behavior due to the particles collected by the filter fibers and other particles collected on fibers inside the filter media, and the final sharper slope is caused by the dust cake formation.
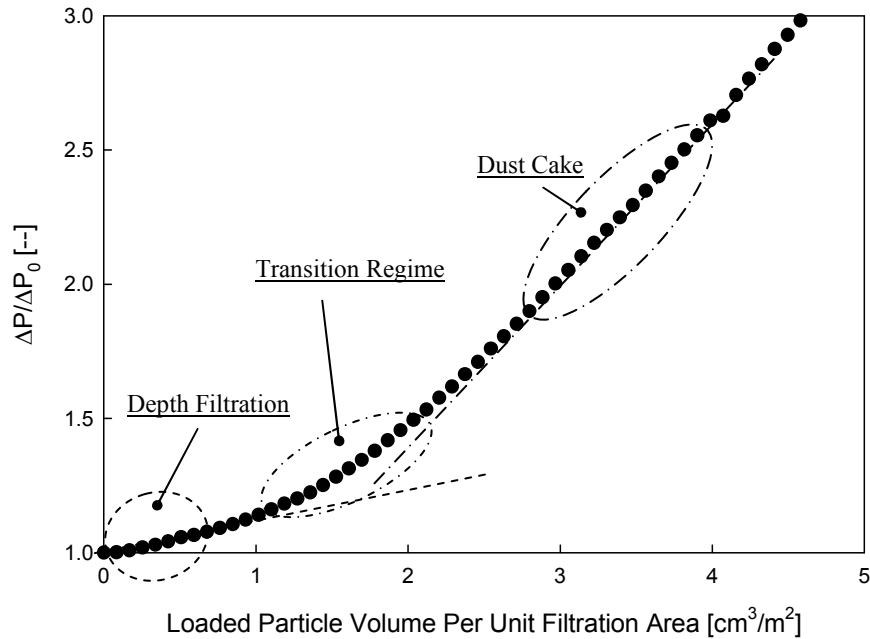
Figure 2.1 Typical loading behavior for fibrous filter loaded with solid particles

Because liquid particles can coalesce and ultimately flow, for filters loaded with liquid particle/droplets the nature of the loading behavior is much more variable and more complicated than that for solid particles (Fig. 2.2). At the initial filtration stage, the droplets are deposited mainly on the surface of fibers and interfere only marginally with

the flow, thus the pressure drop increases slowly. Later, the pressure drop starts to accelerate again due to the formation of liquid bridges, pools, and films between fibers and their intersections [14]. In this stage, sometimes the liquid within the filter would redistribute when the pressure drop reaches a characteristic threshold [5], and the increasing rate of the pressure drop slows down for a while. At last, a "pseudo-steady state" is attained, where equilibrium is established between loading, drainage, re-entrainment, and evaporation. The liquid particle loading behavior is closely related to the surface properties of the filter (e.g., wettability) and physical properties of the liquid (e.g., surface tension, viscosity, size distribution) [15].
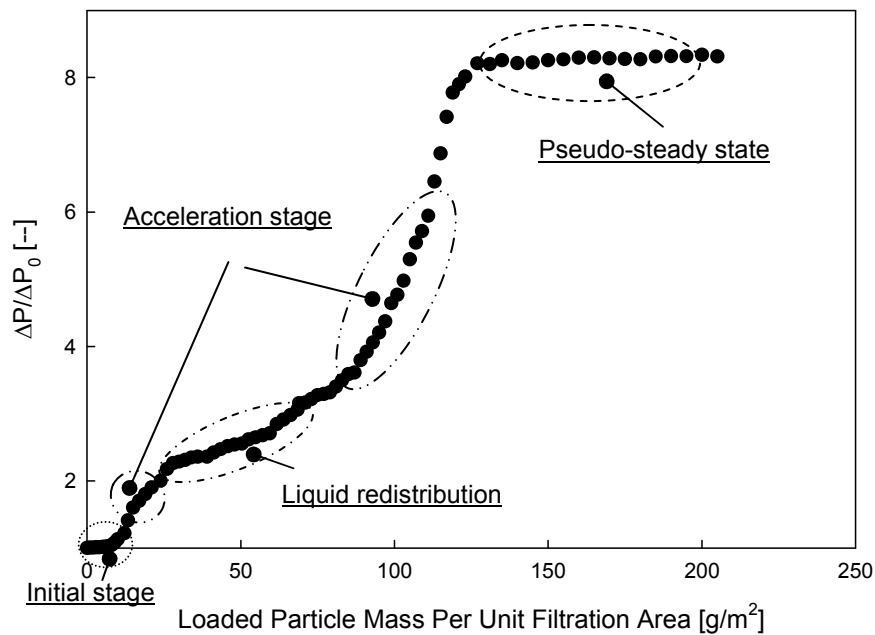
Figure 2.2   Typical loading behavior for fibrous filter loaded with liquid particles

2. Pressure Drop of Clean Filter

Before reviewing the pressure drop models for loaded filters, it is essential to understand the pressure drop across clean filters. One fundamental method to estimate the

pressure drop across a clean filter is based on the summation of the drag forces of all the fibers. At low Reynolds numbers ($\rho U d_f / \mu < 1$), the drag force on a cylinder fiber array can be approximated by the product of flow velocity (U), viscosity (μ), and a drag coefficient (F), and the pressure drop of clean filter (ΔP_0) can be described as:

$$\Delta P_0 = L_f \mu U F \text{, and} \tag{2.1}$$

$$L_f = \frac{4\alpha_f Z}{\pi d_f^2}, \tag{2.2}$$

where

ρ is the density of fluid,

L_f is the total length of all filter fibers per unit filtration area,

F is the drag coefficient,

Z is the filter thickness,

α_f is the filter packing density, and

d_f is the fiber diameter.

The accuracy of Eqn. 2.1 is highly dependent on the drag coefficient (F). Table 2.1 lists four general expressions of F used for calculating the pressure drop across a clean filter. The expressions for F proposed by Happel (1959) [16], Kuwabara (1959) [17], and Stechkina and Fuchs (1963) [18] are all derived theoretically by solving the flow field in a system of parallel circular cylinders at low Reynolds number, but applying different boundary conditions. Happel (1959) [16] assumed the normal velocity and the tangential stress at the cylindrical surface are zero, while Kuwabara (1959) [17] assumed the normal velocity and the vorticity are zero. However, experimental results generally

show that the accuracy of these expression in predicting filter pressure drop is not as good as the empirical expression proposed by Davies (1952) [19]. Werner and Clarenburg (1965) [20] performed extensive experimental tests of glass fiber filters with packing densities ranging from 0.039 to 0.084, and showed good agreement with the predictions of Davies. Possibly, the difference between theoretical and empirical values can be attributed to the theoretical models not considering the random orientation of the fiber cylinders and the flow interference between them.

Table 2.1   Drag Coefficients (F)

Author	Expression of F
Davies (1952) [19]	$F = 16\pi\alpha_f^{0.5}(1 + 56\alpha_f^3)$ for $0.006 < \alpha_f < 0.3$ $F = 16\pi\alpha_f^{0.5}$ for $\alpha_f < 0.006$
Happel (1959) [16]	$F = 8\pi \dfrac{1}{-\ln\alpha_f - ((1-\alpha_f^2)/(1+\alpha_f^2))}$
Kuwabara (1959) [17]	$F = 8\pi \dfrac{1}{-\ln\alpha_f + 2\alpha_f - 0.5\alpha_f^2 - 3/2}$
Stechkina and Fuchs (1963) [18]	$F = 8\pi \dfrac{1}{-\ln\alpha_f - 3/2}$

If Davies' expression is chosen, the pressure drop of a clean filter can be written in terms of fluid viscosity (μ), face velocity (U), filter thickness (Z), fiber mean diameter (d_f), and packing density (α_f):

$$\Delta P_0 = \mu Z U \frac{64\alpha_f^{1.5}(1+56\alpha_f^3)}{d_f^2} \quad \text{for } 0.006 < \alpha_f < 0.3 \text{, and} \tag{2.3}$$

$$\Delta P_0 = \mu Z U \frac{64\alpha_f^{1.5}}{d_f^2} \quad \text{for } \alpha_f < 0.006 \text{.} \tag{2.4}$$

Notice that these equations are semi-empirical and do not account for the fiber size variation in the filter media. An intensive survey by Jackson and James (1986) [21] also shows the prediction starts to deviate from the experimental measurements when the packing density is below 0.001.

3. Pressure Drop of Solid Particle Loading

The pressure drop across filters loaded with solid particles has been extensively studied, and several researchers have attempted to establish mathematical models to simulate the process of pressure drop evolution for a filter loaded with solid particles under different filtration regimes. In this section, a few representative models are reviewed.

At the microscopic level, the pressure drop increase across a loaded filter is due to the additional flow resistance contributed by the deposited particles. These deposited particles collect other incoming particles to form particle dendrites (branched structures of particles, Fig. 2.3) and further disturb the original flow field. The formation mechanisms of the particle dendrite are analogous to the mechanical filtration mechanisms (inertial impaction, direct interception, and Brownian diffusion), and they are closely related to the particle size. Kanoaoka et al. (1986) [22] summarized the different particle deposition patterns (dendrite morphology) on a single fiber and showed

the continuous changes of the patterns with the particle Peclet number (Pe) and Stokes number (StK) (Fig. 2.4). The differences between these deposition patterns create different flow resistances and result in different pressure drops across loaded filters. However, the linkage between the microscopic dendrite structure, loaded particle mass and the macroscopic pressure drop measurements is still not very clear. The major challenge in this field is investigating and quantifying the particle dendrite structure on loaded filters, especially for polydisperse submicron particles.
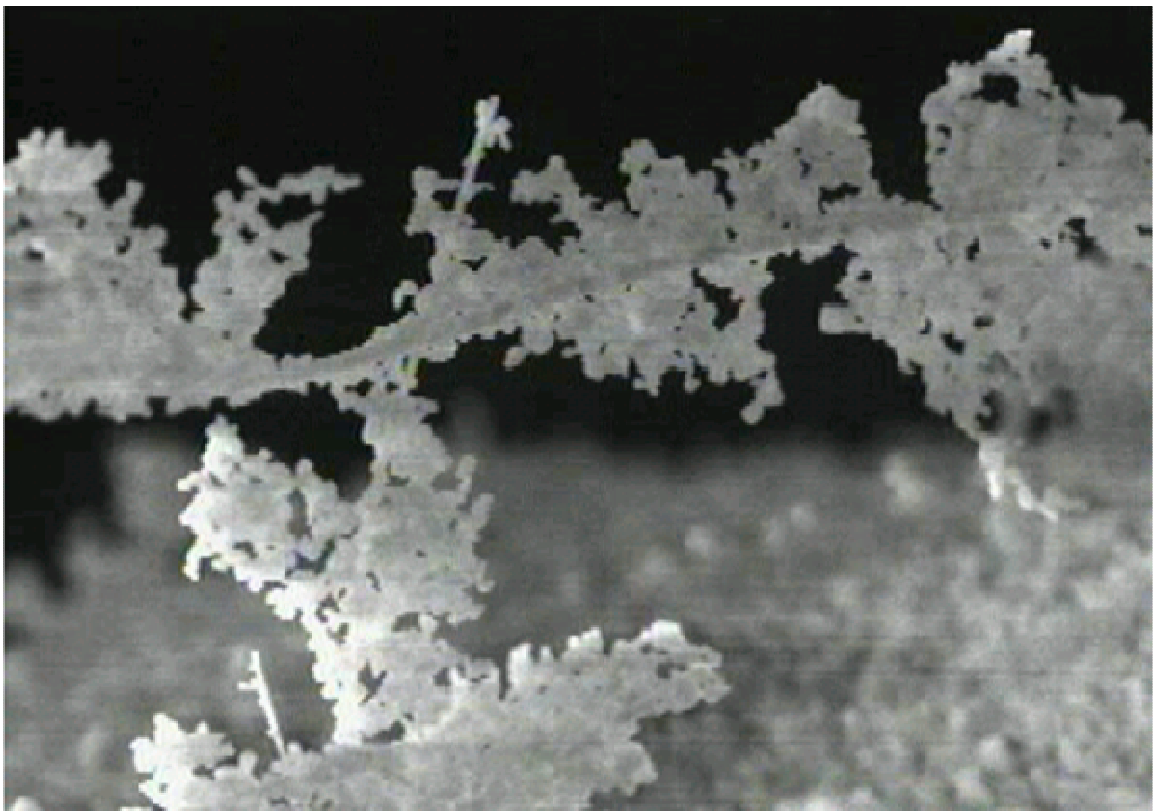
Figure 2.3   Particle dendrite
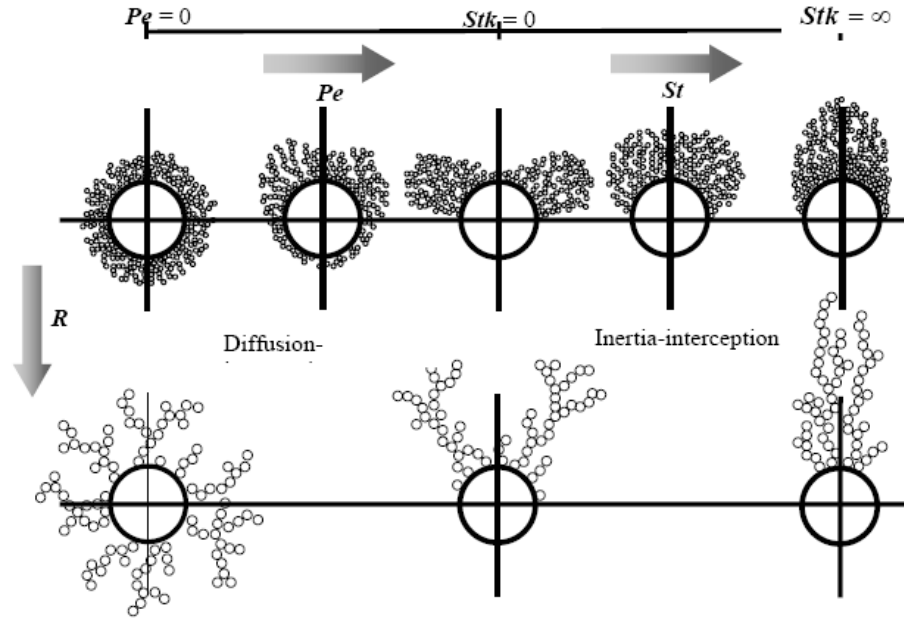
Figure 2.4   Particle dendrite morphology transitions

(Kanaoka, C., Emi, H., and Hiragi, S., *Proc. of 2nd Int. Aerosol Conf.*, Berlin, 1986, 674.)

[22]

Payatakes and Tien (1976) [23] first established a deterministic model to simulate particle dendrite growth in fibrous filters and derived a pressure drop equation for loaded filters. Although it captures the average growth of the particle dendrite, the model is quite complicated and requires two density functions: the dendrite age distribution function ($\chi(t;\tau,\ \theta)dt$) and the dendrite number distribution function ($N(\tau,\theta)dt$). In principle, these density functions could be determined from particle trajectory calculations, but in reality they are both difficult to estimate. In addition, the drag force (F_{pk}) acting on the dendrite particles in Eqn. (2.5) is also not easy to evaluate.

$$\frac{\Delta P(\tau)}{\Delta P_0} = \frac{F_f + \int_0^\pi \left\{ \int_0^\tau \left[\sum_{k=1}^{M(t,\theta)} m_t(t,\theta) F_{pk}(\theta) \right] \chi(t,\tau,\theta)dt \right\} N(\tau,\theta)d\theta}{F_f},$$

<div align="right">(2.5)</div>

where

τ is the time measured from the beginning of the aerosol flow through the filter,

t is the age of a dendrite starting from the instant of deposition of its first particle,

$\Delta P(\tau)$ is the pressure drop across a differential filter element at time τ,

ΔP_0 is the initial pressure drop across a differential filter element,

$\chi(t, \tau, \theta)$ is the number of dendrites between θ and $\theta + d\theta$ at time τ,

$N(\tau, \theta)$ is the fraction of the dendrites with age between t and $t + dt$,

F_f is the drag force per unit length of clean filter fiber,

$F_{pk}(\theta)$ is the drag force on a particle in the kth layer of a dendrite at θ, and

θ is the angular coordinate measured from the front stagnation point.

A few researchers [24-27] have proposed different methods to calculate the drag force on a dendrite, but all achieve limited success. Moreover, the critical assumption of Payatakes and Tien's model is that the particle dendrites have negligible effect on the flow field, which greatly limits the application at the initial stage of the filter loading.

Kanaoka and Hiragi (1990) [28] proposed another theoretical model for the pressure drop across a dust loaded filter (ΔP_l) by summing the drag forces acting on the individual dust loaded fibers (F_l). The F_l is evaluated in the same manner as Newton's resistance law, and the diameter of a dust loaded fiber (d_{fm}) is chosen as a representative parameter of dendrite structure.

$$\Delta P_l = L_f \int_0^L F_l dz, \tag{2.6}$$

21

$$F_l = C_{dm} d_{fm} \frac{\rho U^2}{2},$$
(2.7)

where

C_{dm} is the drag coefficient of a dust loaded filter,

d_{fm} is the diameter of a dust loaded fiber (Fig. 2.5), and

ρ is the fluid density.
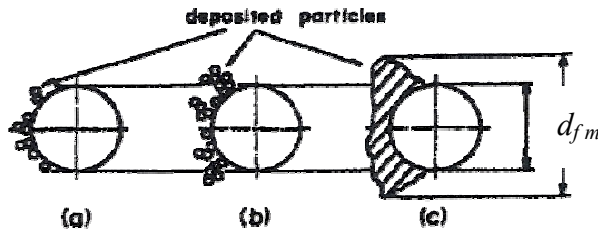
Figure 2.5   The diameter of a dust loaded fiber (d_{fm}) at different stages

(Kanaoka, C. et al., *J. Aerosool Sci.*, 21, 1990, 127.) [28]

The drag coefficient of a dust loaded filter (C_{dm}) and the diameter of a dust loaded fiber (d_{fm}) are two critical parameters in this model, and they are correlated with the filtration condition/collection mechanism and a dimensionless volume (V_{ac}) based on the experimental data in Kanaoka and Hiragi's article. Kanaoka and Hiragi also classified the rate of increase of d_{fm} into three stages: no growth at very low V_{ac} (Fig. 2.5a), rapid growth at intermediate V_{ac} (Fig. 2.5b), and damped growth at large V_{ac} (Fig. 2.5c). It is claimed that the model is applicable to the prediction of the pressure drop of a dust loaded filter under any filtration conditions. However, the limitation of this model is that the effective fiber diameter (d_{fm}) and drag coefficient of the dust loaded fiber (C_{dm}) can not be estimated theoretically. They are empirically fitted with the accumulated volume of captured particles and can not be determined without prior experimentation.

Instead of evaluating the drag forces on the particle dendrites formed by the deposited particles, Bergman et al. (1978) [29] considered particle dendrites as new fibers and modified Davies' equation (Eqn. 2.4) to include an additional pressure drop due to this newly formed fiber. In addition, to correct the interference between the dendrites and filter fibers, they increased the fiber and dendrite volume fraction by the factors $(L_f+L_p)/L_f$ and $(L_f+L_p)/L_p$ respectively.

$$\Delta P_l = 16\pi\mu U\left[(\alpha_f \frac{L_f+L_p}{L_f})^{0.5} L_f + (\alpha_P \frac{L_f+L_p}{L_P})^{0.5} L_P\right],$$ (2.8)

where

α_p is the packing density due to deposited particle, and

L_p is the total length of the "new" fiber formed by the particle dendrites.

The L_p can be evaluated as following

$$L_p = \frac{4\alpha_p Z}{\pi d_p^2}.$$ (2.9)

Combining Eqn. (2.8) and Eqn. (2.9), the expression for the pressure drop across a loaded filter can be rewritten as

$$\Delta P_l = 64\mu Z U\left(\frac{\alpha_f}{d_f} + \frac{\alpha_p}{d_p}\right)\left(\frac{\alpha_f}{d_f^2} + \frac{\alpha_p}{d_p^2}\right)^{0.5}.$$ (2.10)

By comparison with experimental data, Vendel et al. (1992) [30] indicated the pressure drop predicted by Bergman's model during the loading process is underestimated. They suspected it was due to the assumption that particle deposition and particle diameter are uniformly distributed over the whole filter thickness. Therefore, Thomas et al. (1999, 2001) [11, 31] tried to relax the assumption of homogeneous

particle deposition over the whole filter thickness and the assumption of monodisperse challenging particles. They extend Bergman's model by dividing the filter into various layers with thickness Z_j and assumed particles homogeneously deposited in each layer of the filter. They also proposed an equation to calculate the diameter of the "new" fiber ($\overline{d}_{pJ,t}$) formed by the particle dendrite in the layer J at time t.

$$\overline{d}_{pJ,t} = \frac{\overline{d}_{pJ,t-1}\alpha_{pJ,t-1}\rho_p dZ + \sum_{i=0}^{nc}(m_{fJ,i,t} + m_{pJ,i,t})d_{p,i}}{\alpha_{pJ,t-1}\rho_p dZ + \sum_{i=0}^{nc}(m_{fJ,i,t} + m_{pJ,i,t})}, \tag{2.11}$$

where

n_c is the number of particle size range,

$m_{fJ,i,t}$ is the particle mass collected by filter fiber in layer J at time t,

$m_{pJ,i,t}$ is the particle mass collected by particle dendrite in layer J at time t,

$\alpha_{pJ,t}$ is the packing density of collected particles in layer J at time t, and

ρ_p is the particle density.

$m_{fJ,i,t}$, $m_{pJ,i,t}$ and $\alpha_{pJ,t}$ can be calculated by knowing the particle penetration of filter fibers ($P_{fJ,i,t}$) and the particle penetration of particle dendrites ($P_{pJ,i,t}$), which are estimated through the Payet model (1991) [32] in Thomas et al.'s article (1999) [31].

Thomas et al. claim the model needs only the knowledge of clean filter, inlet aerosol and filtration characteristics, and can then describe the transition between depth filtration and cake filtration. However, it requires repeat calculations of the collection efficiency, the loaded particle mass, and the packing density of each layer for each time increment up to the final filtration time. In addition, the rationale for applying the two purely empirical factors of Bergman's model is questionable.

For a heavily loaded filter, HEPA filter, or fabric filter, surface filtration is dominant, and the loaded particles mainly form the dust cake on the filter. The total pressure drop across the loaded filter can then be separated into two parts. One is contributed by the pressure drop across the clean filter (ΔP_0), and the other is contributed by the pressure drop of the dust cake (ΔP_c). Therefore, the pressure drop across a loaded filter can expressed as

$$\Delta P_m = \Delta P_0 + \Delta P_c. \tag{2.12}$$

The models of the dust cake pressure drop are more mature and consistent than those describing the pressure drop transition between depth filtration and cake filtration. One classic work studying the effect of particle polydispersity and shape on dust cake pressure drop, done by Endo, Chen and Pui (1998) [8], is briefly summarized here. The derivation concept still originates from the summation of all drag forces on the deposited particles. The equation proposed by Yoshida, Kousaka, and Okuyama (1979) [33] is chosen to estimate the drag force (F_1) acting on a single particle within the Stokesian and non-Stokesian regimes.

$$F_1 = \frac{\pi}{8} d_p^2 \rho u_i^2 \left(0.55 + \frac{4.8}{\sqrt{\mathrm{Re}_p}} \right)^2 \kappa \text{, and} \tag{2.13}$$

$$\Delta P_c = \int_{-\infty}^{+\infty} F_1 v(\varepsilon) n_t f(d_p) d(d_p) \cdot \frac{u_i}{u_s} H, \tag{2.14}$$

where

u_i is the interstitial flow velocity,

u_s is the superficial flow velocity,

Re_p is particle Reynolds number,

κ is the dynamic shape factor of particle,

$v(\varepsilon)$ is the void function and ε is the porosity (it represents the effect of neighboring

          particles),

n_t is the total particle number in unit volume of dust cake,

$f(d_p)$ is the particle size distribution function, and

H is the thickness of dust cake.

By further assuming the lognormal particle size distribution, the general

expression of the dust cake pressure drop can be derived:

$$f(\ln d_p) = \frac{1}{\sqrt{2\pi}\ln\sigma_g}\exp\left[-\frac{(\ln d_p - \ln d_{pg})^2}{2\ln^2\sigma_g}\right], \text{ and} \tag{2.15}$$

$$\Delta P_C = 0.2269\rho_f u_s^2 H \frac{(1-\varepsilon)v(\varepsilon)}{\varepsilon^3}\frac{\kappa}{d_p\exp(2.5\ln^2\sigma_g)}$$

$$+ 3.96\sqrt{\rho_f \mu u_s^{1.5}}H\frac{(1-\varepsilon)v(\varepsilon)}{\varepsilon^{2.5}}\frac{\kappa}{d_p^{1.5}\exp(27/8\ln^2\sigma_g)} \qquad , \tag{2.16}$$

$$+ 17.28\mu u_s H\frac{(1-\varepsilon)v(\varepsilon)}{\varepsilon^2}\frac{\kappa}{d_p^2\exp(4\ln^2\sigma_g)}$$

where

d_{pg} is the geometric mean diameter, and

σ_g is the geometric standard deviation of the particle size distribution.

If particles are monodisperse, spherical, and in the Stokesian regime, then Eqn.

(2.16) can be reduced to the well known Kozeny-Carman equation in porous media.

4. Pressure Drop of Liquid Particle Loading

For a fibrous filter loaded with liquid particles, only a few models have been established, and they primarily work for liquid loaded filters under steady-state saturation conditions, instead of simulating the pressure drop's evolutionary behavior.

Liew and Conder (1985) [14] performed various tests on filters with mean fiber diameters of 4, 8, 12 and 22 μm and developed an empirical equation to predict the pressure drop at the final steady-state stage (P_s). They suggested the equation can be used for rough estimates of the pressure drop in a wet filter of packing density over 0.02.

$$\frac{\Delta P_s}{\Delta P_0} = \left[1.09 \left(\alpha_f \frac{Z}{d_f} \right)^{-0.561} \left(\frac{U\mu}{\gamma_{LV} \cos\theta} \right)^{-0.477} \right], \qquad (2.17)$$

where

γ_{LV} is the liquid surface tension, and

θ is the contact angle between the deposited droplet and the fiber.

Raynor and Leith (2000) [34] provided another empirical expression for the pressure drop (P_s) at the steady-state loading stage of a liquid loaded filter. The P_s is correlated with the steady-state saturation ratio (S_e) and packing density (α).

$$\ln\left(\frac{\Delta P_s}{\Delta P_0} \right) = \frac{S_e^{0.91 \pm 0.06}}{\alpha^{0.69 \pm 0.06}} \exp(-1.21 \pm 0.24). \qquad (2.18)$$

They also constructed an empirical expression for S_e against the dimensionless numbers (Ca, Bo, Dr) by a commercialized statistic software (SAA/STAT).

$$S_e = \frac{\alpha^{0.39 \pm 0.09}}{Bo^{[(0.47 \pm 0.06) + (0.24 \pm 0.07)\ln(Bo)]} Ca^{0.11 \pm 0.04}} \qquad (2.19)$$
$$\times \exp\left[(-0.04 \pm 0.36) + ()6.6 \pm 0.15 \times 10^5 \, Dr \right]$$

where

Bo   is Bond number ($\rho g d_f^2 / \gamma_{LV} \times 10^5$),

Ca   is capillary number ($\mu_g u_i / \gamma_{LV} \times 10^5$) and μ_g is the fluid viscosity, and

Dr   is non-dimensional drainage rate.

The application of both Liew and Conder's model and Raynor and Leith's model is limited, since they are both purely empirical. For instance, Liew and Conder's model requires the filter packing density be larger than 0.02, and Raynor and Leith's model applies to the filter thickness is less than 0.88 cm. In addition, these two models applicable only for predicting the steady-state pressure drop of a liquid loaded filter.

Frising et al. (2005) [35] attempted to establish a pressure drop model over different filtration/loading stages based on an adapted version of Davies' equation. To imitate the gradual clogging of the filter, they characterized the whole loading process into four stages and divided the filter into n_p layers of thickness dZ. In the first stage, the loaded liquid particles are assumed to perfectly coat the filter fiber and to form a film or tube around the fiber. Therefore, the fiber diameter (d_f) and the packing density (α_f) are replaced with the "coated" fiber diameter ($d_{f,w}$) and the new packing density term ($\alpha_f + \alpha_l$), which includes the loaded droplets.

$$d\Delta P = 64 \mu U dZ \frac{(\alpha_f + \alpha_l)(\alpha_f + \alpha_l)^{0.5}}{d_{f,w}^2} \times \left(1 + 16(\alpha_f + \alpha_l)^{2.5}\right), \tag{2.20}$$

$$d_{f,w} = d_f \sqrt{\frac{\alpha_f + \alpha_l}{\alpha_f}}, \text{ and} \tag{2.21}$$

$$dZ = \frac{Z}{n_p},$$ (2.22)

where

α_f is the packing density of clean filter, and

α_l is the additional packing density due to loaded droplets.

The second stage is defined as the formation of the liquid bridge and liquid film at fiber intersections, and the diameter of the "coated" fiber remains constant in this stage. Since the air flow is greatly influenced by the liquid bridge and films, the air velocity needs to be modified to take this effect into account. The pressure drop equation for the second stage is given as:

$$d\Delta P = 64\mu dZ \frac{\left(\alpha_f + \alpha_{tube}\right)\left(\alpha_f + \alpha_l\right)^{0.5}}{d_{f,w}^2}$$
$$\times \left(1 + 16(\alpha_f + \alpha_l)^{2.5}\right)\frac{U}{1 - \alpha_l + \alpha_{tube}},$$ (2.23)

where

α_{tube} is the maximum packing density due to the liquid coated on the filter fiber.

So far, however, α_{tube} can not be determined either theoretically or experimentally. In Frising et al.'s article, the value was determined experimentally to optimize the prediction of the model.

In the third stage, the liquid packing density reaches the maximum, and liquid migration between the filter layers starts. The pressure drop is considered constant at this stage. Once the liquid begins to drain out of the filter, the loading process enters the fourth stage, in which

$$dΔP = 64μdZ \frac{\left(α_f + α_{tube}\right)\left(α_f + α_{film}\right)^{0.5}}{d_{f,w}^2}$$
$$× \left(1 + 16(α_f + α_{film})^{2.5}\right)\frac{U}{1 - α_{film} + α_{tube}} \quad , \qquad (2.24)$$

where

$α_{film}$ is the maximum liquid packing density.

$α_{film}$ can be estimated by weight the test filter before and after experiments.

Frising et al. (2005) [35] reported fairly good agreement between their experimental results and the predictions of the model, and argued the model needs only two parameters, $α_{tube}$ and $α_{film}$. However, the assumption of perfect liquid coating on filter fibers is not accurate. For liquids with high surface tension, the deposited droplets would create liquid beads, instead of forming a film, on the fibers [36]. In addition, Mullins and Kasper (2006) [37] also point out some misconceptions in Frising et al.'s work. They cited the other studies related to mist filters and film flows, and comment that stable films (without droplet) can not exist on single cylindrical fibers. Moreover, the estimation of $α_{tube}$ in Frising et al.'s model still remains unsolved.

5. Concluding Remark

The loading curves of a filter loaded with liquid coated particles are expected to transition from that of a filter loaded with pure solid particles to that of a filter loaded with pure liquid droplets as the coated liquid film thickness increases. Therefore, one possible method to model the whole loading behavior might be integrating or/and modifying the models of liquid particle loading with the models of solid particle loading.

6. References

[1]   Novick, V. J., Monson, P. R., Ellison, P. E. (1992) The effect of solid particle mass loading on the pressure drop of HEPA filters. *J. Aerosol Sci.,* 23:657-665.

[2]   Gupta, A., Novick, V. J., Biswas, P., Monson, P. R. (1993) Effect of humidity and particle hygroscopicity on the mass loading capacity of high efficiency particle air (HEPA) filters. *Aerosol Sci. Technol.* 19: 94-107.

[3]   Japuntich, D. A., Stenhouse, J. I. T., Liu, and B. Y. H. (1994) Experimental results of solid monodisperse particle clogging of fibrous filters. *J. Aerosol Sci.* 25**:** 385-393.

[4]   Japuntich, D. A., Stenhouse, J. I. T., Liu, and B. Y. H. (1997) Effective pore diameter and monodisperse particle clogging of fibrous filters. *J. Aerosol Sci.* 28**:** 147-158.

[5]   Walsh, D. C. (1996) Recent advances in understanding of fibrous filter behavior under solid particle loading. *Filtration and Separation (June)* 501-506.

[6]   Walsh, D. C., Stenhouse, J. I. T., Scurrah, K. L., and Graef, A. (1996) The effect of solid and liquid aerosol particle loading on fibrous filter material performance. *J. Aerosol Sci.,* 27(suppl. 1):S617-618.

[7]   Barrett, L.W. and Rousseau, A.D. (1998) Aerosol loading performance of electret filter media. *AIHA J.* 59: 532-539.

[8]   Endo, Y., Chen, D. R., and Pui, D. Y. H. (1998) Effects of particle polydispersity and shape factor during dust cake loading on air filters. *Powder Technology*, 98:241-249.

[9]   Brown, R.C. and Wake, D. (1999) Loading filters with monodisperse aerosols: macroscopic treatment. *J. Aerosol Sci.* 30:227-234.

[10]   Chen, C. C., Chen, W. Y., Huang, S. H., Lin, W. Y., Kuo, Y. M., and Jeng, F. T. (2001) Experimental study on the loading characteristics of needlefelt filters with micrometer-sized monodisperse aerosols. *Aerosol Sci. Technol.* 34: 262-273.

[11]   Thomas, D. Penicot, P., Contal, P., Leclerc, D., and Vendel, J. (2001) Clogging of fibrous filter by solid aerosol particles: experimental and modeling study. *Chemical Engineering Science*, 56:3549-3561.

[12]   Miguel, A. F. (2003) Effect of air humidity on the evolution of permeability and performance of a fibrous filter during loading with hygroscopic and non-hygroscopic particles. *J. Aerosol Sci.* 34**:** 783-799.

[13]   Lawrence, C. A. and Liu, P. (2006) Relation of structure, properties and performance of fibrous media for gas filtration. *Chem. Eng. Technol.* 29:957-967.

[14]   Liew, T. P. and Conder, J. R. (1985) Fine mist filtration by wet filters. *J. Aerosol Sci.* 16: 497-509.

[15]   Contal, P., Simao, J., Thomas, D., Frising, T., Callé, S., Appert-Collin, J. C., and Bémer, D.   (2004) Clogging of fiber filters by submicron droplets: Phenomena and influence of operating conditions. *J. Aerosol Sci.* 35: 263-278.

[16]   Happel, J. (1959) Viscous flow in arrays of cylinders. *Am. Int. Chem. Eng. J.* 5: 174-177.

[17]   Kuwabara, S. (1959) The forces experienced by randomly distributed parallel circular cylinders or spheres in viscous flow at small Reynolds numbers. *J. of Phys. Soc. Japan* 14: 527-532.

[18]   Stechkina, I. B. & Fuchs, N. A. (1963) A note on the theory of fibrous filters. *Ann. Occup. Hyg.* 6: 27-30.

[19]   Davies, C. N. (1952) The separation of airborne dust and particles. *Institution of Mechanical Engineers,Proceedings* : 185-198.

[20]   Werner, R. M. and Clarenburg, L. A. (1965) Aerosol Filters. *Ind. Eng. Chem. Proc. Des. Dev.* 4: 288-293.

[21]   Jackson, G. W. and James, D. F. (1986) The permeability of fibrous porous media. *Can J. Chem. Eng.* 64: 364-374.

[22]   Kanoaoka, C., Emi, H., Hiragi, S., and Myojo, T. (1986) Mophology of particulae agglomerates on a cylindrical fiber and the collection efficiency of a dust loaded fiber. *Aerosol: Formation and Reactivity, 2nd International Aerosol Conference* 674-677.

[23]   Payatakes, A. C. and Tien, C. (1976) Particle deposition in fibrous media with dendrite-like pattern: a preliminary model. *J. Aerosol Sci.* 7: 85-100.

[24]   Medjimorec, V., Okuyama, K., and Payatakes, A. C. (1981) Estimation of the drag forces acting on particle dendrites. *J. Coloid Interface Sci.* 82: 543-559.

[25]   Pendse, H., Tien, C., and Turian, R. M. (1981) Drag force measurement of single spherical collectors with deposited particles. *AIChE J.* 27: 363-372.

[26]   Hall, M. S. (1988) Calculation of the drag on a sphere with an attached dendrite. *J. Aerosol Sci.* 19: 317-331.

[27]   El-Shobokshy, M. S., Al-Sanea, S. A., and Adnan, A. M. (1994) Computer simulation of monodisperse aerosol collection in fibrous filters. *Aerosol Sci. Technol.* 20: 149-160.

[28]   Kanaoka, C. and Hiragi, S. (1990) Pressure drop of air filter with dust load. *J. Aerosol Sci.* 21: 127–137.

[29]   Bergman, W. et al. (1978) Enhanced filtration program at LLNL. 15th DOE/NRC nuclear air cleaning conference, Boston.

[30]   Vendel, J., Letourneau, P., and Renaudin, V. (1992) Effects of the particle penetration inside HEPA filtration media. *21st DOE/NRC Nuclear Air Cleaning Conf.,* San Diego: 799-808.

[31]   Thomas, D. Contal, P., Renaudin, V., Penicot, P., Leclerc, D., and Vendel, J. (1999) Modeling pressure drop in HEPA filters during dynamic filtration. *J. Aerosol Sci.,* 30:235-246.

[32]   Payet, S. (1991) Filtration Stationnaire et dynamique des aérosol liquides submicroniques. Ph.D. Dissertation. Paris XII.

[33]   Yoshida, T., Kousaka, Y., and Okuyama, K. (1979) *Aerosol Science for Engineers, Power,* Tokyo: 24.

[34]   Raynor, P. C. and Leith, D. (2000) The influence of accumulated liquid on fibrous filter performance. *J. Aerosol Sci.* 31: 19–34.

[35]   Frising, T., Thomas, D., Bémer, D., and Contal, P. (2005) Clogging of fibrous filters by liquid aerosol particles: Experimental and phenomenological modelling study. *Chem. Eng. Sci.* 60: 2751-2762.

[36]   Brown, R.C. (1993) Air filtration : an integrated approach to the theory and applications of fibrous filters. Oxford , New York.

[37]   Mullins, B. J., and Kasper, G. (2006) Comment on: "Clogging of fibrous filters by liquid aerosol particles: Experimental and phenomenological modeling study" by Frising et al.. *Chem. Eng. Sci.* 61: 6223-6227.

Chapter 3

Submicron Liquid Coated Particle Loading

1. Introduction

The pressure drop evolution curve during the filtration process is an important characteristic for defining filter performance. Most researchers are focusing on filters loaded with solid particles, and some are working with liquid particles, such as mist. However, in the real world, particles coated with a thin film of liquid are often encountered in the environment and in industrial workplaces, and they can cause adverse health effects due to the toxicities of the coating liquids. Filter performance under such particle loading is quite different from that of filters loaded with completely solid particles or liquid droplets, and the behavior of filters loaded with liquid-coated particles has not been specifically explored yet. As a result, there is a need for understanding and characterizing the pressure drop evolution of filters (filter loading behavior) challenged by liquid-coated particles.

In this chapter, the general filter loading behavior of liquid-coated particles is characterized. Two different methods are applied to generate polydisperse submicron liquid-coated particles. One is the heating-evaporation-condensation method, and the other is the co-solvent method. Four different filter media, including a high efficiency fiber glass filter and three membrane filters with different surface properties (untreated, hydrophilic, and oleophobic), are tested under identical conditions to study the effect of the filter media properties.

2. Experimental Methods

To systematically study the loading behavior of filters loaded with liquid-coated particles, a stable generator of liquid-coated particles with controllable liquid volume

35

ratios is needed. There is no such an aerosol generator commercially available. To carry out this study we developed two liquid-coated particle generation systems.

2.1   Particle Generation by the Heating-Evaporation-Condensation Process

For the first liquid-coated particle generation system, a Condensation Monodisperse Aerosol Generator (CMAG, TSI 3475) was modified to fit our needs.
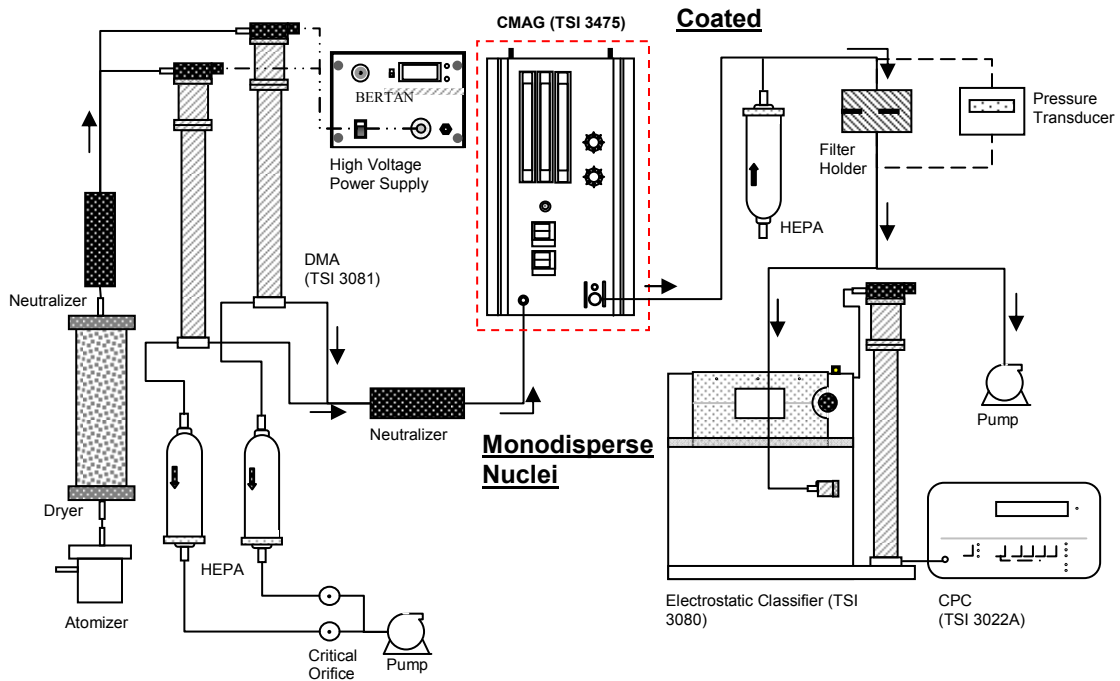
Figure 3.1   Schematic diagram of experimental system using the heating-evaporation-condensation process

A schematic diagram of the liquid-coated particle generation system is shown in the Fig. 3.1. The CMAG was originally designed to generate relatively monodisperse particles of high concentration by heterogeneous condensation on aerosol nuclei.

36

Therefore, it is a potential aerosol generator for producing liquid-coated particles by the heating-evaporation-condensation process. To better control the thickness of the liquid film on individual test particles, monodisperse particles were used as the nuclei (i.e., core particles) instead of the polydisperse particles generated by the original CMAG nuclei generator. Sodium chloride (NaCl) particles were produced by an external collison atomizer and classified by two identical long DMAs in parallel, which doubled the monodisperse NaCl nuclei flow rate and reduced the loading period by half. The mode size of the NaCl particles was selected by changing the voltage of the high voltage power supply connected to the DMAs, and the sheath flow rate of the DMAs was fixed at 6 lpm and controlled by a vacuum pump with critical orifices. To exclude the effect of particle charges, the classified monodisoerse particles were passed through a Po^{210} neutralizer to reach the Boltzmann charge equilibrium before mixing with the coating liquid vapor. The vapor was generated by heating the bulk coating liquid in the CMAG saturator. By adjusting the saturator temperature and the carrier gas flow rate through the saturator, the concentration of the vapor could be changed. As a result, the thicknesses of the liquid film coated on core particles, i.e. the liquid volume fracton of the liquid-coated particles, could then be varied. Before entering the condensation tube in the CMAG, both the aerosol stream and the liquid vapor were reheated to prevent non-uniform condensation due to flow mixing and to ensure the complete vaporization of the liquid. The condensation tube of the CMAG was a 14 inch-long cylindrical tube with an inner diameter of 0.75 inch. In this study, the temperature of the reheater was set at 300 ºC, and the total flow rate in the condensation tube was controlled around 3 lpm. Since the total aerosol flow rate for loading tests is larger than 3 lpm, additional clean air was introduced

to compensate for the flow difference. Two different gases, compressed air and nitrogen, were used as the carrier gas for the coating liquid vapor. The tests using compressed air mimicked particles produced in the environment. Because pure nitrogen reduces the oxidation of coating liquid, those with nitrogen were used to gain a fundamental understanding of liquid-coated particle loading behavior. For the loading tests using the first system, the mode size of the liquid-coated particles was maintained at 400 nm, and the liquid volume percentage was changed from 25% up to 90%. As seen in Fig. 3.2, the shapes of the size distributions are slightly varied due to the different operation conditions, but the GSD of the distributions are controlled in the range of 1.23 to 1.37, which can be considered as quasi-monodisperse.
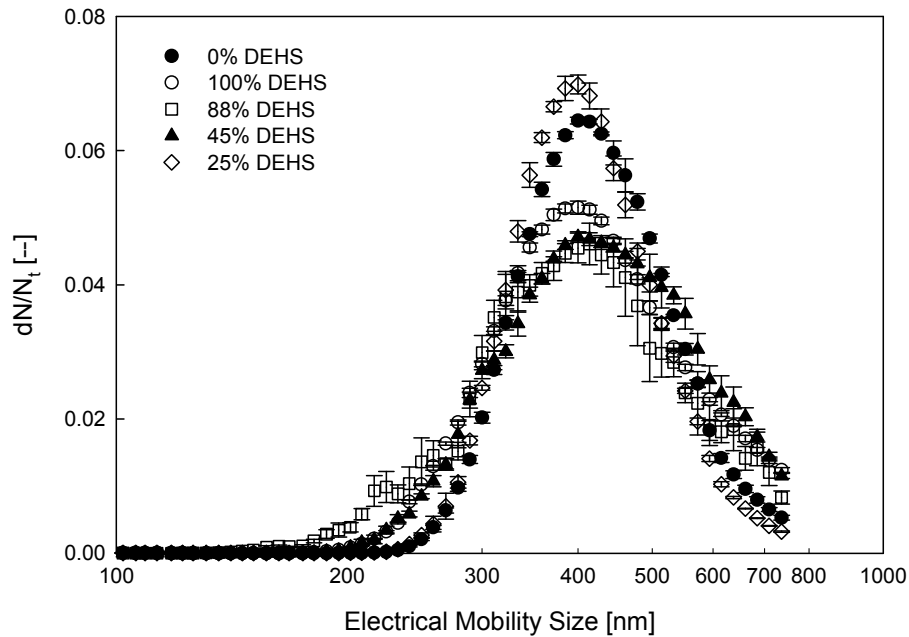
Figure 3.2   Liquid-coated particle size distributions generated by the first system: heating, evaporation, and condensation.

2.2   Particle Generation by the Co-solvent Method

The second liquid-coated particle generation system used a collison atomizer. Liquid-coated particles were generated by the co-solvent method. Potassium chloride (KCl) and the coating liquid were dissolved in water and 2-propanol separately, and latter mixed with each other in a volume ratio of 1:1. The well-mixed solution was then used as the solution in the collison atomizer to produce liquid-coated particles. By varying the KCl and coating liquid concentrations in the co-solvents, liquid-coated particles were produced in a fixed size with various liquid volume percentages. However, the solutes concentrations of the co-solvent can not be arbitrarily changed. Otherwise, the mixed solution would become an emulsion and create unstable particle size distributions of the liquid-coated particles.

The schematic diagram of the second liquid-coated particle generation system is shown in the Fig. 3.3.
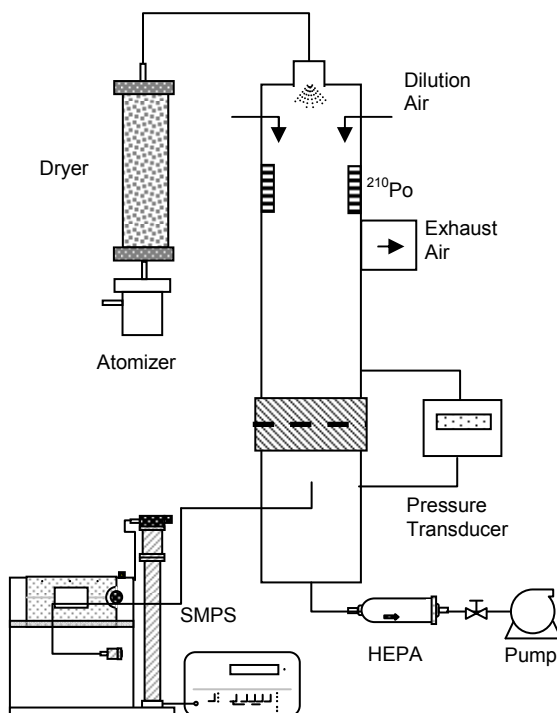
Figure 3.3   Schematic diagram of experimental system using the co-solvent method

Based on trial and error, 100 nm liquid-coated particles with different liquid volume percentages (100%, 88%, 50%, 25%, 0%) were produced. The particle size

distributions produced by this system were broader that those generated by the first system, and the GSDs varied slightly from 1.80 to 1.95 (Fig. 3.4).
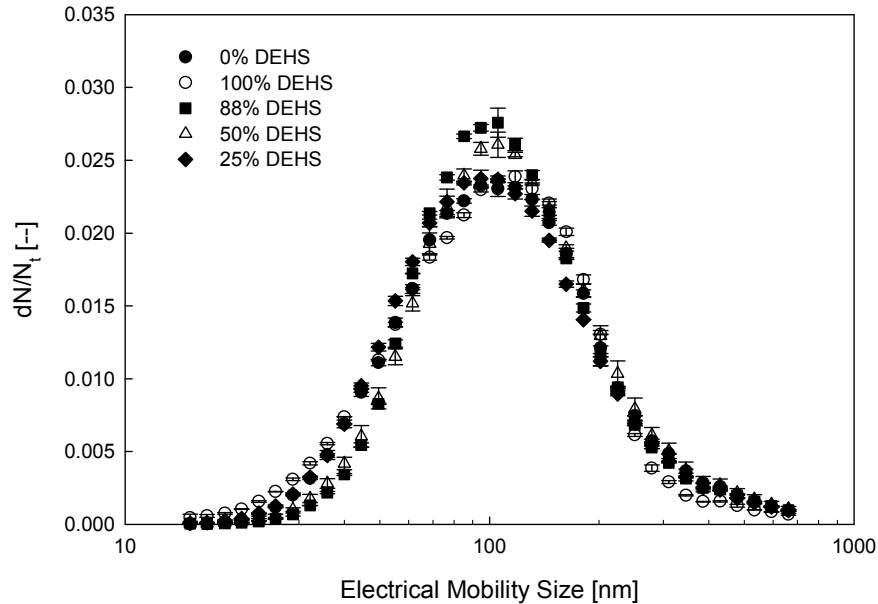
Figure 3.4   Liquid-coated particle size distributions generated by the co-solvent system

2.3   *Experimental Conditions*

For both systems, a high-efficiency glass fiber filter (filtration efficiency of 99.98% at 300 nm particle size) was used as the test medium. Additional polytetrafluoroethylene (PTFE) membrane filters (including untreated, hydrophilic, and oleophobic membrane filters) were tested for the co-solvent system to explore the effect of filter surface properties on the liquid-coated particle loading. The test filter sample was cut and seated in a 47 mm diameter in-line filter holder (Pall 1235), and the liquid-coated particles were fed from the top of the filter holder. The filter face velocity was kept at 11.0 cm/sec and controlled by a vacuum pump with an adjustable needle valve. Dioctyl

40

sebacate (DEHS) was chosen as the material for the coating liquid, and its surface tension and viscosity are 31.3 dyne/cm and 25.6×10^{-3} Pa-s. During the loading process, the particle distributions upstream and downstream of the test filters were measured by a SMPS (TSI 3936). Meanwhile, the pressure drop across the filter was monitored in-situ and recorded by a pressure transducer. The filter samples were weighed before and after loading tests to determine the loaded particle mass. Each loading case was repeated at least once to ensure its repeatability. For the reference, experimental runs were also performed to load the same filter media with completely liquid and completely solid particles of the same outer diameters.

3. Results and Discussion

The filter loading behavior is generally described by the pressure drop evolution curves, which are plotted in terms of pressure drop ratio or differential pressure drop versus the particle loading volume. The pressure drop ratio is defined as the ratio of the loaded-filter pressure drop (ΔP) to the filter initial pressure drop (ΔP_0), and the differential pressure drop is defined as the difference between these two values. Instead of the particle mass loaded on filters, the total volume of loaded particles was used for liquid-coated particle loading curves, because of the different densities of the core particle and the coating liquid material.

41

3.1   Pure Solid Particle Loading

Fig. 3.5a shows the pressure drop curves when the glass fiber filters were loaded with pure solid particles of four different diameters, 100 nm, 257 nm, 402 nm, and 547 nm. For the 100 nm case, the solid particles were not classified by the DMA, and the GSD (σ_g) of the size distribution was about 1.83. For the other three cases, the GSD (σ_g) was reduced to 1.23 due to electrostatic classification. Since the collection efficiency of the test filter was high, the downstream particle concentration was not detectable for all four particle sizes, even in the initial stage. Thus, surface filtration was expected to be the main process of the loading tests. This expectation was also confirmed by the linear behavior of the loading curves. In addition, the slope of the loading curves gradually decreases with increasing particle size. However, by multiplying the pressure drop by the square of particle size and a function of GSD, $\exp(\ln^2(\sigma_g))$, these four loading curves can be collapsed into one characteristic curve (Fig. 3.5b). The merged curves confirm the effect of particle size and polydispersity described in the general theory derived by Endo et al. (1998) [1] for solid particle loading in the dust cake regime.
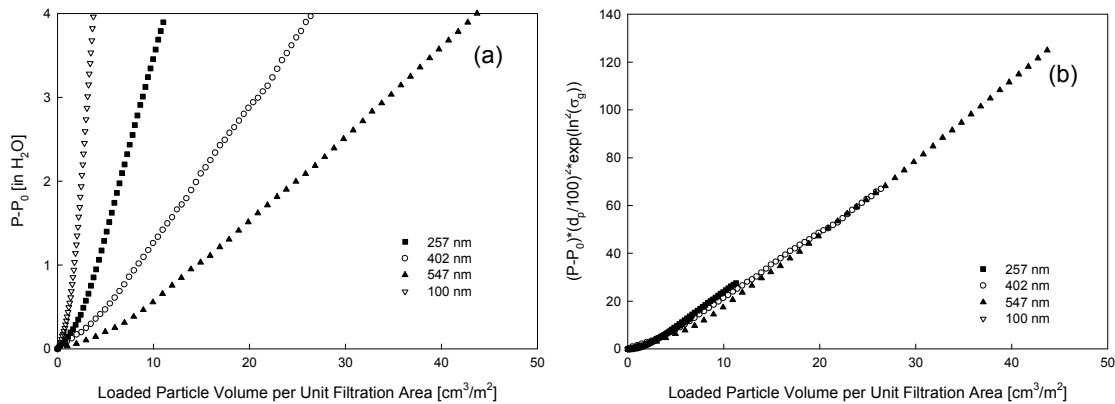
Figure 3.5a   Pressure drop evolution curves for the pure solid particle loading

Figure 3.5b   Normalized solid particle loading curves

3.2 Pure Liquid Particle Loading

The pure liquid particle loading tests were also performed under the same test conditions as those for pure solid particle testing, but the challenge particle sizes changed to 100 nm, 400 nm, and 2.5 μm. The corresponding GSDs of these three particle distributions were 1.92, 1.33, and 1.41. Contradictory to the distinct loading curves for solid particle loading, all three liquid loading curves overlapped each other without any correction (Fig. 3.6). In the other words, no size effect and no the distribution polydispersity effect was observed. Further, the characteristics of the loading curves for liquid particles are very different from those for solid particles.
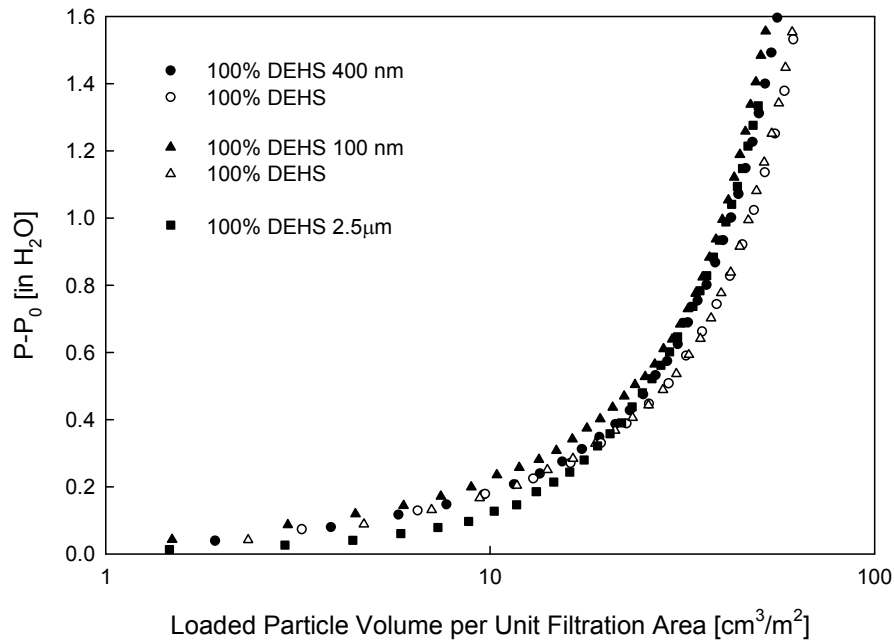
Figure 3.6   Pressure drop evolution curves for pure liquid particle loading

The pressure drop caused by the loaded liquid particles initially increases slowly and is much less than that caused by the solid particle of the same loaded volume, because that the collected liquid particles coalesce and freely move on the filter fiber

surface. For a low surface tension and low viscosity liquid, they may uniformly form a liquid film on the filter fiber. As a result, the effect of the particle size distribution in liquid particle loading is not as significant as that in solid particle loading. In addition, the air flow through the filter media was only moderately disturbed by the loaded liquid and led to lower pressure drop changes. However, as more liquid particle became loaded onto the filter, the liquid started to fill the void spacing among the fibers and radically raised the pressure drop. The exponential growth of the pressure drop did not stop until it reaches the threshold for the redistribution of loaded liquid in the filter matrix. This pressure drop threshold is typically much higher than the initial filter pressure drop. For the loading experiments performed with the condensation system, the pressure drop of a loaded filter is limited to within 2 times the initial filter pressure drop.

3.3 Loading Behavior of Submicron Liquid-coated Particles Generated by Heating-Evaporation-Condensation Method

For this part of the study, two different vapor carrier gases, compressed air and nitrogen, were separately used to bubbled through the CMAG saturator. Fig. 3.7 shows the loading result using compressed air as the DEHS vapor carrier gas. Compressed air was to demonstrate the filter performance when loaded liquid-coated particles in the ambient environment, where liquid oxidation is unavoidable. Liquid-coated particle with three different liquid volume percentages, 65%, 85% and 98%, were tested in this case. Note that the outer diameters of the test particles were kept nearly the same size, around 400 nm. As seen in Fig. 3.7, the characteristic shape of the loading curves for liquid-coated particles is similar to that for pure liquid particle loading. The pressure drop ratio

initially increases relatively slowly in a linear manner and then sharply increases when a certain critical loading volume is reached. This similar behavior is because the liquid volume percentage of the test particle is high.
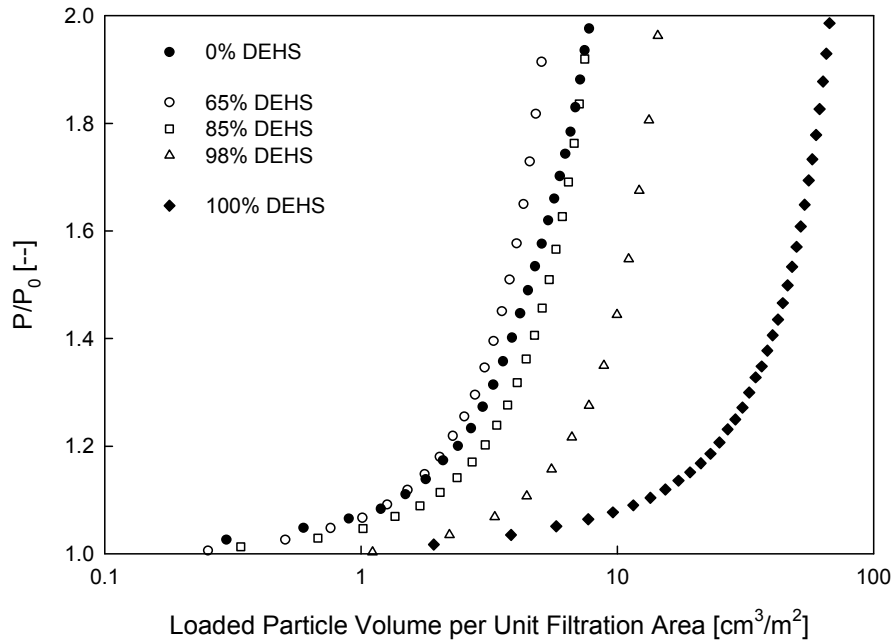
Figure 3.7   Loading curves for liquid-coated particles generated with compressed air carrier gas

In addition, the loading curves of different liquid volume percentages gradually shift toward the right-hand side of the plot as the liquid volume percentage increases. This shift can be explained by the increasing fluidity with increases in the liquid volume percentage of the liquid-coated particle. However, the curve of the 98% liquid volume fraction still deviates far from that of the pure liquid particle loading. In other words, the lifetime of the filters is dramatically reduced when they are loaded with liquid-coated particles. For the 85% loading curve, it initially located below the solid particle loading curve and later crosses the curve around a loaded volume of 7 cm^3/m^2. Moreover, the

loading curve of 65% liquid volume percentage is completely to the left side of the pure solid particle loading curve. One implication is that the loading curves could shift further toward the left when the liquid percentage of the particle varies from 0% to 65%, which is opposite to the rightward general trend of the loading curves as the liquid percentage increases from 65% to 100%.
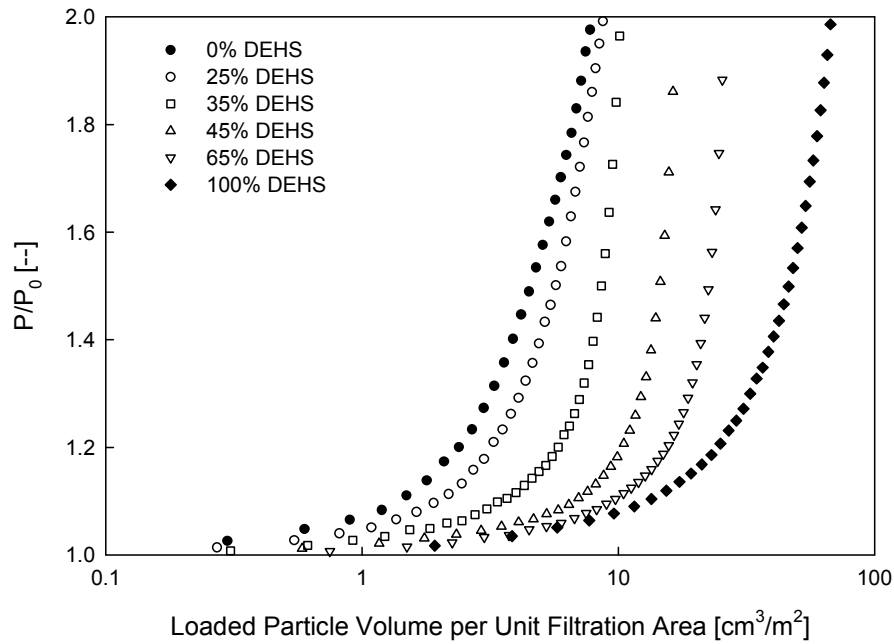
Figure 3.8   Loading curves for liquid-coated particles generated with nitrogen vapor carrier gas

We do not have a clear understanding about the factor resulting in such a leftward loading behaviour transition. It was, however, found that the viscosity of bulk DEHS liquid in the saturator was slightly increased after long term loading tests. At the same time, the other liquid properties, such as surface tension, may have changed, too. It is thus suspected that the change in liquid properties due to the liquid oxidation at the elevated temperature may be responsible for this unusual trend of loading curve transition. The

temperature of the saturator in the CMAG was always around the boiling point of the coating liquid. Contal et al. (2004) [2] have shown that the clogging of a filter loaded with glycerol is much faster than one loaded with DEHS. They attributed their observation to the higher surface tension of glycerol. Therefore, an increase in the viscosity or surface tension of the coating liquid due to oxidation in our loading experiment might move the loading curves to the left-hand side of where they otherwise would be. In addition, the transparent DEHS liquid became to brown after continuous heating in the saturator. Therefore, additional particles might have been generated by the reaction between the coating liquid and the compressed air, and contaminated the liquid-coated particles.

In the original CMAG manual, nitrogen was recommended as both the vapor carrier gas and the air source for the atomizer generating nuclei. However, for our filter loading test, the experimental time was normally more than 10 hours for each run, and the total flow rate was in the range of few liters per minute. Therefore, it was not economically feasible to perform the experiment completely with nitrogen. In this part of the study, only the vapor carrier gas was replaced with nitrogen to reduce changes in the coating liquid properties due to oxidation. After the loading tests, the viscosity of the bulk coating liquid was measured, and it was found that the variation of the viscosity before and after the tests was less than 3%. In addition, the color change of the bulk DEHS liquid in the saturator was less pronounced than before. Consequently, the liquid properties are believed to be more stable in the case of a nitrogen carrier, and the characteristics of the loading curves for liquid-coated particles are better controlled.

Five different liquid volume percentages, 25%, 35%, 45%, 65% and 90%, were tested in the case of nitrogen. As seen in Fig. 3.8, the characteristics of these loading curves are in general similar to that for pure liquid particle loading, except for the curve with a liquid volume fraction less than 35%. At 35%, it is observed that the liquid coated particle loading curves switch from linearly increasing to exponential growth. In other words, when the solid volume fraction is greater than 65%, the liquid-coated particle loading behaves more like that of solid particle loading. For curves where the liquid volume fraction was greater than 35%, their characteristics are similar to that of pure liquid particle loading. As the liquid percentage increases, the curves approach that of pure liquid particle loading. The trend was already observed for the cases using compressed air as the carrier gas, but the initial slopes of the liquid-coated particle loading curves obtained in this part of the study were all less than that of the pure solid particle loading curve. Compared to the cases using compressed air as carrier, more particle volume can be loaded on the filter for liquid-coated particles. In summary, the leftward and rightward transition behavior seen in the case of compressed air was not observed with nitrogen, and the loading curves continuously approach that of pure liquid particle loading as the liquid percentage increases. This experimental observation indirectly evidences the importance of the liquid properties on filter performance under liquid-coated particle loading. On the other hand, it also suggests the complexities of the loading behavior of liquid-coated particles in the real world.

3.4 Loading Behavior of Submicron Liquid-coated particle Generated by Co-solvent Method

As we found previously, the heating-evaporation-condensation system can change the coating liquid properties through the heating process during the continuous loading tests, and create uncertainties in the experimental results. In addition, although this system can produce quasi-monodisperse liquid-coated particles, the particle concentrations are relatively low due to the electrical classification for the upstream nuclei. Therefore, to generate high-concentration submicron liquid-coated particles with stable properties, the co-solvent method was used. Notice that the particle size distributions generated by this system are broader than those generated by the other system, since this generation process does not involve electrical classification. Moreover, the peak sizes of the particle distributions are kept round 100 nm, which is smaller than those generated by the first system.

As seen in Fig. 3.9, using the co-solvent method, no crossover between the solid particle loading curve and the liquid-coated particle loading curves is observed. The loading curves transits consistently from left to right. However, comparisons can not be made for these results and the experimental data from the condensation system, because the peak size and the GSD of the upstream challenge particle size distributions are different. The effect of particle size and the effect of the broadness of size distribution can not be differentiated in these two data sets.
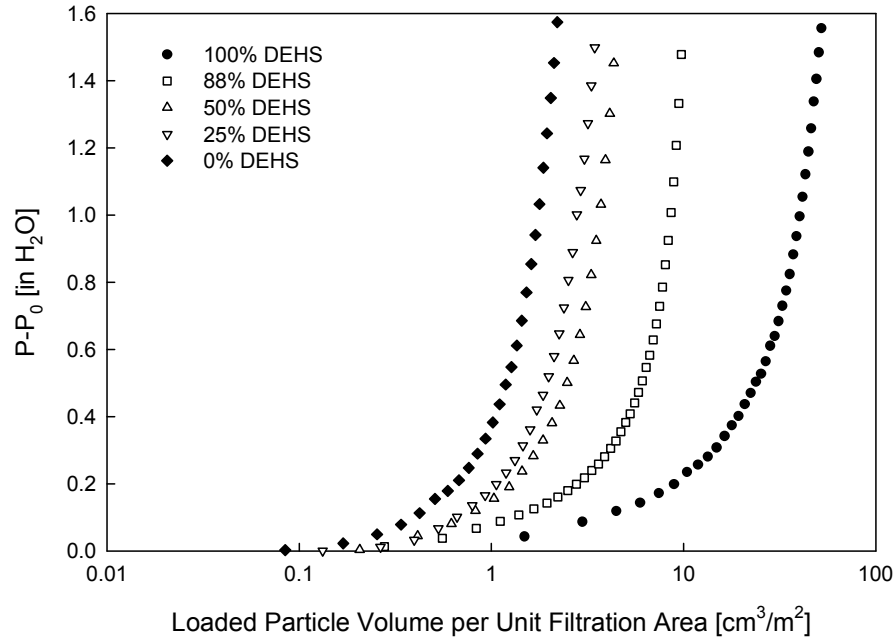
Figure 3.9   Loading curves for the glass fiber filter (using the co-solvent method)

To explore the effect of the filter surface properties, four different filters, including glass fiber filters, untreated PTFE membrane filters, hydrophilic PTFE membrane filters, and oleophobic PTFE membrane filers, were challenged by submicron liquid-coated particles of 20%, 50%, and 88% DEHS (by volume). The measured characteristic properties of these four filter media listed in Table 3.1. The glass fiber filter is a fibrous filter, and the other three PTFE filters are membrane filters. The pressure drop and the filter thickness of the untreated PTFE filter are similar to those of the glass fiber filter, but the packing density of the untreated PTFE filter is much higher than that of the glass fiber filter. In addition, for all three PTFE filters, their base weight, thickness, and packing density are all similar, but the initial pressure drops are different. Note that the Oleophobic PTFE filter's pressure drop is almost double that of the untreated PTFE filter. Therefore, it is suspected that the base weight, thickness, and

packing density of the PTFE filter are mainly contributed by the backing materials for supporting the membrane, and they can not represent the real characteristics of the membrane.

Table 3.1   Filter characteristic properties

Filter Media	Base Weight $[g/m^2]$	Thickness $[\mu m]$	Packing Density $[--]$	Initial P. $[in\ H_2O]$
Glass Fiber	64.0	435	0.056	2.75±0.1
Untreated PTFE	218.0	420	0.240	2.60±0.2
Hydrophilic PTFE	222.0	420	0.245	3.28±0.2
Oleophobic PTFE	218.0	420	0.240	5.34±0.2
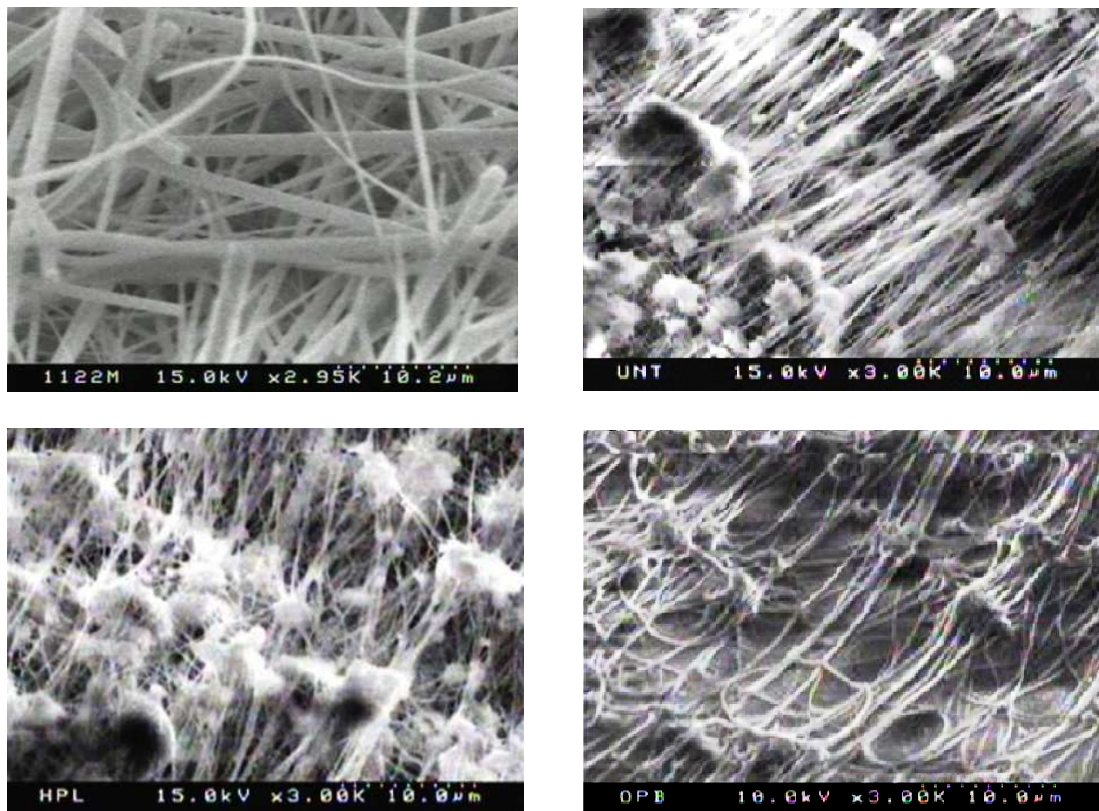
Figure 3.10   SEM pictures of (a.) glass fiber filter (b.) untreated PTFE filter (c.) hydrophilic PTFE filter (d.) oleophobic PTFE filter

Fig. 3.10 shows SEM pictures of clean filter samples at the same scale. The PTFE membrane filters have a structure very different from the fibrous filter. Since the general procedure to make PTFE membrane is heating and stretching a PTFE sheet, the typical microstructures of the PTFE membrane filters are a lot of fine fibers connecting with big clumps. The surface property of the original/untreated PTFE filter is hydrophobic, but by means of special treatment from the manufacturer it can become hydrophilic or oleophobic. As seen in Fig. 3.10, the structures of the untreated and hydrophilic PTFE filters are similar. However, the oleophobic PTFE filter has a different structure, which could explain the unique initial pressure drop observed for this filter.
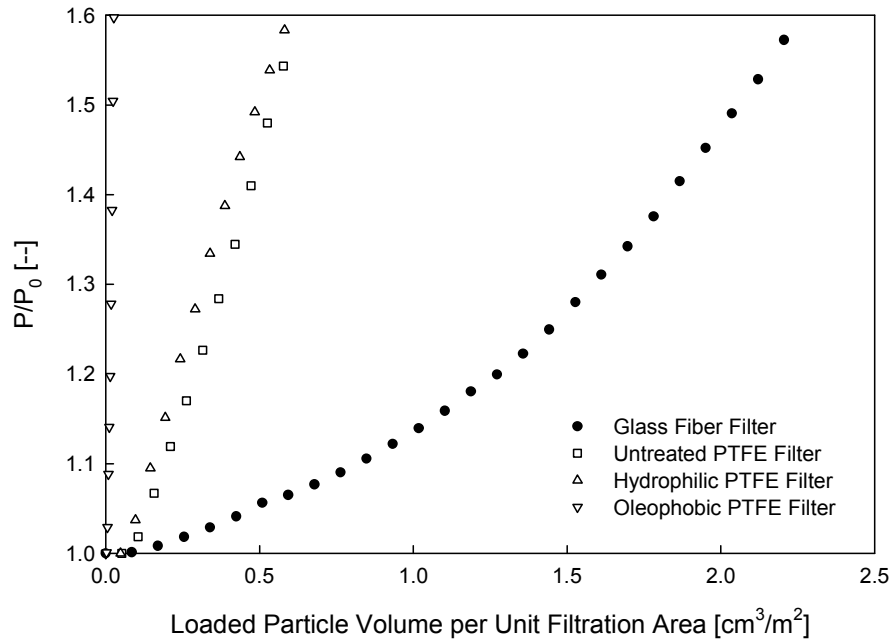
Figure 3.11   Solid particle loading curves for different filters

Considering the solid particle loading on the different filters, the four loading curves can be viewed as three groups. The pressure drop of the oleophobic PTFE filter shoots up very quickly when only a little particle volume is deposited on the filter. On the

other hand, the loading curve of the glass fiber filter is located at the very right of the plot. In between, similar loading behaviors are observed for the untreated and hydrophilic PTFE filters. It is believed that the effect of filter surface properties is not important for solid particle loading, and the different loading behaviors are due to the different filter microstructures. The glass fiber has the most porous structure, thus the pressure drop increases slower than the others as the solid particle loads on the filter. The concave up loading curve also reveals the filtration regime transits from depth filtration to transition filtration. The similar filter structures of the untreated and hydrophilic PTFE filters were shown previously, and their loading curves are similarly close. The oleophobic filter could have a higher packing density since its initial pressure drop is high. Therefore, its pressure drop increases much faster than the others.
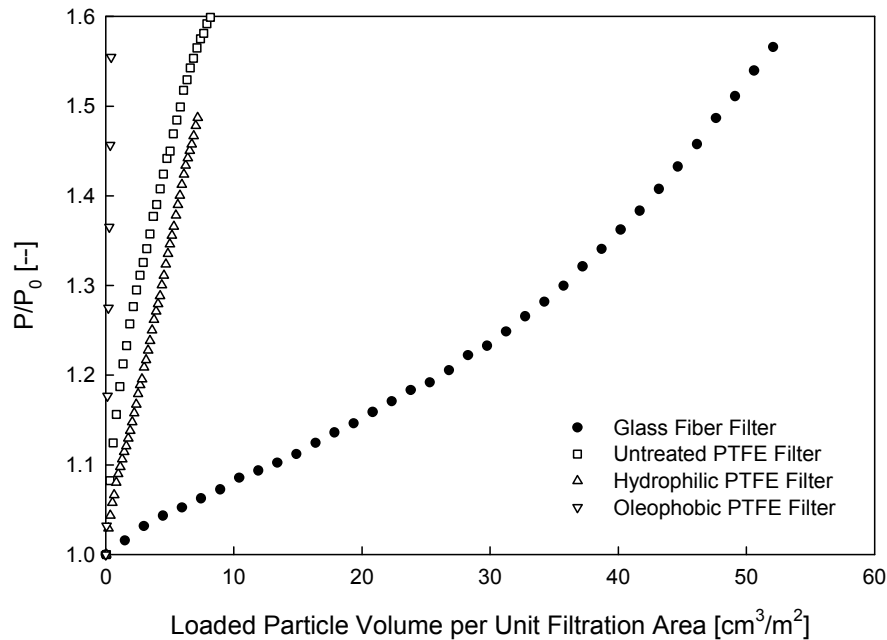
Figure 3.12   Liquid droplet loading curves for different filters

As seen in Fig. 3.12, the relative positions of the loading curves are similar to what we observed for solid particle loading. However, the morphologies of deposited liquid droplets and loaded solid particles on a filter are very different, due to the essential difference on the particle phase. Therefore, for liquid droplet loading, the loading behaviors can be simply explained by filter structures. The effect of filter surface properties should be significant as well, because they could change the shape of the deposited droplets or influence the coalescence behavior on filter fibers. Agranovski and Braddock, (1998) [3, 4] have done numerous experimental studies on wettable (hydrophilic) and non-wettable (hydrophobic) filters, and they conclude that aerosol is collected by the accumulation of relatively large droplets on and near the front face of the filter for the non-wettable filter, and the drainage is effected by the detachment of large drops from the front face of the filter. For the wettable fiber, the liquid collects throughout the filter in the form of thin liquid films on the surfaces of the filter fibers, and drainage occurs down the filter fibers through the thin liquid films. A similar scenario may occur for the oil droplets collected by the oleophobic and oleophilic PTFE filters.

4. Summary

Two different methods, the heating-evaporation-condensation and the co-solvent methods, were employed to generate submicron liquid-coated particles for filter loading tests. For the system using the heating-evaporation-condensation method, a liquid-coated particle generator was developed by modifying a TSI CMAG to produce liquid-coated particles of various liquid volume percentages. Liquid-coated particles were generated by mixing size-selected particle nuclei with coating liquid vapor by heterogeneous

condensation. The core particle material was sodium chloride, and the coating liquid was DEHS. Two different gases, compressed air and nitrogen, were employed to carry the coating liquid vapor. For both cases, as the liquid volume percentage increases, the loading curves all gradually approach to that of loading pure liquid particles. The transition processes, however, are different between these two cases. For compressed air, the loading curve first moves toward the left of the completely solid particle loading curve at lower liquid volume percentage. As the liquid volume percentage continuously increases, the curve then gradually approaches that for pure liquid particle loading. In other words, the performance of a filter loaded with liquid-coated particles could be either better or worse than that when loaded with solid particles, depending on the liquid volume fraction. It is suspected that this wandering transition is due to changes in the liquid properties and/or the additional particle contamination of the coating liquid, both caused by the oxidation at elevated temperature during the loading tests.

When nitrogen was replaced with compressed air as the carrier gas, as the liquid volume percentage increases the loading curves continuously moved to the right, in between the curves of pure solid particle loading and pure liquid particle loading. In addition, the negligible change of viscosity and color of the coating liquid was found before and after the loading experiments. These observations, therefore, indirectly evidence our supposition and demonstrate the significance of the liquid properties on the loading behavior of filters loaded with liquid-coated particles. The real-world implication of this finding is that it is very challenging to estimate the lifetime of filters when loaded with liquid-coated particles if the temporal variation of coating liquid properties is not

carefully characterized. Furthermore, liquid oxidation is an important issue that needs to be considered when using a CMAG to generate particles.

To avoid the changes in liquid properties during the loading tests, the co-solvent method was then used to generate submicron liquid-coated particles. Compared to the heating-evaporation-condensation method, the liquid properties of the coated particles generated by this method are more stable for long term loading experiments. In addition, the possibility of creating additional particle contamination by heating is eliminated, and it proved a reliable method for generating liquid-coated particles. The transition behavior of the loading curves is similar to the case of using nitrogen as the vapor carrier gas. However, the co-solvent method is limited by the intrinsic characteristics of the selected atomizer, such as the peak size and the GSD of the generated droplet distribution, and by the maximum solute concentration for making a homogeneous co-solvent.

Glass fiber filters, untreated filters, hydrophilic filters, and oleophobic filters were later tested for liquid-coated particles generated by the co-solvent method to study the effect of surface properties of the filter media. The general transition behavior for liquid–coated particles was observed for all four filter media, but the behavior depended on the filter medium. For the solid particle loading, the pressure drops for the test membrane filters increased faster than for the glass fiber filter when the same particle volume was loaded. This difference was caused by the different structures of the fibrous filter and the PTFE membrane filters, as the surface properties of filter are believed to be insignificant for solid particle loading. In the filtration studies of wettable and non-wettable filters [3, 4], it was found their filtration behaviors were very different for collecting mists. Therefore, the effect of filter surface properties, hydrophilic, hydrophobic or oleophobic,

is expected to be the same for liquid oil droplet loading. From the experimental results, the differences are observed for PTFE filters with different surface properties. However, we are unable to draw a solid conclusion about the effect of filter surface properties based on the experimental observations, since the filter structure of the oleophobic PTFE filter is quite different from the other two PTFE filters.

5. References

[1]   Endo, Y., Chen, D. R., and Pui, D. Y. H. (1998) Effects of particle polydispersity and shape factor during dust cake loading on air filters. *Powder Technology*, 98:241-249.

[2]   Contal, P., Simao, J., Thomas, D., Frising, T., Callé, S., Appert-Collin, J. C., and Bémer, D. (2004) Clogging of fibre filters by submicron droplets. Phenomena and influence of operating conditions. *J. Aerosol Sci.* 35, 263-278.

[3]   Agranovski, I. E., and Braddock, R. D. (1998) Filtration of liquid aerosols on wettable fibrous filters. *AIChE J.*, 44:2775-2783.

[4]   Agranovski, I. E., and Braddock, R. D. (1998) Filtration of liquid aerosols on non-wettable fibrous filters. *AIChE J.*, 44:2784-2790.

Chapter 4

Supermicron Liquid Coated Particle Loading

1. Introduction

In chapter 3, the general transition behavior of loading curves was characterized for polydisperse submicron liquid-coated particles. The characteristics of liquid-coated particles are different from those of solid or liquid particles, and the morphologies of liquid-coated particles deposited on filter fibers are hypothesized to vary with the volume percentage of the coating liquid. Therefore, the current pressure drop models for solid and/or liquid particle loading can not predict the pressure drop evolution for liquid-coated particle loading. In addition, Contal et al. (2004) [1] have found that the liquid properties, such as viscosity and surface tension, play an important role in pure liquid particle loading. Since the liquid of coated particles contributes part of the total pressure drop during the loading process, the loading curves should depend on the properties of the coating liquid as well.

In this chapter, supermicron liquid-coated particles were generated by the co-solvent method, which was previously proved to be reliable for long term loading tests, and loaded onto two different filter media. One was made of glass fiber, and the other was made of cellulose. To further investigate the transition behavior of the loading curves at the microscopic level, the morphologies of deposited particles coated with different volumes of liquid were examined under SEM. The influences of the face velocity, the particle size, the properties of the coating liquids, and the filter material were also studied by conducting several series of tests under different operation conditions. Furthermore, an empirical model is developed based on our experimental observations and results for the glass fiber filter and the cellulose filter. The model is able to simulate liquid-coated particle loading curves at up to four times the initial pressure drop at different liquid

volume percentages. In addition, the model also considers the viscosity of the coating liquid.

2. Experimental Methods
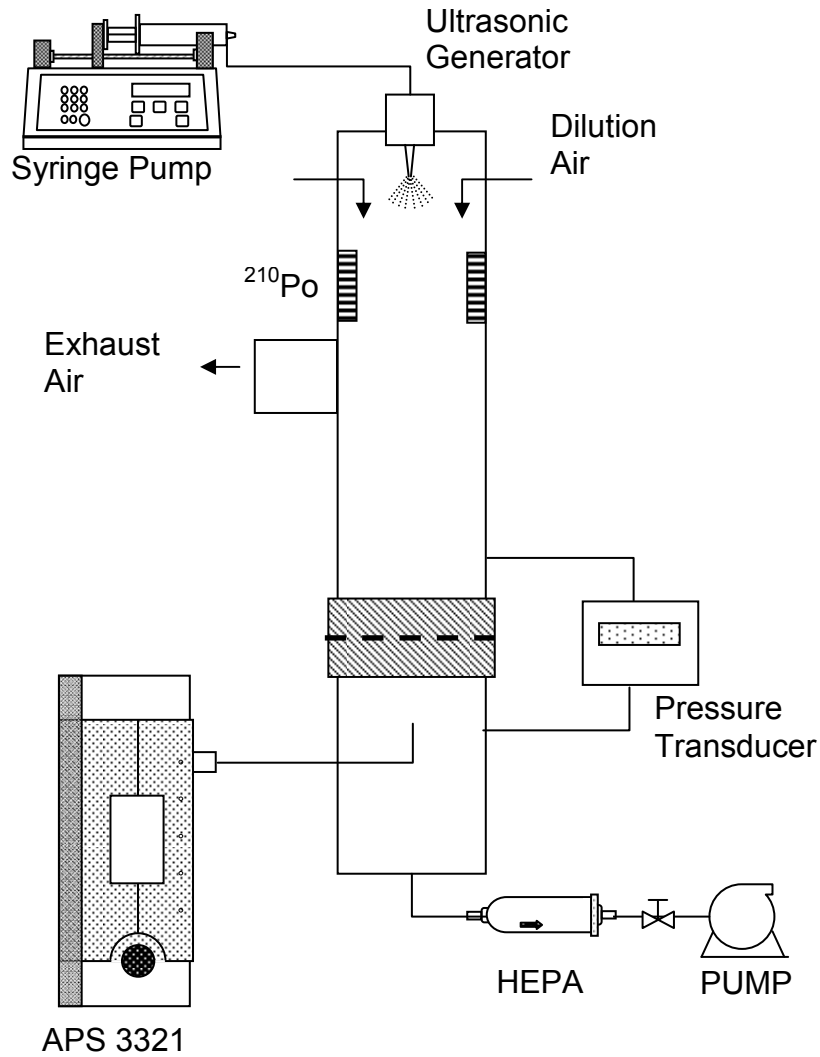
Figure 4.1   Schematic diagram of the experimental system

A schematic diagram of the experimental system used in this study is shown in Fig. 4.1. The system consists of three sections: the particle generation apparatus, the filter

test chamber, and the measurement instruments. In chapter 3, it was shown that using the heating-evaporation-condensation method to generate liquid-coated particles can change the coating liquid properties and raise uncertainties about the experimental results. Hence, the co-solvent method is employed to prepare liquid solutions for the generation of supermicron liquid-coated particles by an ultrasonic generator. The co-solvent method does not involve heating, thus the properties of the coating liquid on the test particles stay the same during filter loading experiments. To make the co-solvent, the coating liquid was dissolved in 2-propanol and then mixed with the potassium chloride (KCl) aqueous solution in a volume ratio of 1:1. The well mixed co-solvent was then delivered to ultrasonic particle generator (Sono-tek 8700) by a syringe pump (Harvard 70-2000) to produce supermicron liquid-coated particles. The ultrasonic nozzle is fixed at the top of the filter test chamber, and four Po^{210} strips were placed immediately next to the nozzle to reduce the level of electric charges on the generated droplets, lessening the transport loss of the droplets in the test chamber. Clean dry air was introduced from the sides of the chamber to carry the ultrasonically produced droplets and to evaporate their solvent, yielding liquid-coated particles for the loading experiments. Test filter media with a diameter of 2.75" were punched out from large sheets and placed in the homemade filter holder in the test chamber. The air flow rate passing through the test filter sample was controlled by a needle valve and monitored by a TSI flow meter (TSI 4043). During the loading process, an APS (Aerodynamic Particle Sizer, TSI 3321) and a pressure transducer (MKS 223BD) were used to measure the upstream and downstream particle size distributions and to record the dynamic pressure drop of a loaded filter, respectively. The evolutionary particle penetration at a particular size was derived from the ratio of the

downstream and upstream particle concentrations in the size bin of the APS-measured size distributions. It was later used to correct the accumulated loaded particle mass at the corresponding pressure drop.
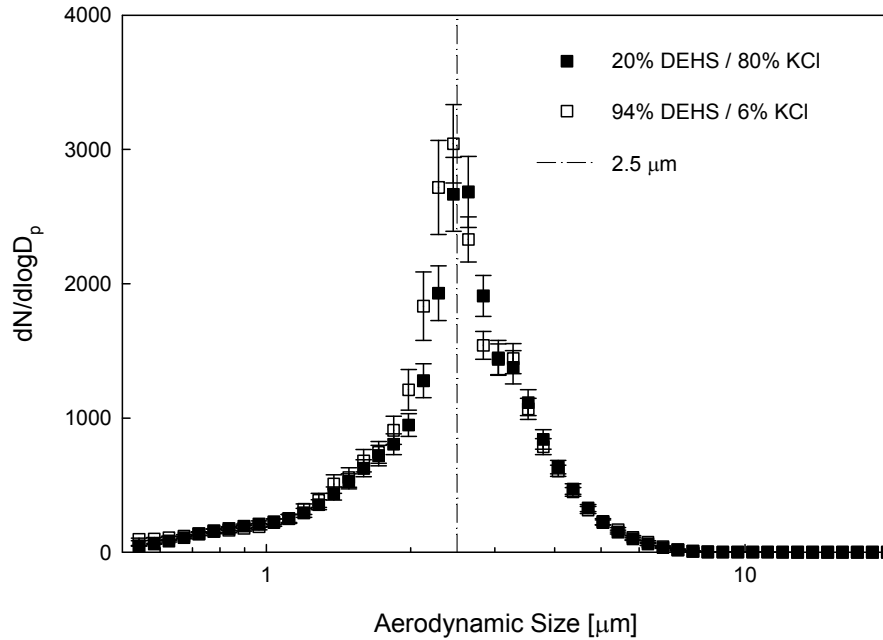
Figure 4.2   Typical particle size distributions for upstream liquid-coated particles

The mode sizes of liquid-coated particle distributions were kept the same for a series of loading experiments, while the liquid volume percentage was varied. The liquid volume percentage of the coated particle was varied from 20% to 94% by changing the relative concentration of the coating liquid to that of the KCl in the co-solvent. To explore the particle size effect on the liquid-coated particle loading, two different particle sizes, 2.5 μm and 5.0 μm, were tested at a face velocity of 11 cm/s. Figure 4.2 shows typical size distributions of the liquid-coated particle with two different liquid volume percentages, 20% and 94% DEHS. As seen in the figure, the shapes of the two distributions are similar, and the main peak sizes remain at 2.5 μm. The mass-based

GSDs of the particle size distributions are around 1.33, and they are considered as quasi-monodisperse. To further verify that the liquid was well coated on the particle, the fluorescent dye was doped into the coating liquid, and the generated particles were collected and inspected. Figure 4.3 shows pictures of the 20% and 94% DEHS-coated particles taken through a fluorescent microscope. It can be clearly seen that the core solid particles are well coated with DEHS under both extreme liquid volume percentages.
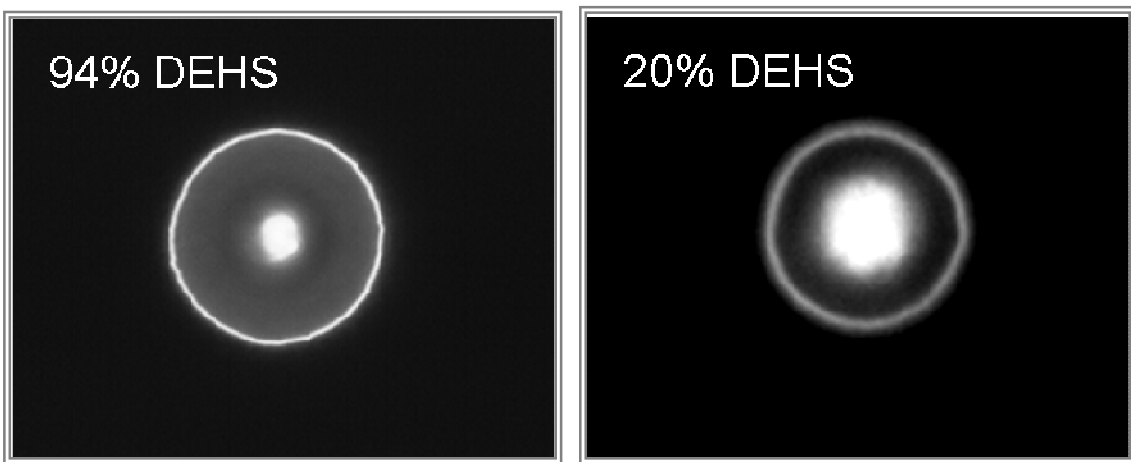
Figure 4.3   Liquid-coated particles viewed through a fluorescent microscope

To study the effect of coating liquid properties on the loading behavior, we tested four coating liquids, DEHS, light mineral oil, castor oil, and glycerol, with different surface tensions and viscosities. Their surface tension and viscosity were characterized by a vibro viscometer (A&D SV-10) and a tensiometer (KSV sigma 703D) in the lab, and the densities were provided by the manufacturers. The values are all listed in Table 4.1. DEHS, light mineral oil, and castor oil have similar surface tensions, but glycerol has a much higher value, almost double the others'. On the other hand, all of the viscosities are

different. Glycerol has the highest viscosity, followed by castor oil, mineral oil and DEHS.

Table 4.1   The properties of coating liquids

Liquid	Viscosity	Surface Tension	Density
	$[10^{-3}$Pa-s]	$[10^{-3}$N/m]	$[g/cm^3]$
DEHS	26.2	30.30	0.914
Light Mineral Oil	59.3	29.73	0.83
Castor Oil	1450	34.75	0.96
Glycerol	2410	63.75	1.262

Two low-efficiency filter media were tested in this study: glass fibers and cellulose. Their basic properties, including base weight, porosity, and filter thickness, were characterized and are listed in Table 4.2. The initial penetration curves of these two filter media were also measured, using APS for the supermicron size range and a scanning mobility particle sizer (SMPS, TSI Model 3936) for the submicron size range. As shown in Fig. 4.4, the maximum particle penetration sizes, MPPS, of both filters are around 0.3 μm. The penetrations at the MPPS were about 80% and 90% for the glass fiber filter and the cellulose filter, respectively. For reference, the initial filter pressure drops at a face velocity of 11 cm/sec were about 0.08 inch H_2O and 0.21 inch H_2O for the glass fiber filter and the cellulose filter.

The test filter sample was weighed before and after each run test using a microbalance (Denver Instrument SI-215D). The filter weighing was done after conditioning the medium in desiccants for at least 24 hours. The difference in the weights

before and after the loading test was then considered as the total particle mass collected by the test filter sample. Since the densities of the core particle and the coating liquids were generally different, the loaded particle mass was replaced by the loaded particle volume to characterize the liquid-coated particle loading behavior. The accumulated particle volume was derived as a function of loading time from the weighed total loaded volume and the time-dependent particle penetration data, with the assumption of a constant upstream particle concentration.

Table 4.2   Characteristics of the test filter media

Test Filter Medium	Basic Weight [g/m²]	Porosity [--]	Filter Thickness [mm]
Low Efficiency Cellulose	135.7	0.877	0.71
Low Efficiency Glass Fiber	112.3	0.904	0.45
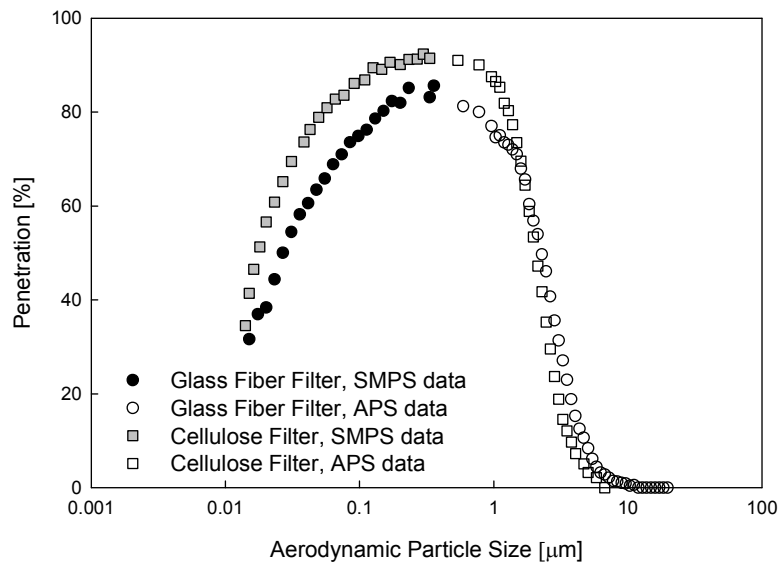
Figure 4.4   Initial penetration curves for the test filter media

66

3. Results and Discussion

3.1   Supermicron Pure Liquid Particle Loading

Before showing the loading behavior for liquid-coated particles, one extreme condition, pure liquid particle loading, is examined. The filtration of liquid particles is particularly important in the chemical industry, where waste liquid aerosols may be highly toxic or corrosive, such as in the manufacture of sulfuric acid [2]. Fig. 4.5 illustrates the loading behaviors for the glass fiber filter loaded with DEHS, light mineral oil, castor oil, and glycerol droplets of a similar size distribution under identical operation conditions. As seen in the figure, only the loading curve for glycerol stands out, and all the other three curves overlap. The profile of the merged loading curves shows the typical initial phase of liquid particle loading behavior. The pressure drop evolution curves are bent down for a while due to the redistribution of the collected liquid, and then rise up because of the formation of liquid bridges and films between filter fibers and at their intersections. For the distinct curve of glycerol, the pressure drop constantly increases, and the values are always higher than those caused by either DEHS or light mineral oil or castor oil. This behavior was also reported by Contal et al. (2004) [1], who attributed it to the high surface tension of glycerol. They summarized the work done by Briscoe et al. (1991) [3] and indicated that the liquid droplets with high surface tension/large contact angle would form a clamshell or a bead on fibers, and those with low surface tension/small contact angle form undulating shapes on fibers. Thus, the collected glycerol droplets would offer a specific area larger than those of a lower surface tension liquid. In addition, Contal et al. [1] also suspect liquid viscosity could play an important role on the

modification of the rearrangement within the structure of the filter. However, based on our experimental results, the liquids with the same surface tension but different viscosities ranging 26.2 to 1450 mPa-s, i.e., DEHS, light mineral oil, and castor, all behave similarly. The viscosity seems to have a negligible effect on pure liquid particles loaded on a glass fiber filter.
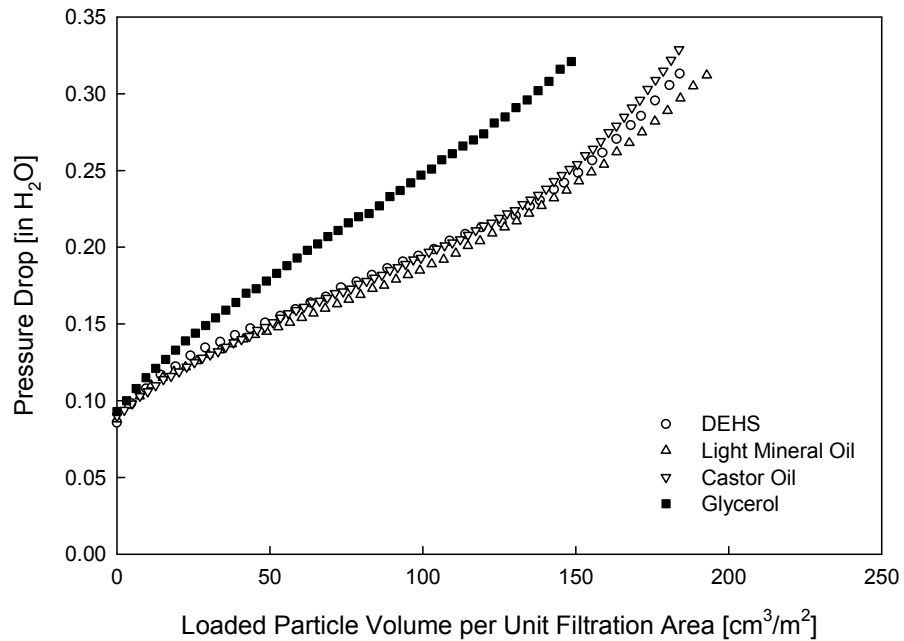
Figure 4.5   Liquid loading curves for the glass fiber filter

The same experiments were also performed on the cellulose filter. The shape and the relative positions of the loading curves are different from what we observed for the glass fiber filter. The initial slopes of the loading curves are much lower than those in the Fig. 4.5. The loading curve of glycerol is still on the far left-hand-side of the plot, i.e., the pressure drop rises more quickly than in the other cases, but now the curve of castor oil quickly separates from those of light mineral oil and DEHS. The curve of castor oil is located in between that of glycerol and those of DEHS and light mineral oil. Therefore,

the loading behaviors of different liquids on the cellulose filter can not be simply explained by the surface tension effect.

Cellulose is known to have a substantial intake of moisture [4] and the absorption of liquids may play an important role in the liquid loading behavior for cellulose filters. For the cases of DEHS and light mineral oil, since their viscosity and surface tension are low, the deposited droplets would be easily absorbed by cellulose filter fibers. Therefore, the rates of pressure drop increase of DEHS and light mineral oil for the cellulose filter are much smaller than those for the glass fiber filter. On the other hand, castor oil and glycerol have much higher viscosities, and their absorption by cellulose fibers may become more difficult. The loading curves of different liquids, following the order of their viscosity, move from right to left. The liquid viscosity effect must be considered for cellulose filters and other filter media that could absorb liquid.
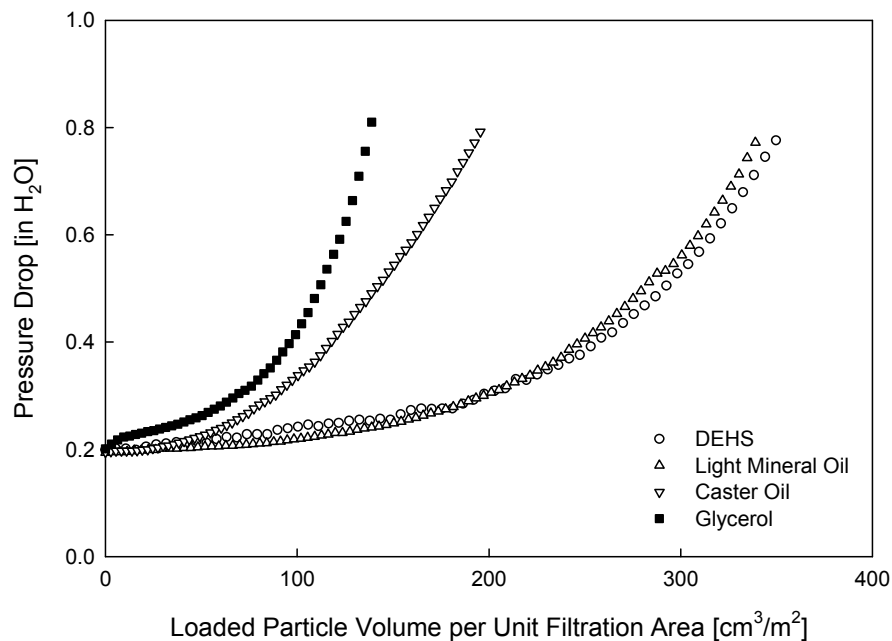
Figure 4.6   Liquid loading curves for the cellulose filter
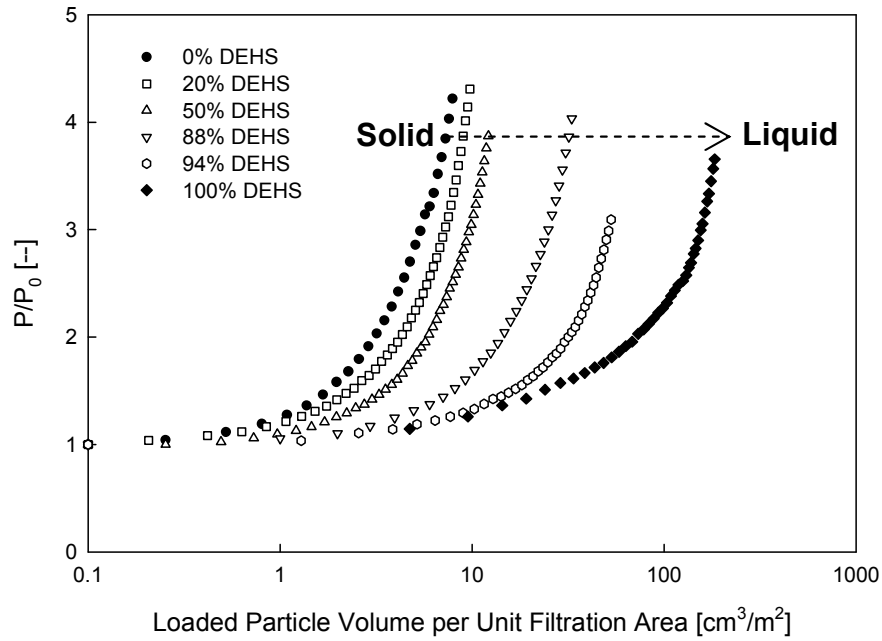
Figure 4.7   Loading curves for the glass fiber filter loaded with different DEHS coated particles
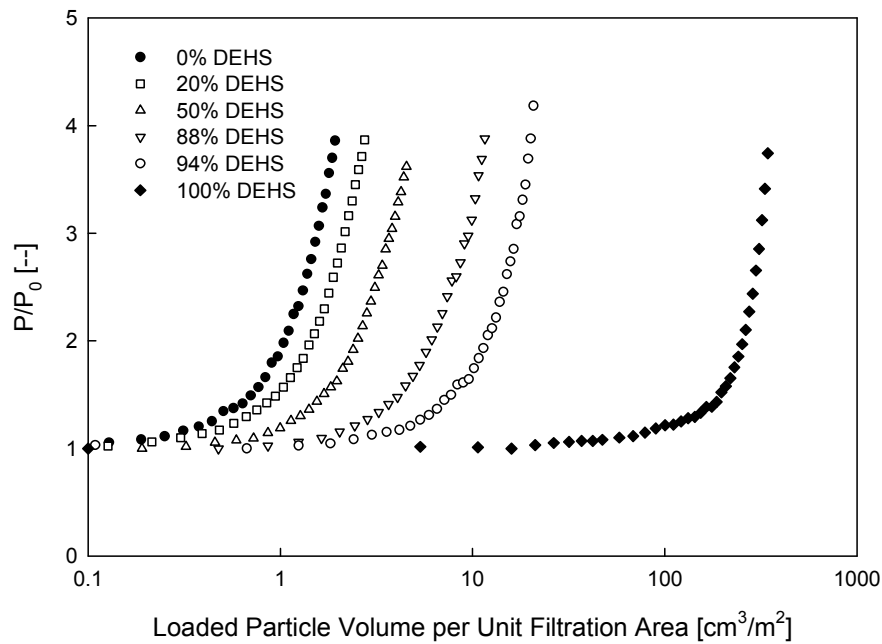
Figure 4.8   Loading curves for the cellulose filter loaded with different DEHS coated particles

Fig. 4.7 and Fig. 4.8 illustrate the loading curves for the 2.5 μm liquid-coated particle distributions with various percentages of DEHS loaded on the glass fiber filter and the cellulose filter, respectively. The results show in general that the loading behavior of liquid-coated particles transits from that of solid-only particle to that of liquid-only particles as the percentage of liquid volume of the particles increases. However, the transition between the two limiting cases (i.e., the solid-only and the liquid-only cases) is different for the cellulose filter and the glass fiber filter. For the glass fiber filter, the loading curves are more evenly distributed, between the two extreme, than the loading curves of the cellulose filter (Fig. 4.7 and 4.8). For the cellulose filter, the loading curves of the liquid-coated particles skew to the side of the curve of solid particles (Fig. 4.8). In the other words, a small percentage of solid mass in liquid-coated particles could dramatically change the loading behavior. Furthermore, compared to the case of the glass fiber filter, smaller rates of pressure drop increase are observed for the cellulose filter. These observations may be both due to the absorption characteristic of cellulose filters.

The general transition behavior of liquid-coated particle loading curves, moving from left to right in Figs 4.7 and 4.8, is believed due to the increase in fluidity of the deposited particles as the liquid percentage increases. To further verify this postulation, filters loaded with liquid-coated particles of 0%, 50%, 94%, and 100% DEHS, as well as clean filters were investigated under a Scanning Electron Microscope (SEM). As seen in series of SEM pictures of loaded glass fiber filters, when the liquid percentage increases from 50% to 94%, the morphology of loaded liquid-coated particles gets closer to that of loaded liquid droplets. Initially, when the deposited particles were purely solid, dendrite structures formed on the filter fibers and blocked the channels for air flow. As the liquid

percentage of the coated particles increased to 50%, the solid core particles still created dendrites, but the dendrites had shorter lengths and smaller diameters. Moreover, the coating liquids of the particles partially coated the filter fiber and partially created liquid bridges between the collected core particles or the particles and the fibers. Therefore, at the same loaded volume, the pressure drop of the 50% DEHS particle was less than that of the pure solid particle. In addition, we also suspected that the pressure drop was mainly caused by solid core of the liquid-coated particles within 50% liquid volume percentage. In Fig. 4.9a., the loaded particle volume is therefore multiplied by the solid volume percentage, and the loading curves for the liquid percentages less than 50% all converge within a narrow range. This directly evidences that under low coating percentages the main contributor of the pressure drop is the solid core of the liquid-coated particle. The deviations of these corrected curves may be due to the size effect of the core particles, which will be discussed in a later section.

For the case of 94% DEHS, the collected particles either uniformly distributed on the glass fibers or coalesced and became large unduloid droplets. No particle dendrites were observed, and the solid core particles were all trapped in the coating liquid films. This mixed solid and liquid film could turn out to exhibit a microscopic debris film flow on filter fibers. In addition, compared to the case of 50% DEHS, more liquid is coated on the glass fibers. However, compared to the case of 100% DEHS, fewer liquid films are observed between the fiber spacing. It is suspected that both observations are because of the small solid core of the coated particle. The core particle used in this study is KCl, and its density is about twice the densities of all the tested coating liquids. For a low viscosity liquid, such as DEHS, the solid core particles could be moved by gravity and then break

72

up liquid films between the fibers. On the other hand, these core particles also serve as filler material in the debris flow to make the filter fibers hold more coating liquid.

As well as the transition behavior, the morphologies of the deposited liquid-coated particles on the cellulose filter are different from those on the glass fiber filter. Previously, in the section describing pure liquid particle loading, we mentioned that cellulose filter can absorb liquids. Hence, when the liquid-coated particles are loaded on the cellulose filter, part of the coating liquid is absorbed by the cellulose fibers. As a result, similar to the case of the glass fiber filter, the solid core of the deposited coated particles would contribute most of the pressure drop for the loading cases of less-coated particles. As seen in Fig. 4.9b., the loading curves for coating liquid volume percentage less than 50% almost merge into one, when we use the loaded solid volume instead of the total loaded volume. However, at higher liquid percentages, the unabsorbed part of the coating liquid becomes more important by filling void spaces between collected particles and filter fibers or even by carrying the core particles. Therefore, this volume correction method can not collapse all loading curves together. In addition, compared to the glass fiber filter loaded with the same 94% DEHS particles, the shapes of collected particle clusters on the cellulose filter are more irregular and less enveloped by liquids. This may also due to absorption by cellulose material, and may then explain why the liquid-coated particle loading curves stay close to the solid particle loading curve for the cellulose filter.

In addition to the experimental observations, theoretically the liquid bridge formed between collected particles or between particles and filter fibers could significantly affect the loading behaviors of liquid-coated particles. Nevertheless, it is difficult to quantify the effect of liquid bridging because measurements of the contact

angle between the coating liquid and the collected particle or the filter fiber are tricky. Therefore, only a qualitative description is given here. The liquid bridges can both generate static capillary force to strengthen the particle dendrite structure and create dynamic viscous force to resist particle movement. The capillary force is the cohesive force accounting for both the surface tension acting around the perimeter of the bridge cross section and for the pressure difference caused by the curvature of the air-liquid interface [5]. Both the surface tension force and the suction force due to pressure difference are proportional to liquid surface tension. The viscous force is caused by the liquid viscosity, and acts only when particles move.

Since the interaction of liquid-coated particles is somewhat similar to the wet granulation process, it is believed that some findings in wet granulation studies are applicable in our case. The state of liquid saturation or liquid content in wet granulation can be interchangeable with the liquid volume percentage in our study. The capillary force would increase with increasing liquid volume percentage and reach a maximum value at a certain liquid volume percentage [6] (Holm et al., 1985). The viscous force is less significant at low liquid volume percentage and low collision velocity [5]. Therefore, once the liquid volume percentage exceeds a threshold, the deposited liquid-coated particles are expected to move rather than to form particle dendrites. At that point, viscous force could play an important role, and the frictional forces between particles may be involved as well. Based on our experimental results, this threshold could be 50% for DEHS. It is interesting to note that, in the field of food processing research, Servais, Jones, and Roberts (2002) [7] also stated "a 50% (volume) total solid concentration

suspension of non-interacting spherical particles can double in viscosity as the solid is increased by a few percent".

In summary, the system of filter fibers and liquid-coated particles is very complex. The interaction is related to capillary, viscous, and frictional forces, and their relative importance depends highly on the conditions, such as liquid volume percentage, core particle polydispersity, liquid properties, etc..
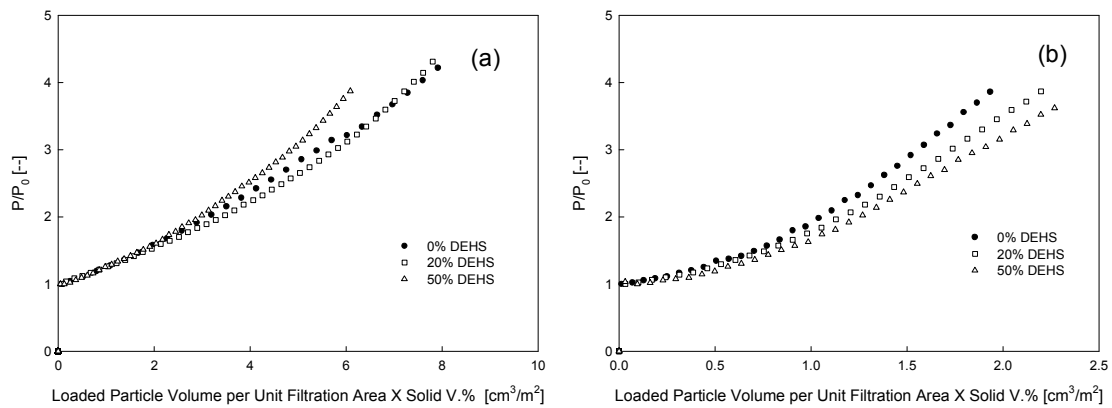
Figure 4.9a   Loading curves for the glass fiber filter re-plotted using loaded solid particle volume as x-axis

Figure 4.9b   Loading curves for the cellulose filter re-plotted using loaded solid particle volume as x-axis
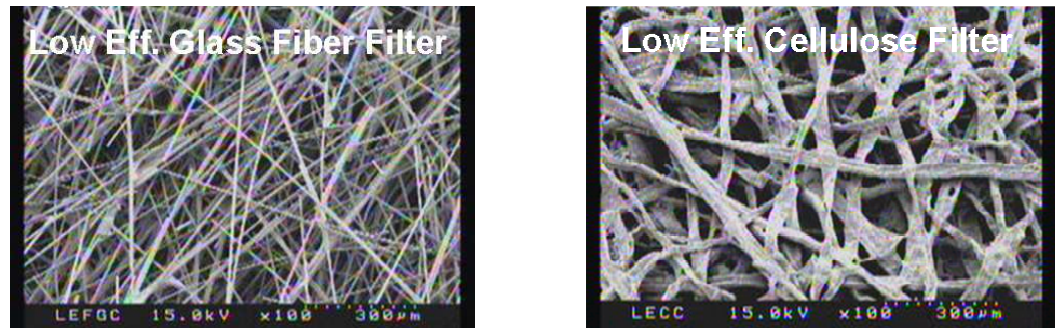
Figure 4.10a SEM pictures of a clean glass fiber filter and a clean cellulose filter
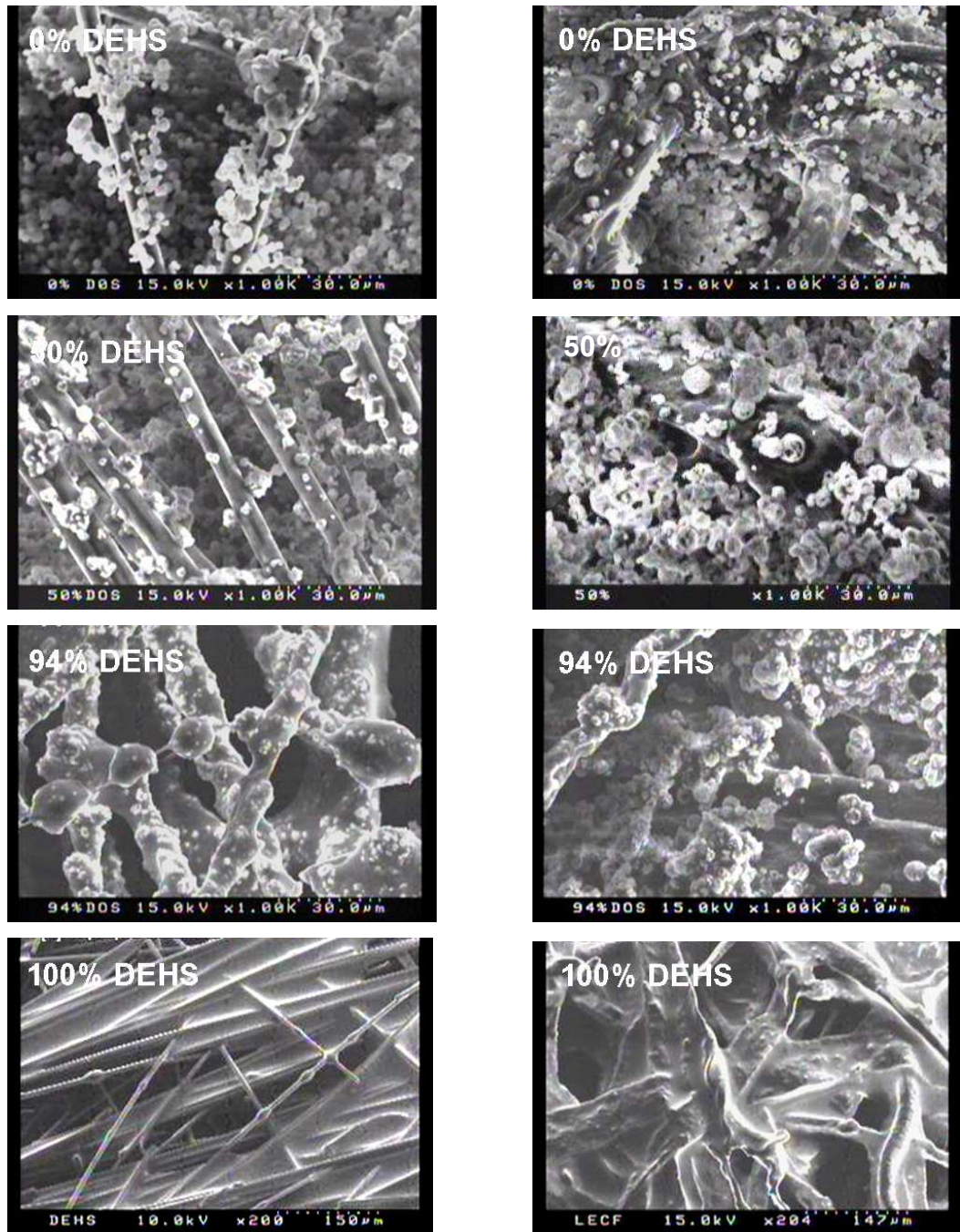
Figure 4.10b SEM pictures of loaded glass fiber filters (left column) and loaded cellulose filters (right column)

3.3 Influence of Face Velocity

Face velocity is an important factor in both solid and liquid particle loading, because it can either change the filtration mechanism or influence the morphology of deposited particles or droplets. For solid particle loading, Takagaki (2006) [8] has reviewed many studies [9-16] and concluded the basic shape of loading curves does not significantly change with face velocity varies from 1 to 100 cm/s. In most cases, the curve can collapse in a single line when the pressure drop is divided by the face velocity.

For liquid particle loading, only Contal et al. (2004) [1] and Charvet, Gonthier, and Gonze (2008) [17] have studied the face velocity effect, and both of them reported similar observations. The liquid particle loading curves behave similarly at different velocities from 2.5 to 40 cm/s, but the exponential growth of pressure drop is located at a smaller loaded mass at a higher velocity. However, in terms of the filter resistance, the curves seem to be independent of the filtration velocities before reaching the saturation/critical mass (m_{cr}), which is the mass coinciding with the sharp rise in pressure drop. Beyond m_{cr}, the higher the velocity, the lower the filter resistance is observed. Both of these two research groups suggest the coalesce filters to be operated under high face velocities, which is opposite to the general understanding of particulate filters.

In this study, pure DEHS droplets and 50% DEHS coated particles were loaded on the cellulose filter under three different velocities, 5, 11, and 20 cm/s, to study the influence of face velocity on liquid-coated particle loading. To verify the filter was operated in the laminar flow regime, the pressure drops of the clean cellulose filter were measured under four different velocities within the test range. It is seen that the pressure

drop is linearly proportional to the face velocity (Fig. 4.11), and the behavior follows
Darcy's law.
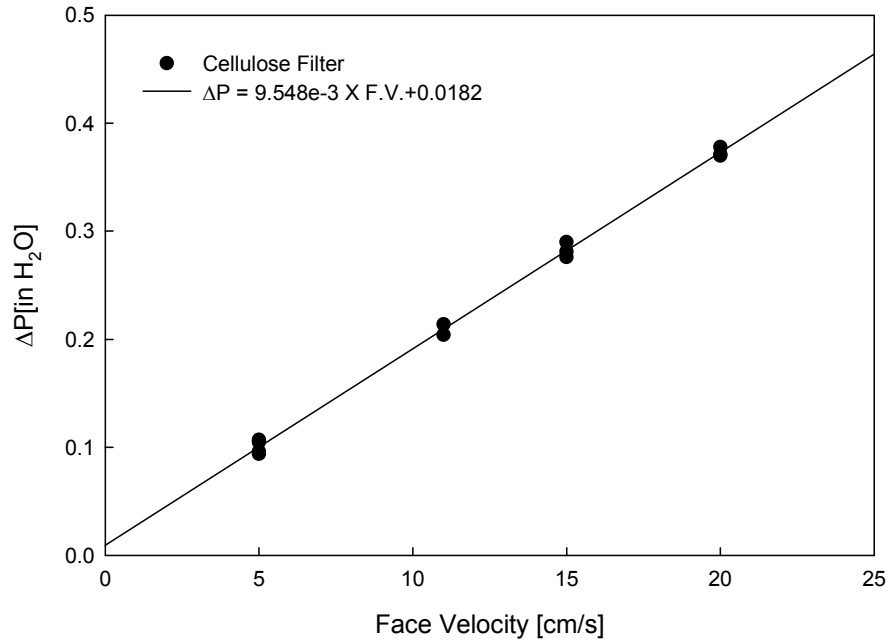
Figure 4.11   Pressure drops of a clean cellulose filter under different face velocities

The data shown in Fig. 4.12 and Fig. 4.13 are presented in terms of pressure drop
ratio, not the values of pressure drop. Therefore, the curves are already scaled with the
face velocity through division by the initial pressure drop. The physical meaning of the
pressure drop ratio is thus similar to the filter resistance used in the previous studies. As
seen in Fig. 4.12, the discrepancies between the curves of pure DEHS loading are
negligible under different velocities, even beyond the critical loading volume. This is
somewhat different from the filter resistance results reported by Contal et al. (2004) [1]
and Charvet, Gonthier, and Gonze (2008) [18]. We believe the different observations are
due to the different filter material used in the liquid loading tests. Although they do not
indicate the filter material in their studies, we suspect from the SEM pictures in Contal et

al.'s paper that the filters are fiber glass or other non-absorbing material. Since our tested cellulose filter could absorb the loaded liquid droplets, the resistance change due to face velocity was expected to be minor. Moreover, in this study the loading tests did not reach the pseudo-equilibrium stage. It is believed that divergence of the loading curves may be observed when the filter is further loaded with more liquid droplets.
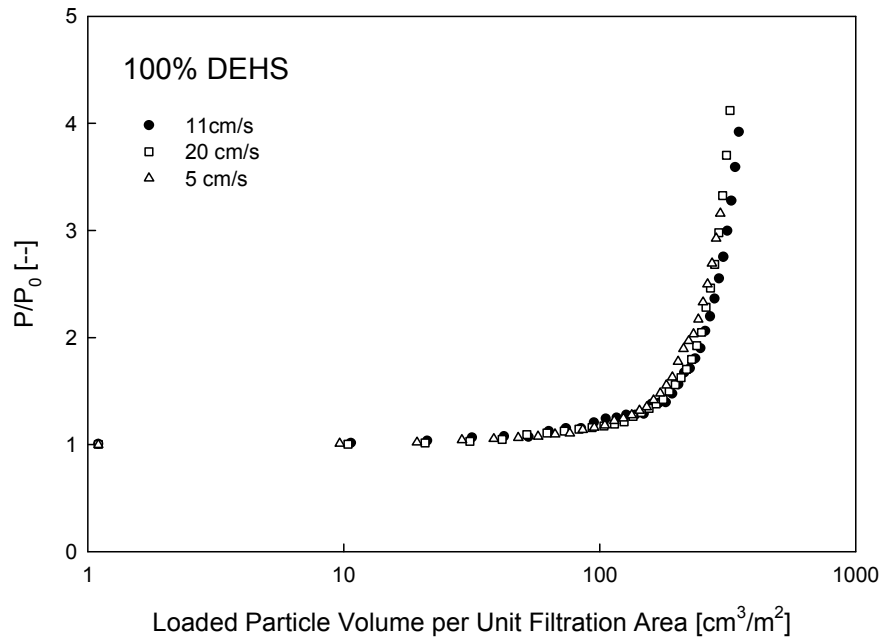
Figure 4.12   Loading curves for a cellulose filter loaded with 2.5μm DEHS droplets under different face velocities

For the 50% DEHS coated particles, the loading curves under different velocities overlap (Fig. 4.13). As verified previously, the pressure drop is mainly caused by the core particles in this case. It is therefore believed that the particle dendrite structures do not alter much when the face velocity varies from 5 to 20 cm/s, which may be because the tested velocities are either too low or too high. Since DEHS is considered low viscosity liquid, the tested velocity could be high enough to move the core particles. In other words, the viscous force due to the liquid bridges may not resist the air drag force, but more

79

experiments need to be performed. In addition, the coated liquid could further lubricate inter-particle contact and reduce the fractional forces depending on the particle size and the broadness of the distribution, as was reported by Iveson et al. (2001) [5] previously in their review of the wet granulation process. For a high viscosity coating liquid and for filters made of non-absorbing material, such as glass fiber, different behaviors may be seen.
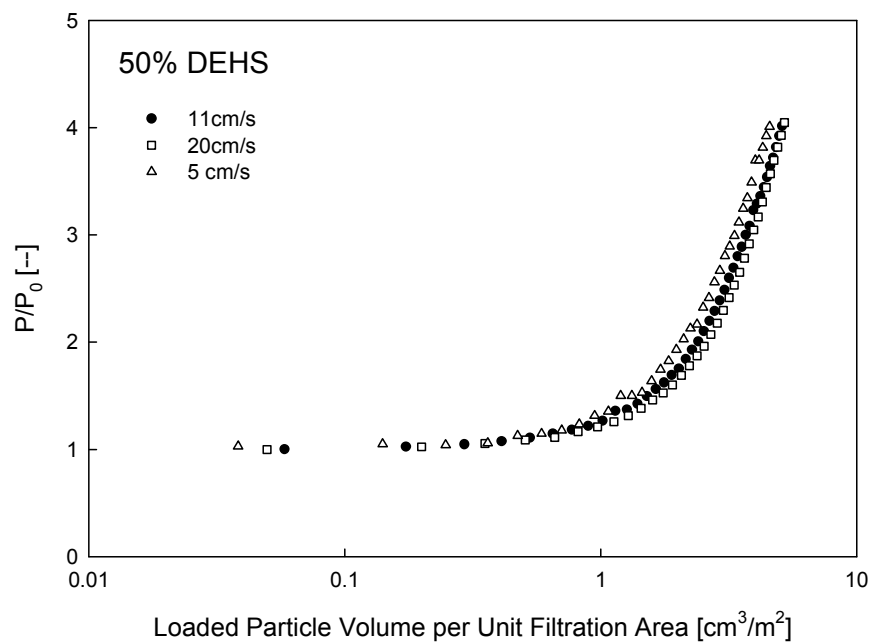
Figure 4.13 Loading curves for a cellulose filter loaded with 2.5μm 50% DEHS coated particles under different face velocities

3.4   Influence of Particle Size

Figure 4.14a shows the two different size distributions generated for liquid-coated particle loading. In the number base, one has the mode size at 2.5 μm, and the other has the mode size at 5.0 μm. To compare their shapes, the particle size in x-axis is further divided by the mode size. It can be seen (Fig. 4.14b) that their normalized profiles are in general similar. Both have the mass-based GSDs around 1.33. However, the 5.0 μm distribution is slightly asymmetric and has a significant long tail on the left side.
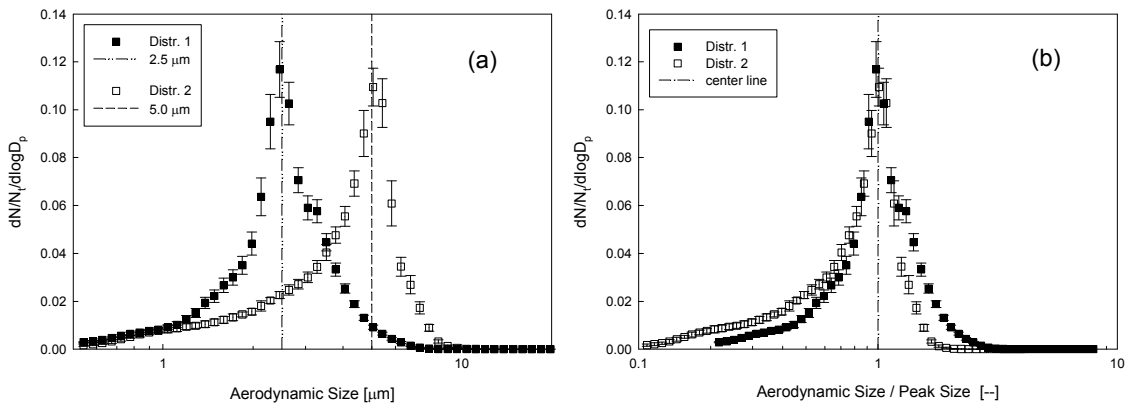
Figure 4.14a Typical 2.5 μm and 5.0 μm particle size distributions

Figure 4.14b Normalized 2.5 μm and 5.0 μm particle size distributions

As found previously for the glass fiber filter and the cellulose filter, loading curves of liquid volume percentages less than 50% can fall within a narrow range when the total loaded volume is multiplied by the solid volume percentage. As seen in Fig. 4.15 and Fig. 4.16, similar behaviors are also observed for the 5.0 μm challenge distribution. For both the glass fiber filter and the cellulose filter, the curves are grouped together when the pressure drop ratio is plotted versus the loaded solid volume. Furthermore, the slopes of the loading curves for 2.5 μm particles are higher than those for 5.0 μm particles. It is known that at the same loaded volume smaller particles can offer more

surface area, therefore a sharper gradient of the loading curves is found for 2.5 μm particles. In addition, the curve of 50% coated particles is usually located at the top of the group for each cases. This can be explained by the size effect of the core particle. The corresponding core particle diameter ratios of the 0%, 20%, and 50% coated particle are 100%, 93%, and 79%, hence higher pressure drop is found for 50% coated particles at the same loaded volume.
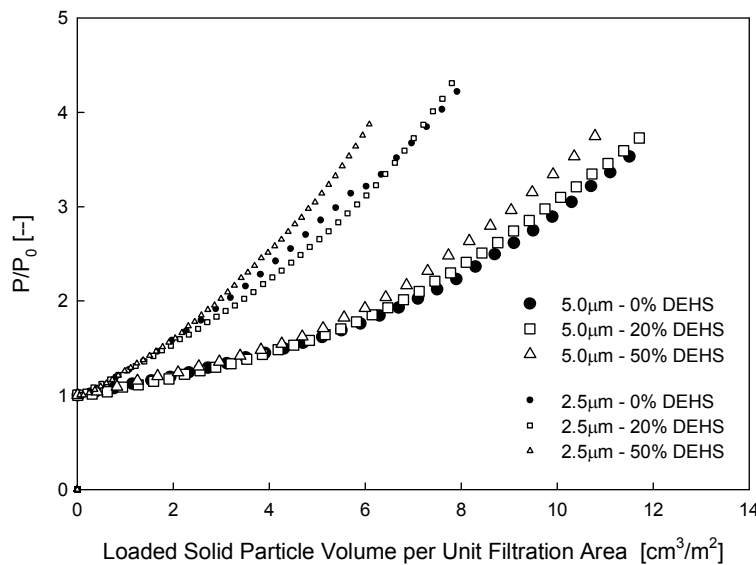
Figure 4.15   Loading curves (<50% liquid volume percentage) for the glass fiber filter loaded with 2.5 μm and 5.0 μm DEHS coated particles (using the loaded solid particle volume as the x-axis)

For the cellulose filter, the shape of the loading curves changed when the particle size was increased to 5.0 μm (Fig. 4.16). These loading curves are slightly bend down when the loaded solid volume reaches 4 cm^3/m^2, due to the filter structure of the tested cellulose filter, which is very non-uniform and has many melted clumps. According to Chen et al. (2001) [16], a filter medium with melted clumps generally has concave down loading curves, which confirms our observation. The initial fast pressure drop increase is

attributed to filling of filter cavities surrounded by the melted clumps of needle-felt filter fibers. Once the particle deposition enters the dust-cake loading phase, the steepness of the loading curve is gradually reduced. Similar behavior is expected for the 2.5 μm distribution when the loaded volume exceeds a certain critical value.
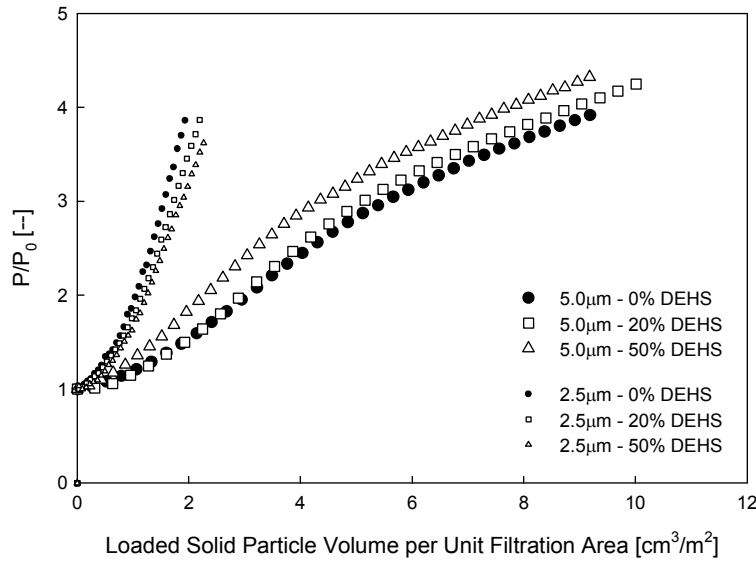
Figure 4.16   Loading curves (<50% liquid volume percentage) for the cellulose filter loaded with 2.5 μm and 5.0 μm DEHS coated particles (using the loaded solid particle volume as the x-axis)

Under the assumption that total drag force is attributed to the added surface of solid core particles, the pressure drop across the loaded filter should be proportional to the total surface area of loaded solid particles. To verify this postulation, the figures are further re-plotted with the total loaded particle surface area as the x-axis. As seen in Fig. 4.17, now two groups merge into one for the case of the glass fiber filter. However, in Fig. 4.18, the two groups of the loading curves for the cellulose filters are still slightly separate. Particles could still be deposited in the funneled zones in the filter medium, and

the sharp initial slope of the concave-down loading curve is not caused only by the deposited particles.
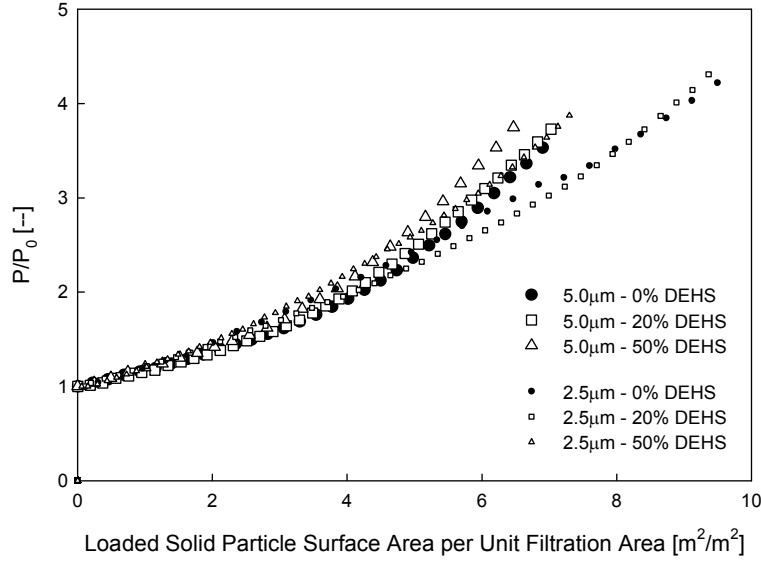
Figure 4.17 Loading curves (<50% liquid volume percentage) for the glass fiber filter loaded with 2.5 μm and 5.0 μm DEHS coated particles (using the loaded solid particle surface area as the x-axis)
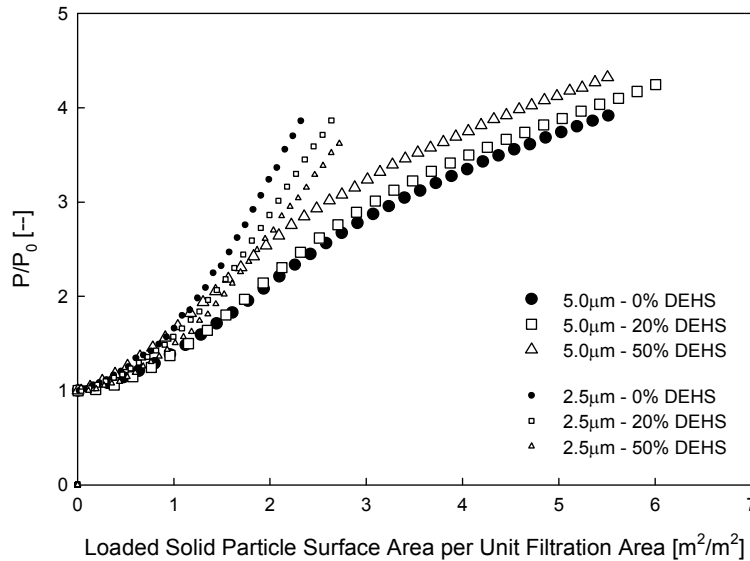
Figure 4.18 Loading curves (<50% liquid volume percentage) for the cellulose filter loaded with 2.5 μm and 5.0 μm DEHS coated particles (using the loaded solid particle surface area as the x-axis)

For the liquid volume percentages higher than 88%, the particle size effect is different, since the coating liquid is involved in the pressure drop evolution. For both the glass fiber and cellulose filter, increasing the loaded particle size shifts the loading curves of 88% and 94% DEHS closer that one of 100% DEHS (Fig. 4.19 and Fig. 4.20). Since the liquid volume percentage is high enough that the loaded coated particle can coalesce and become a colloidal suspension, this shift may be caused by the change of the relative viscosity of the colloidal suspension. Farris (1968) [18] has shown that increasing the broadness and number of modes of the particle size distribution can considerably reduce the viscosity of the suspension. The pure liquid loading curves remained unchanged for the cellulose filter loaded with droplets of two different sizes. However, for the glass fiber filter, the 2.5 μm pure liquid loading curve deviated a little from the 5.0 μm curve in the initial loading phase, and they merge together at a higher loaded volume. Researchers have generally believed the size effect is not important for pure liquid particle loading, since the deposited droplets would coalesce eventually. The minor difference observed in pure liquid particle loading in Fig. 4.19 can be attributed to the non-uniformity of the filter media and to experimental error.
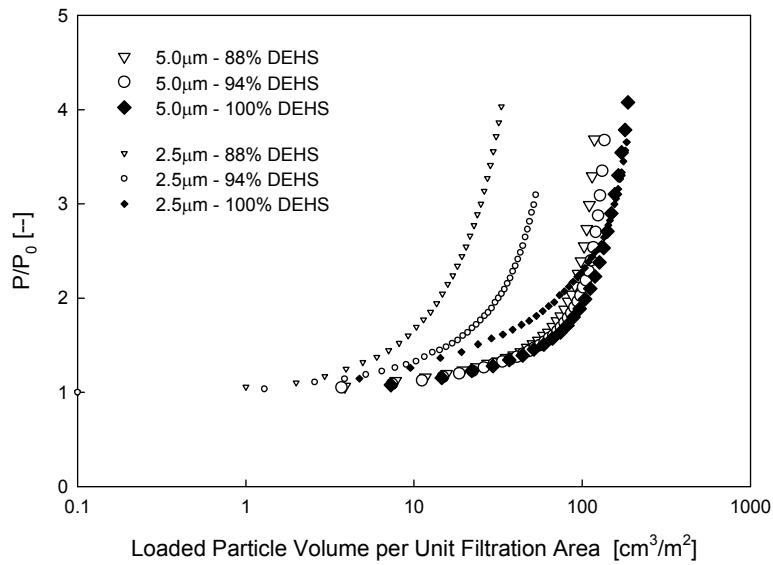
Figure 4.19 Loading curves (>50% liquid volume percentage) for the glass fiber filter loaded with 2.5 μm and 5.0 μm DEHS coated particles
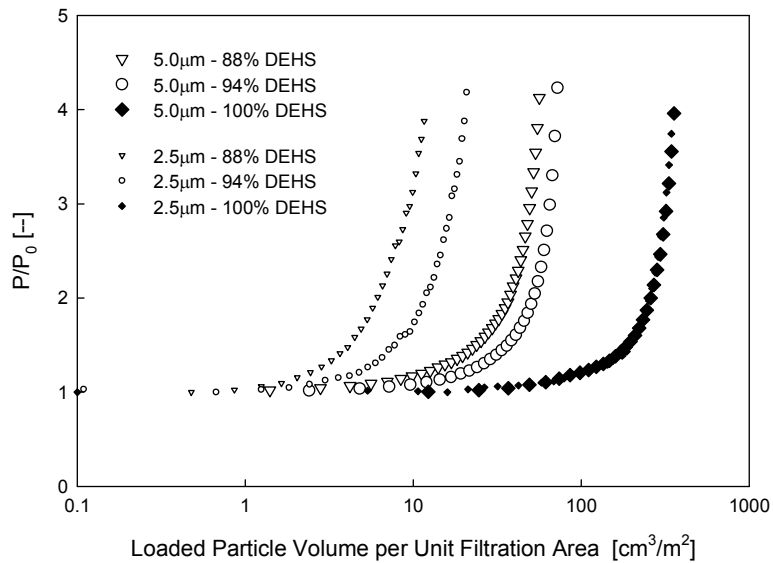
Figure 4.20 Loading curves (>50% liquid volume percentage) for the cellulose filter loaded with 2.5 μm and 5.0 μm DEHS coated particles

3.5   Influence of Liquid Properties (Surface Tension and Viscosity)

In 2004, Contal et al. [1] found the physico-chemical characteristics of liquid, such as surface tension and viscosity, can influence pure liquid particle loading, however they did not make further conclusions based on their experimental data. The liquid properties are also believed to be crucial for liquid-coated particle loading, since the coating liquid could either support the particle dendrite through formation of liquid bridges or carry the deposited core particles along filter fibers. Therefore, in addition to DEHS, light mineral oil, castor oil, and glycerol were used as coating liquid to study the effect of surface tension and viscosity.

Previously, as found in the SEM pictures, liquid bridges could be established between the deposited core particles and the filter fibers when the liquid volume percentage of the coated particles is low. The capillary force resulting from the liquid bridges can strengthen the particle dendrites and make the structure straighter. In addition, it is known that capillary force is proportional to liquid surface tension. Therefore, particles coated with a liquid of high surface tension would create more porous dendrite structure and have less pressure drop change during the loading process. This supposition is confirmed by the behavior shown in Fig. 4.21 for the glass fiber filter and in Fig. 4.22 for the cellulose filter. The loading curve of 50% glycerol coated particles, located at right-hand side of the plot, stands out among all loading curves and the glycerol's surface tension is almost double that of the other three coating liquids. On the other hand, although DEHS, light mineral oil, and castor oil have different viscosities, their loading curves all overlap because of their similar surface tensions. This observation again

demonstrates the importance of the liquid surface tension for liquid-coated particle loading.
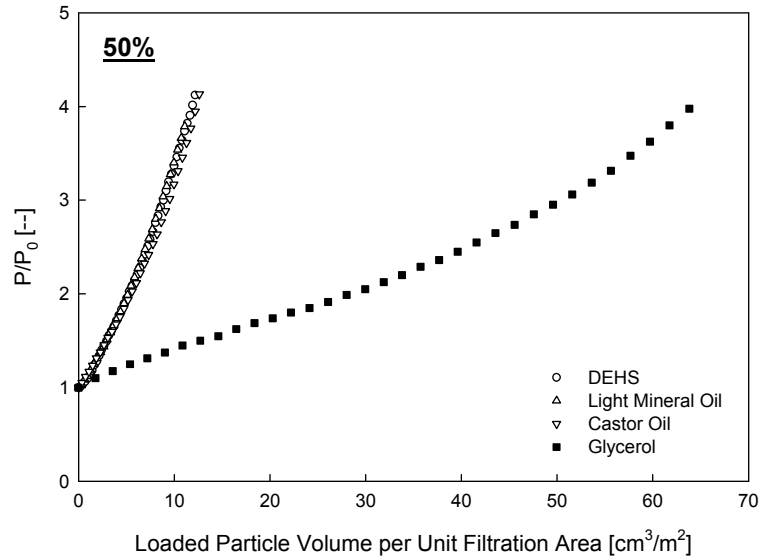
Figure 4.21   Loading curves for the glass fiber filter loaded with particles coated with 50% liquid
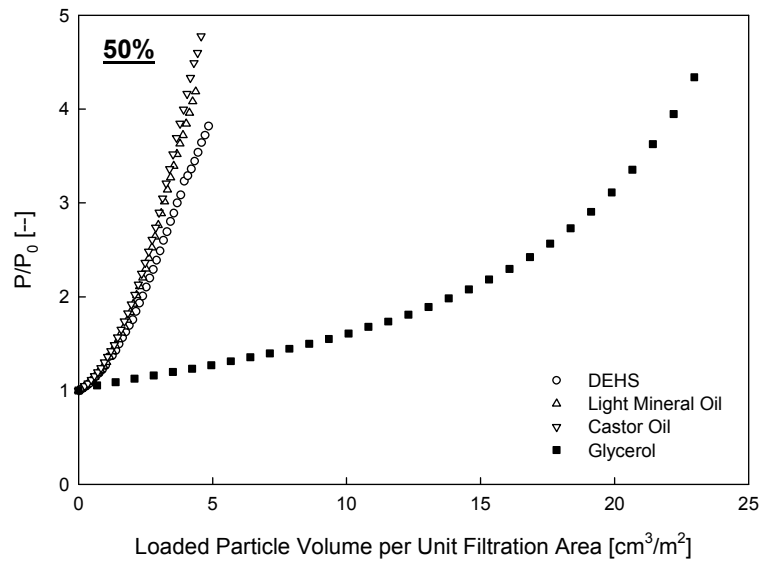
Figure 4.22   Loading curves for the cellulose filter loaded with particles coated with 50% liquid

88

When the loaded particles were coated with more liquid, such as 88% coated particles, the relative positions of the loading curves of different coating liquids changed somewhat. Similar to the case of less coated particles, the curve of glycerol coated particles is still located at the very right for both the glass fiber filter and the cellulose filter (Fig. 4.23, and Fig. 4.24). However, the other three loading curves are now spread out, and the sequence of the curves from left to right follows the order of liquid viscosity. This is due to forces other than capillary force. The fractional force and the viscous force become dominant for the interaction between the 88% coated particles, and the viscous force is directly related to the liquid viscosity. In this liquid volume percentage, the loaded particles might be relocated due to air drag or gravity, and the viscous force and fractional force work against these movements. Therefore, the effect of liquid viscosity is significant for liquid-coated particle loading at a high liquid coating percentage. However, recall that, as previously shown in Fig. 4.5 and 4.6, when the liquid volume percentage is 100%, the effect of the surface tension becomes important again, and the sequence of the curves is totally reversed. In addition, for the cellulose filter the effect of liquid viscosity is still considerable but in different ways, because the cellulose filter can absorb coating liquid.
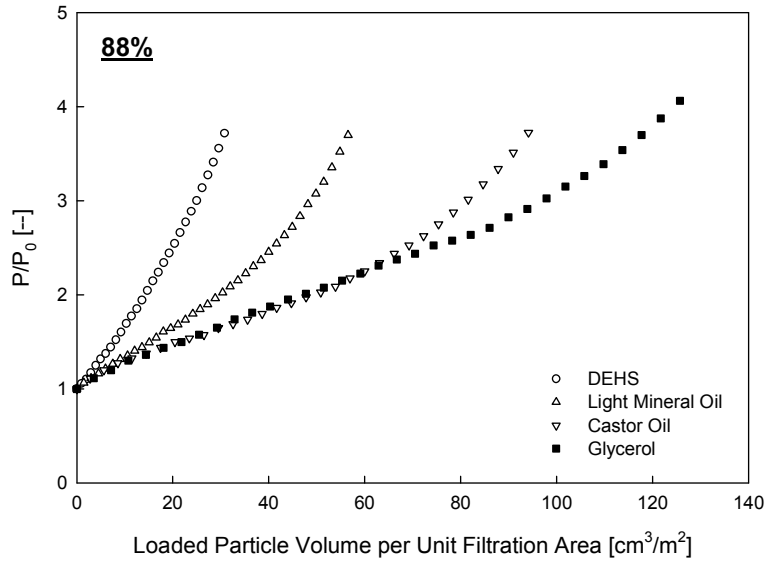
Figure 4.23   Loading curves for the glass fiber filter loaded with particles coated with 88% liquid
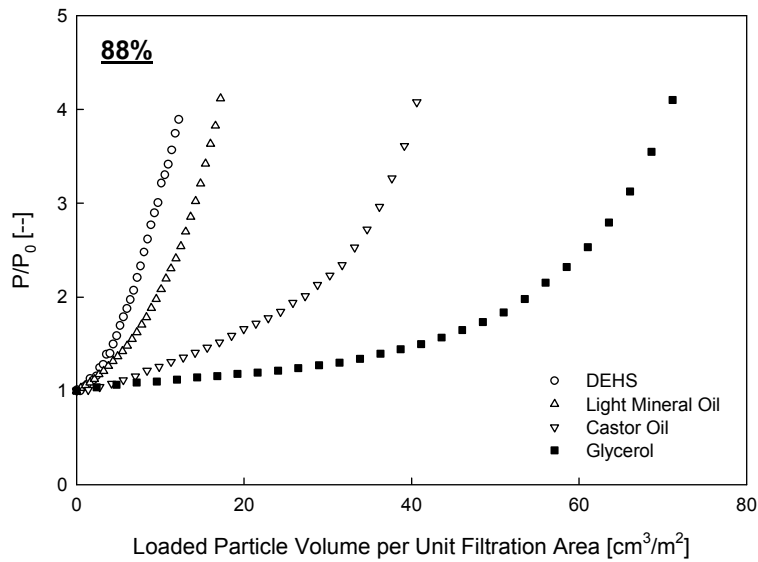
Figure 4.24   Loading curves for the cellulose filter loaded with particles coated with 88% liquid

3.6   *Empirical and Semi-empirical Modeling*

Based on our experimental observations, when the liquid volume percentage is less than 50%, the pressure drops of the glass fiber filter and the cellulose filter are primarily caused by the solid part of the loaded liquid-coated particles. Moreover, the loading curves for the low surface tension liquids can converge into one, regardless of their viscosity, as the total loaded volume is multiplied by the solid volume percentage. As a result, below 50% liquid volume percentage, the existing pressure drop models for solid particle loading can be applied to estimate the loading curves for particles coated with DEHS, light mineral oil, or castor oil. However, most of the models for solid particle loading consider either only the initial loading phase or only the dust cake filtration regime. Bergman's model (1978) [19] can describe the pressure drop evolution from very beginning to the clogged condition, and it is selected for our study. Details of this model were already summarized in Chapter 2 and will not be replicated here.

The general criticism of Bergman's model is on its assumption of uniformly deposited particles in the whole filter. Hence, Thomas et al. (1999, 2001) [9, 10] proposed to divide the whole filter into several layers and evaluate the layers' collection efficiencies and pressure drops repeatedly at every time step, based on the information of the prior layer. Although it is closer to realistic conditions, the calculation is cumbersome and the result can depend on the number of the layers defined artificially. In this study, a similar concept to Thomas et al.'s work is employed, but the filter is divided into only two layers. Since impaction is the major filtration mechanism for our test filters, the front layer is assumed to collect all particles, and the rear layer is assumed to remain as a clean filter. Therefore, the procedure is simplified to calculate the filter pressure drops only and

does not require iterative calculation. The total pressure drop (ΔP) is then the summation of the pressure drops of these two layers.

$$\Delta P = \Delta P_{fL} + \Delta P_{rL} , \tag{4.1}$$

$$\Delta P_{fL} = 64\mu Z_{fL} U \left(\frac{\alpha_f}{d_f} + \frac{\alpha_p}{d_p} \right) \left(\frac{\alpha_f}{d_f^2} + \frac{\alpha_p}{d_p^2} \right)^{0.5} , \text{ and} \tag{4.2}$$

$$\Delta P_{rL} = 64\mu Z_{rL} U \frac{\alpha_f^{1.5}}{d_f^2} , \tag{4.3}$$

where

ΔP_{fL} is the pressure drop of the front layer,

ΔP_{rL} is the pressure drop of the rear layer,

μ is the fluid viscosity,

U is the face velocity,

Z_{fL} is the thickness of the front layer,

Z_{rL} is the thickness of the rear layer,

α_f is the filter packing density,

α_p is the packing density due to deposited particle,

d_f is the filter fiber mean diameter, and

d_p is the particle mean diameter.

The thickness of the front layer (Z_{fL}) is the critical parameter for the model prediction, and it can be estimated from SEM pictures of the loaded filters. The depths of the front layers used for the glass fiber filter and the cellulose filter were 190 μm and 55 μm, respectively. The other filter characteristics required for the model are all listed in

Table 4.2, and α_p can be calculated based on the loaded particle volume. As seen in Fig. 4.26, the curves predicted by the modified Bergman's model are quite close to the experimental results for both the glass fiber filter and the cellulose filter, up to a pressure drop ratio of 4. Therefore, by recalculating the loaded particle volume, the model can be extended to predict the loading behavior for the challenge particle coated with a maximum of 50% liquid by volume.
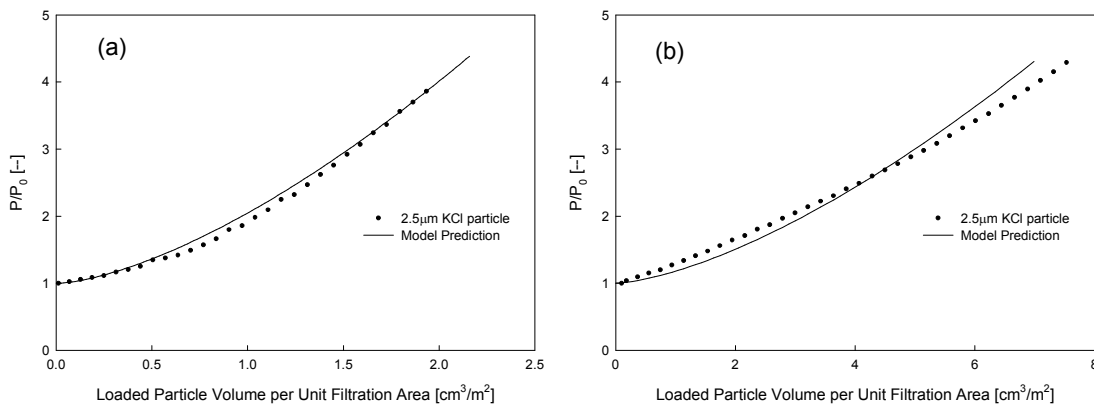
Figure 4.25a Comparison of the experimental data and the model prediction for the glass fiber filter loaded with 2.5 μm solid KCl particles

Figure 4.25b Comparison of the experimental data and the model prediction for the cellulose filter loaded with 2.5 μm solid KCl particles

For liquid volume percentages higher than 50%, the transition behavior is more dynamic and strongly depends on the liquid properties (viscosity and surface tension) as well as the filter media characteristics (absorptive or non-absorptive). No current theoretical or empirical model is able to simulate the behavior. Consequently, a power law type equation including two parameters, the exponent (n) and the critical volume (V_{cr}), is introduced to fit the experimental data. In this equation, the exponent (n) controls the curve growing speed, and the critical volume (V_{cr}) controls the curve horizontal scale.

$$\frac{\Delta P}{\Delta P_0} = 1 + \left(\frac{V}{V_{cr}}\right)^n .$$

(4.4)

A similar approach was earlier employed by Hermans and Bredée (1936) [20] and Gonsalves (1950) [21] in hydrosol filtration, and later applied to aerosol filtration by Emi et al. (1982) [22]. A satisfactory result was reported by Emi et al. for collection efficiency data, but the correlation with the pressure drop was not successful. However, in this study, the loading curves for different liquid-coated particles are found to be well fitted by Eqn. (4.4), at least up to four times the initial pressure drop (Fig. 4.26a. & b.).
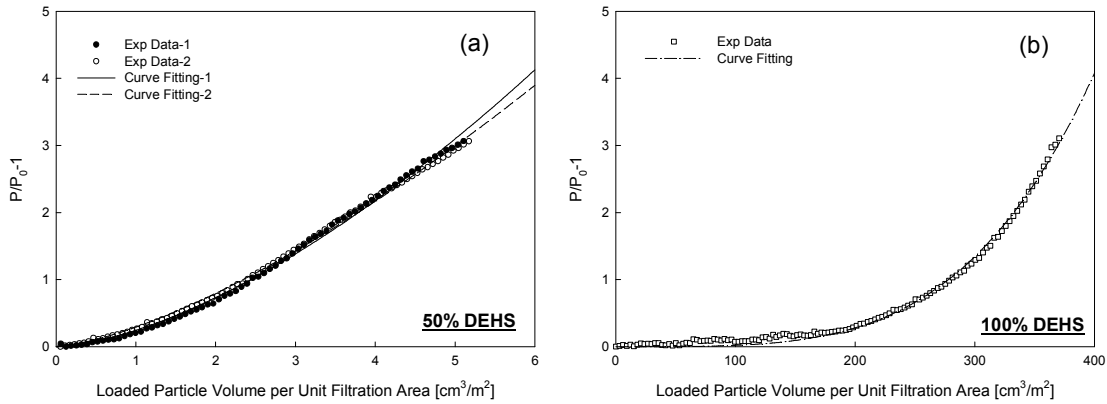
Figure 4.26a Comparison of the experimental data and the fitting results for the glass fiber filter loaded with 2.5 μm 50% DEHS coated particles

Figure 4.26b Comparison of the experimental data and the fitting results for the glass fiber filter loaded with 2.5 μm 100% DEHS particles

In establishing the empirical model, the data of the glycerol case are not included here. Glycerol's surface tension and viscosity are both very different from those of the other coating liquids, and the influences of the surface tension and the viscosity are difficult to qualitatively differentiate based on our current experimental data. Therefore, V_{cr} and n are correlated only with the viscosity of coating liquid in this study.

To better illustrate the fitting results, both V_{cr} and n are plotted versus the diameter fraction of solid core (KCl diameter fraction), instead of the volume percentage of the coating liquid. The KCl diameter fractions corresponding to 0%, 20%, 50%, 88%, and 100% liquid volume percentages are 1.0, 0.93, 0.79, 0.49, and 0. As seen in the figures (Fig. 4.27, 4.28, 4.29, 4.30), when the KCl diameter fraction (X) is larger than 0.79, the values of V_{cr} and n do not change much for coating liquids having similar surface tensions but different viscosities. This again evidenced that within this range of core diameter fractions, the effect of viscosity is not significant, and the behavior can be well modeled as described previously. However, below this critical diameter fraction, V_{cr} and/or n start to diverge, and the trend is correlated with the viscosity of the coating liquid. Therefore, the liquid viscosity begins to influence the loading behavior of liquid-coated particles. For the glass fiber filter, as the KCl diameter fraction further approaches to 0, the V_{cr} for different coating liquids all approach to the same value eventually (Fig. 4.27). It is known that the surface tension effect is dominant over the viscosity effect for pure liquid particle loading on a glass fiber filter. On the other hand, the variations of the power n for different coating liquids are always minor for the glass fiber filter (Fig. 4.28), and their values can be roughly predicted by a 3rd order polynomial equation.

$$n = 1.059 + 1.243X - 1.516X^2 + 0.468X^3, \tag{4.5}$$

where

X is the diameter fraction of solid core.
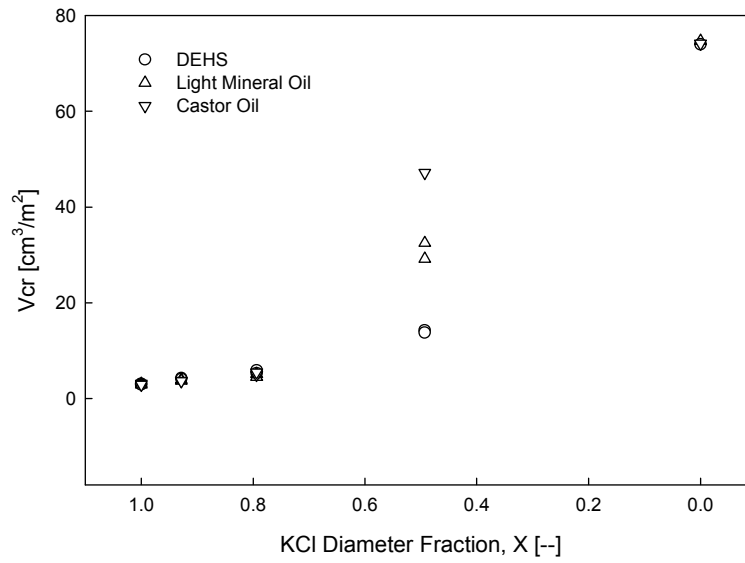
Figure 4.27   Critical volume (V_{cr}) of different coating liquids vs. the core diameter fraction for the glass fiber filter
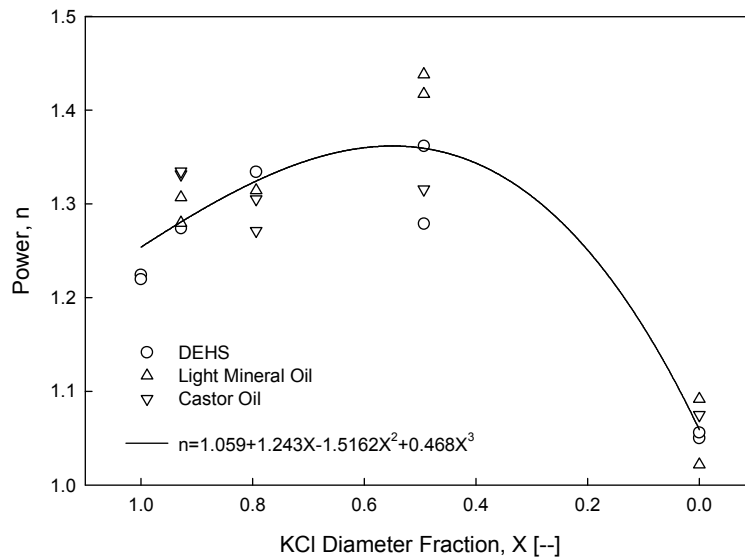
Figure 4.28   Exponent (n) of different coating liquids vs. the core diameter fraction for the glass fiber filter

For the cellulose filter, the behaviors of V_{cr} and n are more complex. The coating liquid not only can flow on the filter fibers but also can be absorbed by the cellulose

fibers. Moreover, the viscosity of the coating liquid reverses the loading curve's relative positions completely within a range of KCl diameter fractions. Compare Fig. 4.6 and 4.24 for example. Therefore, in order to include the viscosity effect in the model, the commercially available software Table Curve 3D is used to correlate V_{cr} and n with liquid viscosity and KCl diameter fraction (X) for the cellulose filter. A similar procedure is also applied to V_{cr} for the glass fiber filter.
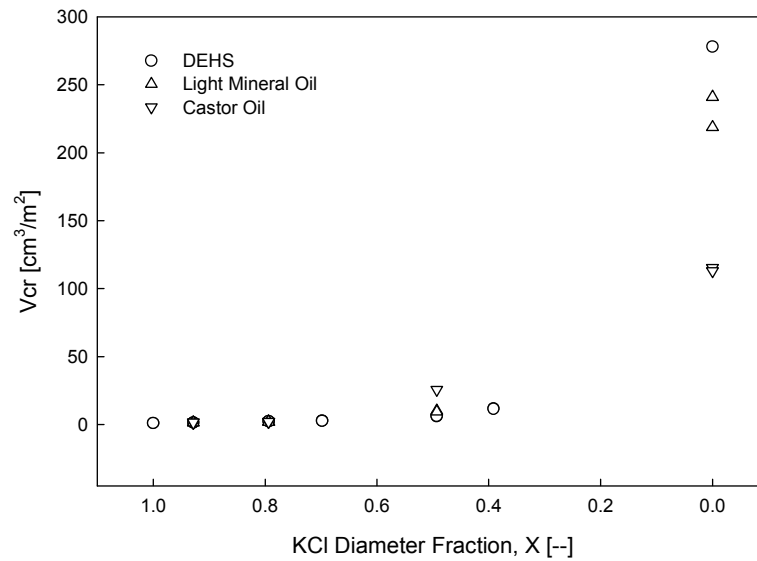
Figure 4.29   Critical volume (V_{cr}) of different coating liquids vs. the core diameter fraction for the cellulose filter
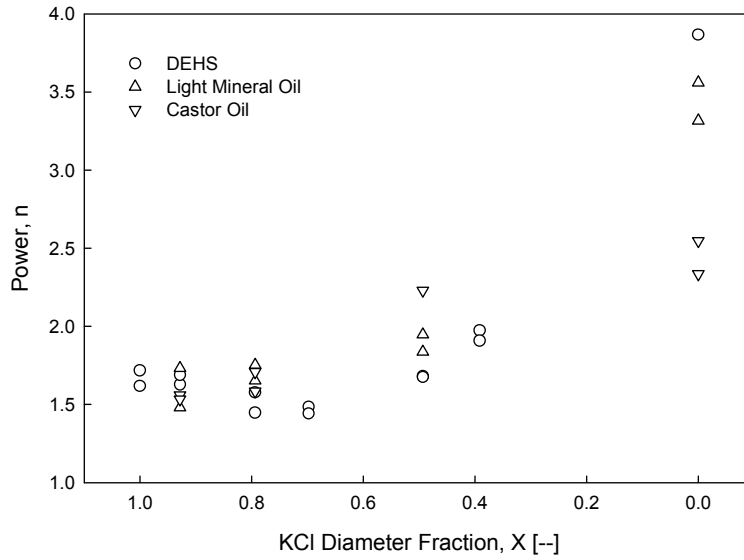
Figure 4.30   Exponent (*n*) of different coating liquids vs. the core diameter fraction for the cellulose filter

Before processing the data, the V_{cr} for different liquids were normalized by the their maximum $V_{cr,liq}$ (the V_{cr} for pure liquid particle loading), and the viscosities of different coating liquids (μ_{liq}) were divided by the viscosity of water (μ_w). As seen in the figures (Fig. 4.31, 4.32, 4.33), all three data sets can be fitted by the same polynomial equation (Eqn. 4.6) but with different constants, which are listed in Table 4.3. In other words, the values of V_{cr} and *n* can now be estimated for the glass fiber filter and the cellulose filter loaded with particles coated with liquids of different viscosities. Therefore, by incorporating the estimated values into Eqn. (4.4), the loading behavior can then be predicted for the liquid-coated particles consisting of more than 50% liquid, i.e., the core diameter fraction less than 0.79.

$$
\frac{V_{cr}}{V_{cr,liq}} = A + B \cdot (X) + C \cdot (X^2) + \frac{D}{\log(\mu_{liq}/\mu_w)^2} + \frac{E \cdot (X)}{\log(\mu_{liq}/\mu_w)} +
$$
$$
F \cdot (X^3) + \frac{G}{\log(\mu_{liq}/\mu_w)^3} + \frac{H \cdot (X^2)}{\log(\mu_{liq}/\mu_w)} \quad \text{for } 0.79 > X > 0,
$$

(4.6)

where *A, B, C, D, E, F, G,* and *H* are fitting constants, and *X* is the core diameter

fraction.

Table 4.3   Fitting constants in Eqn. 4.6 for different V_{cr} and *n*

V_{cr} / Glass Fiber Filter, r^2=0.9950

	Values	Std Error	T Value	95.00% Conf Lim	
A	1.000	0.015	68.590	0.967	1.033
B	0.835	0.161	5.178	0.470	1.199
E	-6.213	0.446	-13.932	-7.222	-5.204
F	-3.194	0.273	-11.719	-3.811	-2.578
H	7.841	0.600	13.066	6.484	9.199

V_{cr} / Cellulose Filter, r^2=0.9957

	Values	Std Error	T Value	95.00% Conf Lim	
A	0.977	0.012	82.161	0.952	1.003
B	-2.866	0.531	-5.397	-4.005	-1.727
C	5.169	1.463	3.532	2.030	8.307
E	-2.640	0.435	-6.075	-3.572	-1.708
F	-3.865	1.042	-3.708	-6.101	-1.629
H	3.284	0.597	5.500	2.004	4.565

n / Cellulose Filter, r^2=0.9846

	Values	Std Error	T Value	95.00% Conf Lim	
A	1.712	0.120	14.264	1.453	1.971
B	6.219	0.958	6.489	4.149	8.289
C	-7.052	1.189	-5.930	-9.621	-4.483
D	9.694	1.273	7.615	6.944	12.444
E	-18.726	1.635	-11.452	-22.259	-15.193
G	-7.576	1.556	-4.869	-10.937	-4.215
H	17.202	1.989	8.647	12.904	21.500
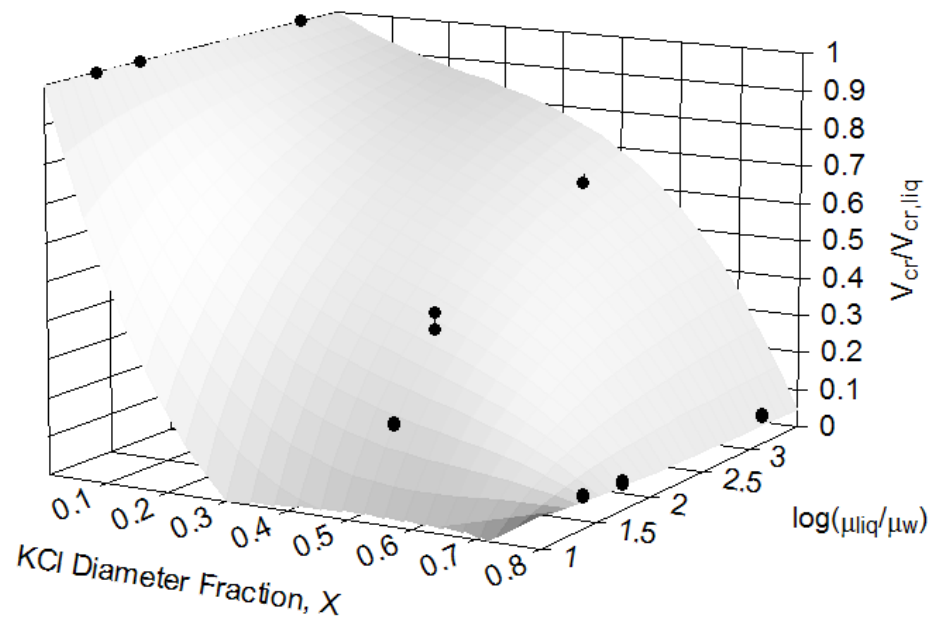
Figure 4.31   Fitting result for V_{cr} in the case of the glass fiber filter
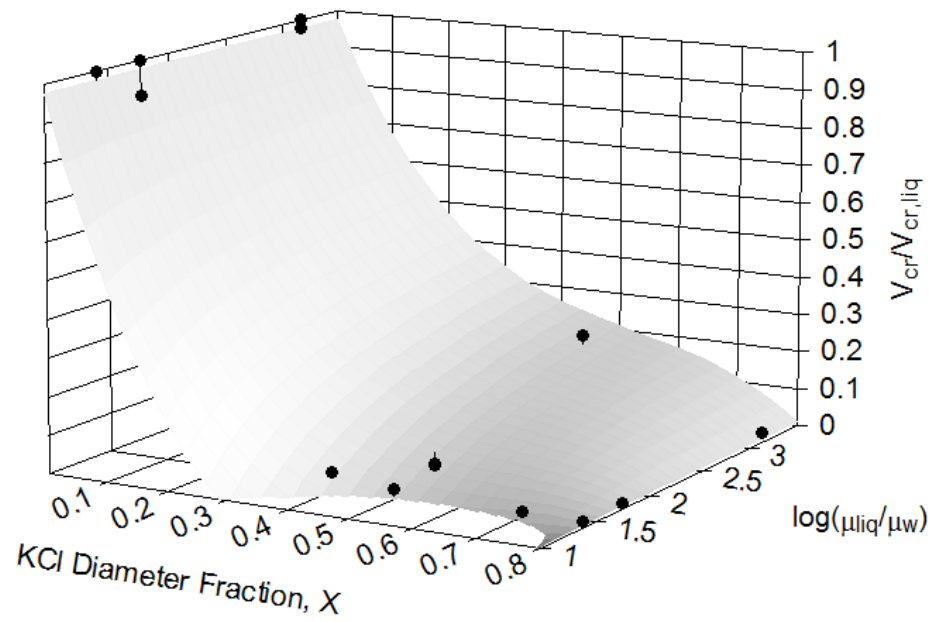
Figure 4.32   Fitting result for V_{cr} in the case of the cellulose filter
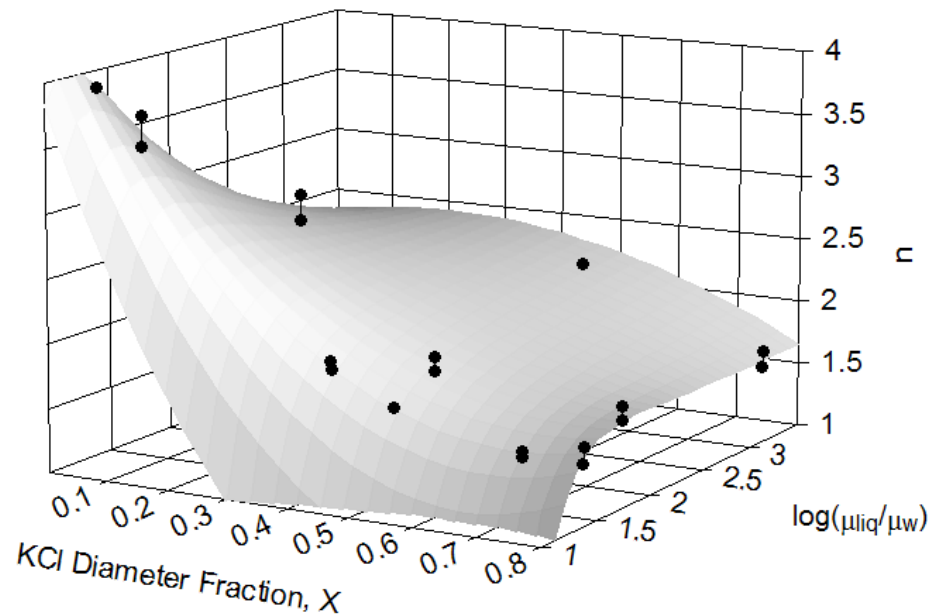
Figure 4.33   Fitting result for *n* in the case of the cellulose filter

4. Summary

Through examining the morphologies of loaded liquid-coated particles under SEM, the general transition behavior of loading curves can be correlated with the microscopic observations. As the amount of the liquid in the liquid-coated particle increases, the structure of the deposited particles changes from long dendrites to short dendrites and then to mixed clumps. Therefore, the loading curves shift from the very left, the solid particle loading case, to the very right, the liquid particle loading case. However, the detailed changes of the morphologies and the behavior are complex, since different forces, such as air drag, capillary force, viscous force, and frictional force, are interacting, and their relative importances are highly depending on the operating conditions. In general, it is believed that at low liquid volume percentages the capillary force is important through the formation of liquid bridges. When the particle is coated with more

liquid, viscous force and frictional force become dominant over capillary force because microscopic "debris flow" can occur on the filter fibers. Later, for pure liquid particle/droplet loading, the surface tension of the liquid is critical, since it determines the shape of coalesced loaded droplets. For cellulose filters, the scenario is even more complex due to the additional mechanism of absorption by cellulose fibers. Therefore, several series of liquid-coated particle loading testes, from pure solid particle loading to pure liquid particle loading, were performed under different operation conditions to study the effect of the filter material, the coating liquid properties, the particle size, and the face velocity. The major findings and conclusions obtained are as follows:

☐ Based on the experimental observation, the liquid volume percentage of 50% seems a critical value for liquid-coated particle loading behavior.

☐ When the liquid volume percentage is less than 50%, the loading curves for the coating liquids of low surface tension, DEHS, light mineral oil, and castor oil, overlap for both the glass fiber filter and the cellulose filter.

☐ Their loading curves at different liquid volume percentages can converge into one as the total loaded particle volume is replaced by the solid particle volume. This convergence directly evidences that the pressure drop is mainly caused by the solid core of liquid-coated particles.

☐ The curve of glycerol, the coating liquid with highest surface tension, is located at the right of the others for both the glass fiber filter and the cellulose filter. This may be because the dendrite is strengthened through the formation of liquid bridges between the particles and the structure becomes more porous.

□ When the liquid-coated particle consists of more than 50% liquid, the effect of the liquid viscosity becomes important. The loading curves for different coating liquids are spread out in the order of their viscosity, for both the glass fiber filter and the cellulose filter.

□ For pure liquid particle loading, the behaviors are different for the cellulose and the glass fiber filter. It is believed that the absorption of liquid by cellulose could be the reason.

□ The size effect on the loading behavior can be diminished by converting the loaded particle volume to the loaded particle surface area for liquid volume percentages less than 50%.

□ Face velocity seems to be insignificant for liquid-coated particles loaded on the cellulose filter in the range from 5 to 20 cm/s, but the face velocity effect is expected for the glass fiber filter.

An empirical model is established to simulate the loading behavior for filters loaded with particles coated with different thickness of liquid films. The model consists of two parts in response to our experimental observations of distinct loading behaviors above and below the coating liquid percentage of 50%. For liquid volume percentages less than 50%, the Bergman's model for solid particle loading is modified to predict the pressure drop evolution up to four times the initial pressure drop. In this part of the model, the loaded filter is considered as a combination of two layers. One collects all challenge particles, and the other remains as a clean filter during the loading process. The thickness of the layer can be estimated by the SEM picture, and the total pressure drop is the

summation of those in these two layers. For coating liquid percentages larger than 50%, a power type equation with two parameters, the exponent (n) and the critical volume (V_{cr}), is introduced to empirically fit the experimental data. The correlations among these two parameters and the core diameter fraction (X) and the viscosity of coating liquid are established for the glass fiber filter and the cellulose filter. Therefore, the overall transition behavior for liquid-coated particle loading can be estimated in advance for coating liquids of different viscosities. However, the current model is limited to the coating liquids of low surface tension (< 35 mN/m), since the effect of the liquid surface tension is not included. The accuracy of the prediction will be improved if more data points are available for empirical fitting.

5. References

[1]   Contal, P. et al. (2004) Clogging of fibre filters by submicron droplets. Phenomena and influence of operating conditions. *J. Aerosol Sci.,* 35: 263-278.

[2]   Agranovski, I. E., and Braddock, R. D. (1998) Filtration of liquid aerosols on wettable fibrous filters. *AIChE J.*, 44:2775-2783.

[3]   Briscoe, B. J., Galvin, K. P., Luckham, P. F., and Saeid, A. M. (1991) Droplet coalescence on fibers. *Colloids and Surfaces,* 156:301-312.

[4]   Espert, A., Vilaplana, F., and Karlsson, S. (2004) Comparison of water absorption in natural cellulosic fibers from wood and one-year crops in polypropylene composites and its influence on their mechanical properties. *Composites: Part A* 35: 1267–1276.

[5]   Iveson, S. M., Lister, J. D., Hapgood, K., and Ennis, B. J. (2001) Nucleation, growth and breakage phenomena in agitated wet granulation processes: a review. *Powder Tech.*, 117:3-39.

[6]   Holm, P., Schafer, T., and Kristensen, H. G. (1985) Granualation in high-speed mixers: Part V. Power consumption and temperature changes during granulation. *Powder Tech.*, 43:213-223.

[7]   Servais, C., Jones, R., and Roberts, I. (2002) The influence of particle size distribution on the processing of food. *J. of Food Engineering*, 51:201-208.

[8]   Takagaki, Sol Sho (2006). Transitional particle loading of air filters, Ph.D. thesis, University of Minnesota, Minneapolis, MN.

[9]   Thomas, D., Contal, P., Renaudin, V., Penicot, P., Leclerc, D., and Vendel, J. (1999) Modeling pressure drop in HEPA filters during dynamic filtration. *J. Aerosol Sci.,* 30:235-246.

[10]   Thomas, D., Penicot, P., Contal, P., Leclerc, D., and Vendel, J. (2001) Clogging of fibrous filter by solid aerosol particles: experimental and modeling study. *Chemical Engineering Science*, 56:3549-3561.

[11]   Penicot, P., Thomas, D., Contal, P., Leclerc, D., and Vendel, J , (1999) Clogging of HEPA fibrous filters by solid and liquid aerosol particles: An experimental study. *Filtration and Separation(March)* 59-64.

[12]   Letourneau, P., Renaudin, V., and Vendel, J. (1991) Aerosol penetration inside HEPA filtration media. *21st DOE/NRC Nuclear Air Cleaning Conference* 799-812.

[13]   Letourneau, P., Renaudin, V., and Vendel, J. (1993) Effects of the particle penetration inside filter medium on the HEPA filter pressure drop. *22nd DOE/NRC Nuclear Air Cleaning Conference* 128-143.

[14]   Walsh, D. C. (1996) Recent advances in understanding of fibrous filter behavior under solid particle loading. *Filtration and Separation (June)* 501-506.

[15]   Lee, J. K., Kim, S. C., and Liu, B. Y. H. (2001) Effect of bi-modal aerosol mass loading on the pressure drop for gas cleaning industrial filters. *Aerosol Sci. Technol.* 35: 805-814.

[16]   Chen, C. C., Chen, W. Y., Huang, S. H., Lin, W. Y., Kuo, Y. M., and Jeng, F. T. (2001) Experimental study on the loading characteristics of needlefelt filters with micrometer-sized monodisperse aerosols. *Aerosol Sci. Technol.* 34: 262-273.

[17]   Charvet, A., Gonthier, Y., and Gonze, Y. (2008) Filtration of liquid aerosols with a horizontal fibrous filter. *Chemical Engineering Research and Design*, 86:569-576.

[18]   Farris, R. J. (1968) Prediction of the viscosity of multimodal suspensions from unimodal viscosity data. *Transactions of the Society of Rheology*, 12: 281-301.

[19]   Bergman, W. et al. (1978) Enhanced filtration program at LLNL. 15th DOE/NRC nuclear air cleaning conference, Boston.

[20]   Hermans, P. H., and Bredée, H. L. (1936) *J. Soc. Chem. Ind.*, 55T:1.

[21]   Gonsalves, V. E. (1950) *Rec. trav. Chim.*, 69: 873.

[22]   Emi, H., Wang, C. S., and Tien, C. (1982) Transient behavior of aerosol filtration in model filters. *J. AIChE,* 28:397-405.

Chapter 5

Effect of Geometric Configuration on the Collection Efficiency

for Axial Flow Cyclones

1. Introduction

Two types of cyclones have been explored in the literature: tangential flow and axial flow cyclones. The primary difference is the relative directions of the entering and exiting aerosol flows. In tangential flow cyclones, the aerosol stream enters perpendicular to the device's axis and exits upward in parallel to the axis. In axial flow cyclones, the stream both enters and exits parallel to the device's axis, entering at the top and existing from the bottom. The flow arrangement of the axial flow cyclone allows it to easily connect inline with other devices. Cyclones also differ in the location of their vortex finder (V.F.). Tangential flow cyclones typically place the V.F. at the top of the cyclone body, while axial flow cyclones locate it at the cyclone base. The intrinsic configuration differences between the two cyclone types result in different flow fields. The effect of other configuration features, such as the geometry of the cyclone base, is expected to differ between tangential and axial flow cyclones. In this chapter we focused on the variation of particle collection efficiency of axial flow cyclones resulting from various internal geometric configurations of the devices.

Tangential flow cyclones have been extensively studied both experimentally and theoretically, but particle motion in cyclones has not been completely characterized. It is because of the complex 3-D vortex turbulence flows and unclear particle-turbulence interaction involved in cyclones. Therefore, semi-empirical models were developed for the design of cyclones [1-6]. The effects of different geometric dimensions and configurations on the collection efficiency of tangential flow cyclones have been investigated. Kim and Lee (1990) [7] studied the effects of the radial dimensions of tangential flow cyclones, including the sizes of cyclone body and the vortex finder (V. F.).

Kim and Lee (1990) [7] found that a decrease of the V.F. diameter enhances the particle collection efficiency. A similar result was also observed by Moore and McFarland (1993) [4], Saltzman and Hochstrasser (1983) [3], and Lidén and Gudmundssen (1997) [5]. The effect of the cyclone body size on the particle collection efficiency is ambiguous, depending on the relative scale to the V.F. size. Moreover, Kenny and Gussman (2000) [8] point out the inconsistent trend of two experimental data sets [5, 9] for the relation between the collection efficiency curve sharpness and the V.F. size. Kenny and Gussman (2000) [8] posited that geometric factors other than the cyclone body size could play an important role in cyclone performance. They further concluded that the cyclone performance of short or small-coned cyclones tends to be controlled by the outlet and inlet designs, while the performance of long or wide-coned cyclones tends to be dominated by the cone and base designs

Zhu and Lee (1999) [10] examined the effect of cyclone longitudinal sizes, cyclone body height, and V.F. length on the particle collection efficiency. It is then concluded that the difference between body height and V.F. length is critical in determining the efficiency. Xiang, Park, and Lee (2001) [11] explored the effect of the cone dimension on particle collection efficiency by testing cyclones with various cone base diameters. The work found that the cyclone collection efficiency increases significantly as cone base diameter is reduced. To further improve cyclone performance, Zhu et al. (2001) [12] proposed a special design of a tangential flow cyclone with an upside-down cup in the body. Lim, Kim and Lee (2004) [13] examined the effect of the V.F. shape on the characteristics of particle collection efficiency. All of these geometric modifications are valuable in optimizing the cyclone performance. However, note that all

the above works focused on tangential flow cyclones for collecting super-micrometer particles.

Very limited experimental data and predictive models have been published for axial flow cyclones. Wedding et al. (1982) [14] proposed a dichotomous sampling head using an axial flow separator design to match the human thoracic penetration curve. Vaughan (1988) [15] developed a simple axial flow cyclone consisting of a helical channel, a cylindrical body, and an aerosol exit tube. Six configurations with three cyclone body lengths and two channel depths were tested under cyclone flow rates ranging from 1.1 to 4.16 lpm. The results show the particle collection efficiency increases with cyclone height up to a certain value and then decreases with further increases in cyclone height. Vaughan also concluded that this axial flow cyclone can separate small particles and may result in high pressure drop, compared to a tangential flow cyclone of comparable size. Work done by Tsai et al. (2004) [16] focused on the axial flow cyclone performance under low pressure. They found the cutoff particle size decreases with decreasing pressure in cyclone body. Under an absolute pressure of 6 torr in the cyclone body, the cutoff size of the cyclone tested was reduced to 43.3 nm aerodynamic particle size [16]. None of these studies systematically investigated the effect of axial flow cyclone configurations on particle collection efficiency. In this chapter we focused on the effects of cyclone configurations. i.e., the V.F. length, optional upside-down cup, and base shape, on the collection efficiency curve. The experimental observations reported herein advance the design knowledge of axial flow cyclones. The study also presents a simple model to evaluate both the particle loss in the spindle vane section of an axial flow

cyclone and the particle collection in the axial cyclone. The report also assists researchers in designing an axial flow cyclone with good performance.

2. Design of Axial Flow Cyclone
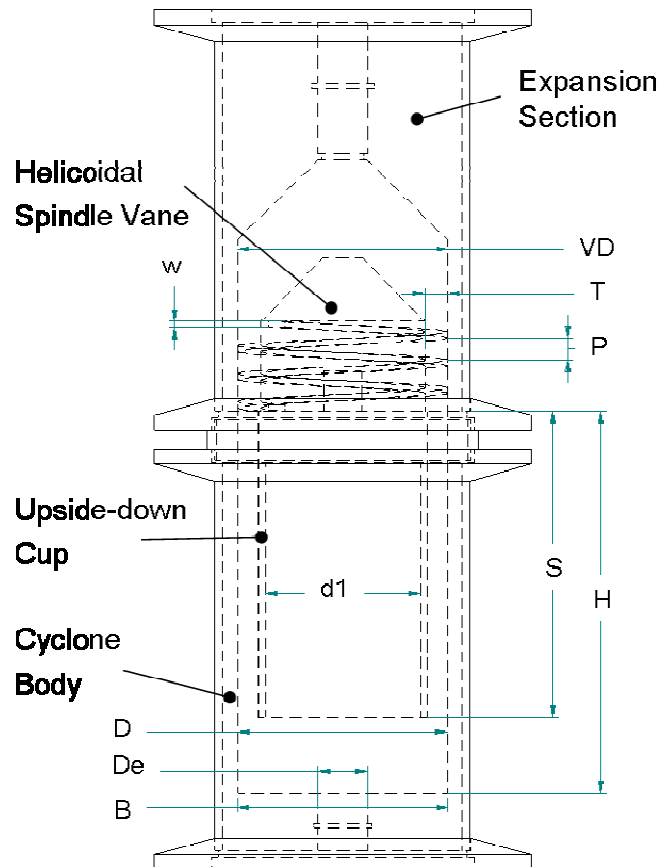
Figure 5.1   Schematic diagram of axial flow cyclones tested

Table 5.1   Geometrical dimensions for tested axial flow cyclones

Vane Dia. (VD)	[cm]	2.898	VD/D	=	1
Pitch (P)	[cm]	0.358	P/D	=	0.123
Channel Depth (T)	[cm]	0.378	T/D	=	0.13
Body Dia. (D)	[cm]	2.898	D/D	=	1
Outlet Dia. (De)	[cm]	0.635	De/D	=	0.219
Body Length (H)	[cm]	5.842	H/D	=	2.015
Base Dia. (B)	[cm]	2.898/0.953	B/D	=	1.0/0.328
Cup Length (S)	[cm]	4.572	S/D	=	1.577
Cup Dia. (d1)	[cm]	2.144	d1/D	=	0.739
Insertion Length (l)	[cm]	3.810/0	l/D	=	1.314/0

Similar to the device designed by Tsai et al. (2004) [16], the axial flow cyclone shown in Fig. 5.1 consists of an expansion section, a helicoidally spindle vane, an optional upside-down cup, a cyclone body with either a conical or abrupt contraction base, and a vortex finder tube (as the aerosol outlet tube). Tsai et al. (2004) [16] found that a spindle vane with one helix flow channel making complete three turns has higher collection efficiency than one with three half-turn helicoidal channels. Accordingly, a spindle vane with one three-full-turn channel was employed in our test cyclone. The pitch and channel width of the helicoidally spindle vane were 0.141 and 0.149 inch, respectively. The vane section was used to guide the axially entering aerosol stream into the cyclone body and to generate swirling flow in the body for particle separation. An optional upside-down cup having the same diameter as the vane inner diameter could be installed under the vane section. The cup idea was first proposed and tested by Zhu et al. (2001) [12] for tangential flow cyclones. For tangential flow cyclones, higher particle

collection efficiency and sharper separation curves were found with the cup when compared to the widely used high-efficiency Stairmand cyclone [12]. None of existing axial flow cyclones included the cup feature. We built the optional cup feature in our axial flow cyclone specifically to test its effect on the cyclone particle collection efficiency. Two cone bases were designed for our cyclone, with the total body length fixed at 2.3 in. One base had a 45° conical contraction, and the other had an abrupt contraction. A vortex finder (V.F.) with a diameter of 0.25" was inserted into the cyclone body from the cyclone base. Vortex finder tubes of two different insertion lengths, i.e., 0 and 1.5", were chosen to investigate their effect on the particle penetration curve. The exact dimensions of each test component of the axial flow cyclone are listed in Table 5.1.

3. Experimental Setup
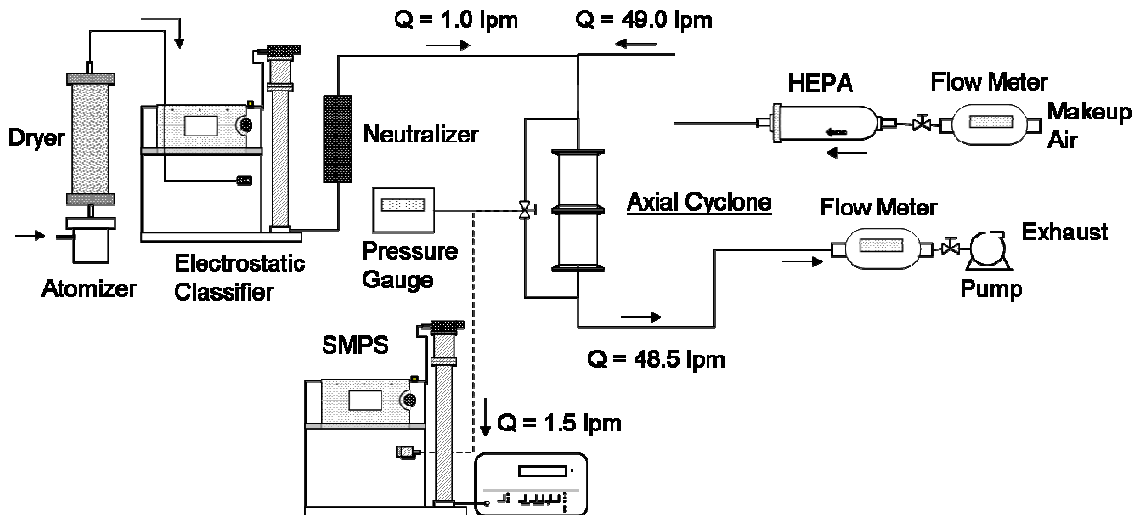
Figure 5.2   Schematic diagram of experimental setup to evaluate the particle
                    collection efficiency of axial flow cyclones

A schematic diagram of the experimental setup used in this study is shown in Fig. 5.2. A homemade collision atomizer was applied to atomize aqueous solutions of

potassium chloride (KCl). Polydisperse KCl particles were produced by passing atomized droplets through a desiccant diffusion dryer to remove the solvent in droplets and through a Kr^{85} bipolar neutralizer to minimize the electrical charges on particles. The resulting polydisperse particles were then introduced to the electrostatic classifier (TSI model 3081) to provide challenge particles in a narrow size range. Because the aerosol flowrate generated by the atomizer was much less than the operational flowrate of the tested axial flow cyclone, additional clean air flow, after passing through a HEPA filter, was added to the aerosol stream. A scanning mobility particle sizer (SMPS, TSI model 3936) was used to measure the particle size distributions in the upstream and downstream of the cyclone. The particle penetration of each size was then calculated by taking the ratio of the particle concentrations measured downstream and upstream of the cyclone. Note that the use of a Kr^{85} bipolar charger prior to the particle classifier typically results in multiple particle peaks in SMPS measurements, because of the multiple charge status of polydisperse particles after passing through a bipolar charger. Particle peaks with multiple charges can be minimized by classifying particles with a size larger than the mean size of generated polydisperse particles. In the particle penetration measurements, we used only the particle concentration in the singly charged particle peak measured by SMPS. Since cyclones separate particles based on aerodynamics, the electrical mobility size (d_e) classified by SMPS was converted to the aerodynamic particle size (d_a) based on the formula given by Hinds (1998) [17]:

$$d_a = d_e \left(\frac{C_c(d_e)}{C_c(d_a)} \right)^{0.5} \left(\frac{\rho_p}{\rho_0} \right)^{0.5} , \qquad\qquad (5.1)$$

where $C_c(d_e)$ and $C_c(d_a)$ are the respective Cunningham slip coefficients for the electrical mobility size (d_e) and the aerodynamic particle size (d_a), and the particle density (ρ_p) of potassium chloride particles is given as 1987 kg/m^3.

Axial cyclones of eight different cyclone configurations, including cases with and without the cup, two base shapes, and two V.F. insertion tube lengths, were tested under identical flow conditions. The operational flow rate of the axial cyclones was fixed at 50 lpm, which was controlled and monitored by a needle valve and a mass flow meter (TSI 4043) located downstream of the cyclones. The pressure drop across the cyclones was recorded by a MKS Baratron type pressure gauge (626A13TAE, 1000 torr max) during the tests.

4 Results and Discussion

Table 5.2   Cutoff sizes and pressure drops of axial flow cyclones with various configurations

Cyclone no.*	Base Geometry	Upside-Down Cup	V.F. Length [in]	d50 [µm]	ΔP [torr]
Con-W-0	Conical	with	0	395.3	134.9
Con-WO-0	Conical	without	0	306.6	182.7
Con-W-1.5	Conical	with	1.5	447.9	125.8
Con-WO-1.5	Conical	without	1.5	356.1	148.5
Rec-W-0	Abrupt	with	0	388.7	135.4
Rec-WO-0	Abrupt	without	0	305.4	187.4
Rec-W-1.5	Abrupt	with	1.5	416.7	135.6
Rec-WO-1.5	Abrupt	without	1.5	272.7	182.6

*The first part of the cyclone no. represents the base geometry, and the second and the last parts indicate whether with or without the upside-down cup and the length of the vortex finder. For example Rec-WO-1.5 is the cyclone equipped with an abrupt base and without the upside-down cup, and the V.F. length is 1.5 inch.

4.1 Effect of upside-down cup

Zhu et al. (2001) [12] first introduced the upside-down cup in their double tangential flow cyclone. It was believed that a supplementary vortex could be created with the cup in addition to the pre-existing outer and inner vortexes. The increased collection efficiency for smaller particles, when compared with that of a high-efficiency Stairmand cyclone, was explained by the strengthened centrifugal force due to the additional vortex and longer particle residence time. However, the comparison performed by Zhu et al. (2001) [12] is not exact since the geometric dimensions of the cyclones compared in their study are not identical. The cup effect on the particle collection efficiency for tangential flow cyclones remains to be clarified in the future.
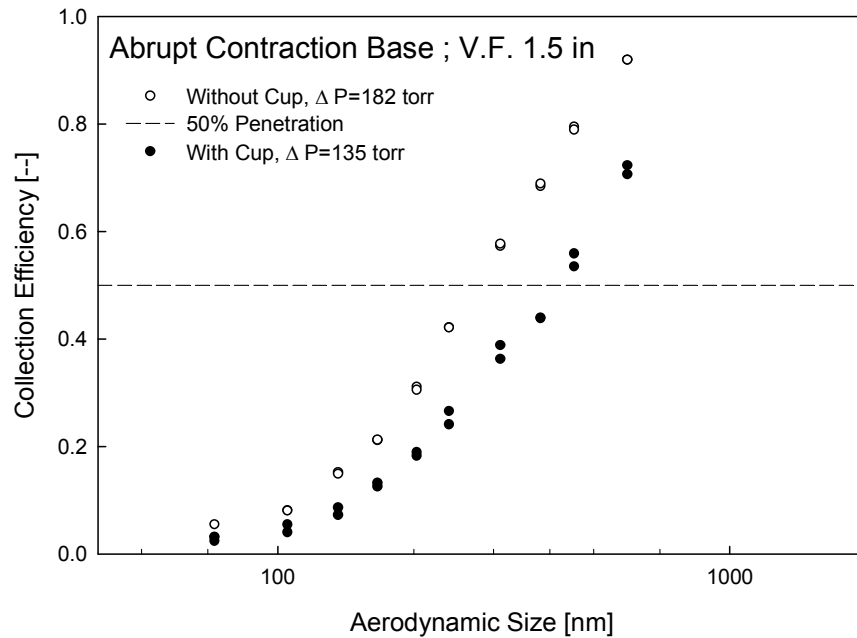
Figure 5.3   Comparison of the collection efficiency of axial flow cyclones without and with the upside-down cup (Rec-WO-1.5 v.s. Rec-W-1.5)

To investigate the effect of the upside-down cup on particle collection by axial cyclones, the same cyclone was tested with and without the upside-down cup. The particle collection efficiencies of axial flow cyclones with and without upside-down cup are shown in Fig. 5.3. With the cup, the particle collection efficiency was shifted to the large particle size range. The cutoff sizes, defined as the particle size with 50% collection efficiency, for the axial flow cyclone with the cup was larger than that for the case without the cup, regardless of the base shape and V.F. tube length (Table 5.2). Moreover, the pressure drop of the axial cyclone without the cup was higher than that with the cup. This observation differs from the result reported by Zhu et al. (2001) [12]. The reason for the larger cutoff particle size for the axial flow cyclone with the upside-down cup may be due to the additional cup wall contributing more flow resistance. The vortexes in the cyclone body thus were weakened by the flow resistance rather than strengthened.

In flow pattern visualization experiments performed by Vaughan (1988) [15], it was shown that the general flow pattern in an axial flow cyclone has three concentric vortexes. The flow following the outer vortex spirals down, forms a inner vortex that spirals upward, and then finally spirals downward again at a even smaller vortex size to the V.F. tube. In other words, without the upside-down cup, the axial cyclone already has a existing vortex resulting from the V.F. tube installed through the cyclone body base. Thus, in our experiments the addition of the upside-down cup to an axial flow cyclone did not provide more particle collection power. Instead, an upside-down cup detrimentally altered the original flow pattern of an axial flow cyclone. We can conclude that an upside-down cup is not recommended in the design of axial flow cyclones.

4.2 Effect of vortex finder length

In a tangential flow cyclone, the dimensions of the V.F. tube are closely related to the cyclone performance as it is critical in defining the cyclone flow characteristics in the cyclone body. Most researches focused on the diameter of the V. F. tubes. The studies have found that the cutoff particle size of a tangential flow cyclone is reduced with a decrease in the V.F. diameter. Moore and McFarland (1993) [4] explain that in a tangential flow cyclone a smaller diameter of the V.F. forces the inner vortex to stretch longer and to increase the fluid velocities of both inner and outer vortexes. As a result, increased particle collection at small particle cutoff sizes is achieved with a smaller V.F. tube diameter. In a study of the V.F. length, Zhu and Lee (1999) [10] conducted a series of experiments for small cyclones with various V.F. insertion tube lengths under flowrates from 60 to 110 lpm. The work suggested the difference between the cylinder height (h) and the V.F. length (S) is the critical parameter, instead of the V.F. length alone, but the experimental correlation between the cutoff size and the parameter (h-S) is not monotonic. The particle cutoff sizes of tangential flow cyclones decrease with an increase of the (h-S) parameter in the small value range, and then increase in the large (h-S) parameter value range. The numerical simulation study of Qian and Zhang (2005) [18] further showed that, for a tangential flow cyclone, natural vortex length is influenced by the same parameter with the same trend, which somewhat explains the effect of the V.F. length observed by Zhu and Lee (1999) [10]. However, the effect of the V.F. length on the natural vortex length and the cyclone performance can be different for axial flow cyclones, owing to the different direction of the exiting aerosol flow. To explore the

effect of the V.F. length on collection efficiency, in this study we tested axial flow cyclones with two V.F. lengths, i.e., 0 and 1.5 in.

As shown in Table 5.2, with the upside-down cup, increasing the V.F. length increases the cutoff size. Although the increase of the V.F. tube length could increase the particle residence time in an axial flow cyclone, the resistance for the flow was also amplified by the presence of the V. F. tube. Apparently the flow resistance effect on particle collection efficiency overshadows the effect of residence time in our study. For the cases without an upside-down cup the results are opposite for the cyclones with rectangular and conical contraction bases. When the V.F. length increases from 0" to 1.5" the collection curve slightly shifted to the small size range for simple cylindrical cyclone body (shown in Fig. 5.4). In contrast, it moved to the large size range for an axial cyclone with conical contraction base (shown in Table 5.2). The above observation can be explained by two possible flow scenarios occurring in the cases of inserting the V.F. tube close to the vane section. For the axial cyclones with a conical contraction base, part of the aerosol flow could be shortcut and directed out by the V.F. tube. For the simple cylindrical cyclone body, the outer vortex may swirl towards the cyclone base and then return up to the vortex finder entrance. As a result, the effective particle residence time would be longer. Consequently the long particle residence time reduces the cutoff particle size of an axial flow cyclone with a simple cylindrical body.
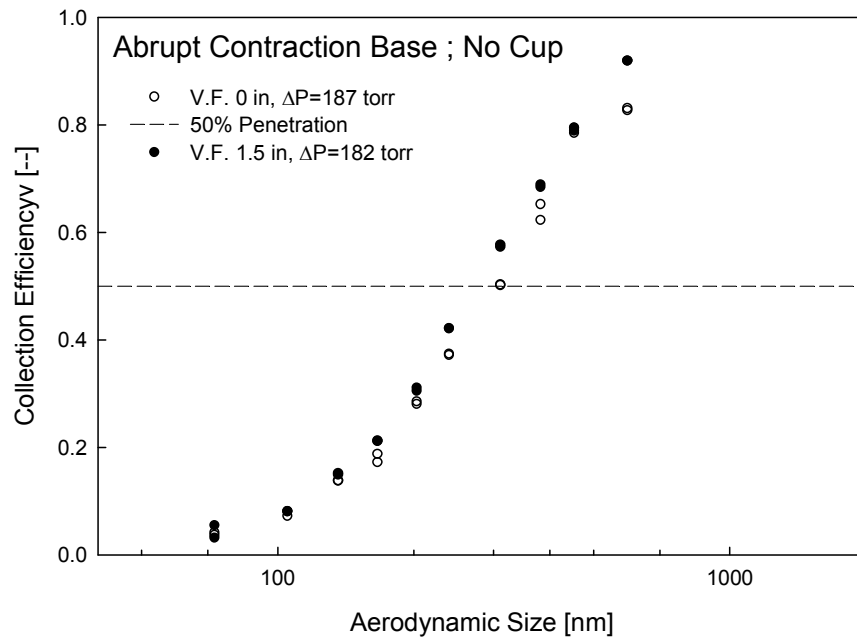
Figure 5.4   Comparison of the collection efficiency of axial flow cyclones with different V.F. lengths (Rec-WO-0 v.s. Rec-WO-1.5)

In conclusion, a longer V.F. could either enhance the particle residence time or raise the chance of creating bypass aerosol flow, depending on other geometric dimensions, such as the cyclone base shape and the diameter of the V.F. tube. Further, similar to Zhu and Lee's analysis, the distance between the outlet and the bottom of vane section is expected be critical for axial flow cyclone performance. More tests will be needed to confirm the above hypothesis.

4.3 Effect of base geometry

The conical contraction base is typically used in tangential cyclones. Kenny and Gussman (2000) [8] concluded that the collection efficiency curves are generally steeper for long or wide-coned cyclones than for short or small-coned cyclones. The experimental results reported by Xiang, Park, and Lee. (2001) [11] demonstrate that the

particle cutoff size increases with a decrease of conical base diameter. Different from tangential designs, most axial flow cyclones utilize a simple cylinder as the cyclone body, with the exception of the multi-stage axial cyclone developed by Liu and Rubow (1984) [19]. No comparison study of the effect of cyclone base geometry on the particle collection efficiency has been reported in the literature.

As shown in Table 5.2, contradictory to the experimental result reported by Xiang, Park, and Lee (2001) [11] for tangential flow cyclones, the cutoff sizes for axial flow cyclones with a conical contraction base cone are always larger than those with an abrupt contraction base. The difference between tangential and axial flow cyclones may be due to the opposed outlet locations of the aerosol flow. The outlet for a tangential flow cyclone is located at the cyclone top. The conical contraction base design in tangential flow cyclones accelerates aerosol flow moving upward. On the other hand, the V.F. is inserted through the base of axial flow cyclones. The conical contraction base may speed up aerosol flow going towards the outlet and consequently increase the particle cutoff size. Therefore, a conical contraction base in an axial flow cyclone will not improve the cyclone performance.

Further, the above observation is strongly correlated with the V.F. insertion length. For cyclones without the upside-down cup, the difference in the collection curves between the cases of conical and abrupt contraction bases is minor with a minimum V.F. tube length. The cutoff sizes in the above cases were 306.6 and 305.4 nm. However, as shown in Fig. 5.5, the cutoff particle size of axial flow cyclones with a conical contraction base increased when the V.F. length was 1.5". As discussed in the previous section, the bypass flow scenario could exist for the cases of long V.F. insertion length

and conical contraction base. It is suspected that the conical contraction base restricts the downward vortex motion and leads to more bypass flow when the V.F. is close to the vane section, while the abrupt contraction base allows the vortex to descend closer to the base. Therefore, for the same cyclone body length, axial flow cyclones with an abrupt contraction base and long V.F. length should offer the best particle collection efficiency among all eight different cyclone configurations tested.
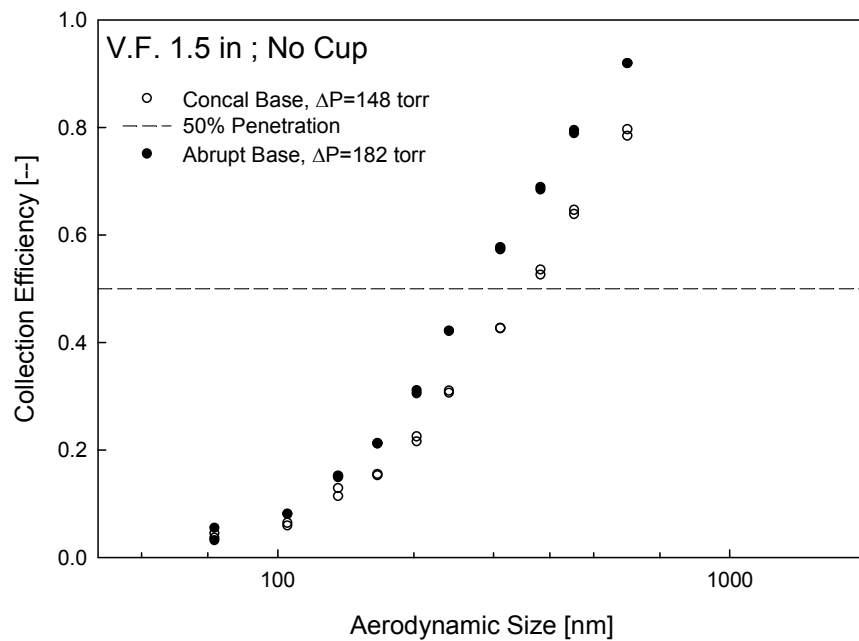
Figure 5.5   Comparison of the collection efficiency of the axial cyclone with conical and abrupt contraction bases. (Con-WO-1.5 v.s. Rec-WO-1.5)

5. Model for Particle Collection Efficiency of an Axial Flow Cyclone

Two models were recently published to predict the particle collection efficiency curve of an axial flow cyclone. Maynard (2000) [20] derived a mathematical model of an axial cyclone under laminar flow (channel Reynolds number < 2000) by assuming that the particle collection primarily occurred in the vane section and cyclone body. In the

vane section, the radial position of particles was evaluated, and the particle penetration was determined by comparing the total cross-sectional area to that containing survival particles. To model the particle penetration in the cyclone body, methodology similar to that developed by Nieuwstadt and Dirkzwager (1995) [21] was used, with the assumption of no turbulent aerosol mixing. The total penetration expression was then given by combining the penetrations through the vane section and cyclone body. Tsai et al. (2004) [16] established a model based on the same scheme as the Maynard's model for the cyclone vanes but calculating the tangential velocity and particle residence time differently. A fitting constant was then chosen to account for additional particle residence time in the cyclone body. Because of the low pressure operation of the axial flow cyclone in Tsai's study, the pressure effect was also taken into account by including the Cunningham slip coefficient (C_c) and flow volume expansion. The flow Reynolds number was further introduced to correlate the cutoff particle sizes of cyclones at different low pressure flow conditions. However, neither of these two models may be appropriate for modeling the particle collection efficiency of the axial flow cyclone tested in this chapter. Chiefly, the channel Reynolds number of the tested cyclone is much larger than 2000. As a result, the Maynard's model with the laminar flow assumption is not valid. For the model of Tsai et al. (2004) [16], the fitting constant used in the particle penetration calculation and the coefficients for the flow Reynolds number correction are purely empirical and limited to use for cyclones of equivalent sizes and operational flowrates. Therefore a new model for axial flow cyclones operating in the turbulence flow regime was proposed.

Similar to Maynard's model, our model estimates the particle penetrations separately in the helicoidal vane section and cyclone body. The overall cyclone collection curve of an axial flow cyclone is then calculated using the separate estimated particle penetrations. For the particle penetration in the vane section, the exponential equation between the particle Stokes number (StK) and the deposition efficiency (P_B) reported by Pui et al. (1987) [22] is employed. Pui et al. derived expression by curve fitting their experimental data at the 90° bend of the circular cross section. They found the penetration is independent of the flow Reynolds number and the Dean number ($\mathrm{Re}/\sqrt{R_b/a_t}$, and R_b and a_t are the centerline radius of curvature of the bend and inner radius of the bend) in the turbulent regime:

$$P_B = 10^{-0.963 StK} \qquad \text{and} \qquad StK = \frac{C_c \rho_p d_p{}^2 U}{18 \mu a_t},$$
(5.2)

where ρ_p is the particle density, d_p is the particle diameter, U is the mean flow velocity, μ is the fluid viscosity. Because of the rectangular cross section of the helix channel, in our proposed model the tube radius (a_t) is replaced by the equivalent hydraulic radius of the helix channel (a_h). The total penetration in one 3-turn vane (Pen_v) is approximated by the power law of P_B:

$$Pen_v = P_B{}^{12} = 10^{-(0.963 StK) \times 12} \quad \text{and} \quad StK = \frac{C_c \rho_p d_p{}^2 U}{18 \mu a_h}.$$
(5.3)

In the cyclone body, we applied the simplified Leith-Licht approach (1972) [2] to derive the particle penetration. Assuming complete radial mixing in the turbulent regime, the fraction of particles removed in the cyclone body can be written as

$$-\frac{dN}{N} = \frac{2R_2 dR - (dR)^2}{R_2{}^2}\bigg|_{R \to R_2} \approx \frac{2dR}{R_2}\bigg|_{R \to R_2} \quad \text{and} \quad dR = u_r dt \text{, and} \tag{5.4}$$

$$-\frac{dN}{N} \approx \frac{2u_r dt}{R_2}\bigg|_{R \to R_2}, \tag{5.5}$$

where R_2 is the radius of the cyclone body, and u_r is the particle radial velocity. Therefore, by integrating Eqn. (5.5) over the particle residence time in the cyclone body (t_b), the particle penetration is derived as

$$Pen_b = \exp\left\{\frac{-2}{R_2}\int_0^{t_b} u_r\big|_{R \to R_2} \, dt\right\}. \tag{5.6}$$

To complete the model derivation, t_b and the particle radial velocity (u_r) close to wall need to be evaluated. In our model, t_b was estimated by dividing the effective volume in the cyclone body (V_{eff}) by the flow rate (Q). The effective volume (V_{eff}) is defined as the total volume of the cyclone from the bottom of the vane section to the level of the natural vortex length (l), minus the volume of the central core (the same diameter as the V.F. diameter). The empirical equation established by Alexander (1949) [23] was used to calculate l:

$$t_{res} = \frac{V_{eff}(l)}{Q} \quad \text{and} \quad l = 2.3 D_e \left(\frac{Dc^2}{PT}\right)^{1/3}. \tag{5.7}$$

The particle radial velocity (u_r) is obtained by the force balance between the centrifugal force and particle drag force in the radial direction. The velocity can be determined in terms of the particle size (d_p) and tangential velocity (v_t):

$$u_r\big|_{R \to R_2} = \frac{\rho_p \cdot d_p{}^2 C_c}{18\mu} \cdot \frac{v_T{}^2}{R}\bigg|_{R \to R_2}. \tag{5.8}$$

The tangential velocity (v_t) is approximated by the velocity in a free vortex. The exponent n is used to take into account the deviation from the ideal condition. Alexander (1949) also provided an empirical equation for calculating n:

$$v_T \big|_{R \to R_2} \cdot (R_2)^n = U \cdot (De / 2)^n \text{, and} \tag{5.9}$$

$$n = 1 - \left[1 - 0.67 \cdot (Dc)^{0.14} \right] \cdot \left(\frac{T}{283} \right)^{0.3}. \tag{5.10}$$

Therefore, the particle penetration through the cyclone body is rewritten as

$$Pen_b = \exp\left\{ -\frac{\rho_p \cdot d_p^2 C_c}{9\mu R_2^2} \cdot \frac{U^2 \cdot (De/2)^{2n}}{(R_2)^{2n}} t_{res} \right\}. \tag{5.11}$$

The overall collection efficiency of the axial cyclone can thus be estimated by the following equation:

$$\eta = 1 - Pen_v \times Pen_b = 1 - \exp\left\{ -0.1643 \cdot \frac{C_c^2 \rho_p^2 d_p^4}{\mu^2 a_h} \times \frac{U^3 \cdot (De/2)^{2n}}{(R_2)^{2n+2}} t_{res} \right\}. \tag{5.12}$$

The comparison between the calculated and experimental particle collection efficiencies of the studied cyclone is shown in Fig. 5.6. In general, the model prediction is in good agreement with the experimental data. The predicted collection efficiency for particles smaller than 180 nm in diameter is slightly higher than experimental data. In addition, only the inertial deposition of particles was considered in the prediction of particle loss in the vane section. In the small size range, particle loss due to the turbulent diffusion should also be taken into account in the model prediction.
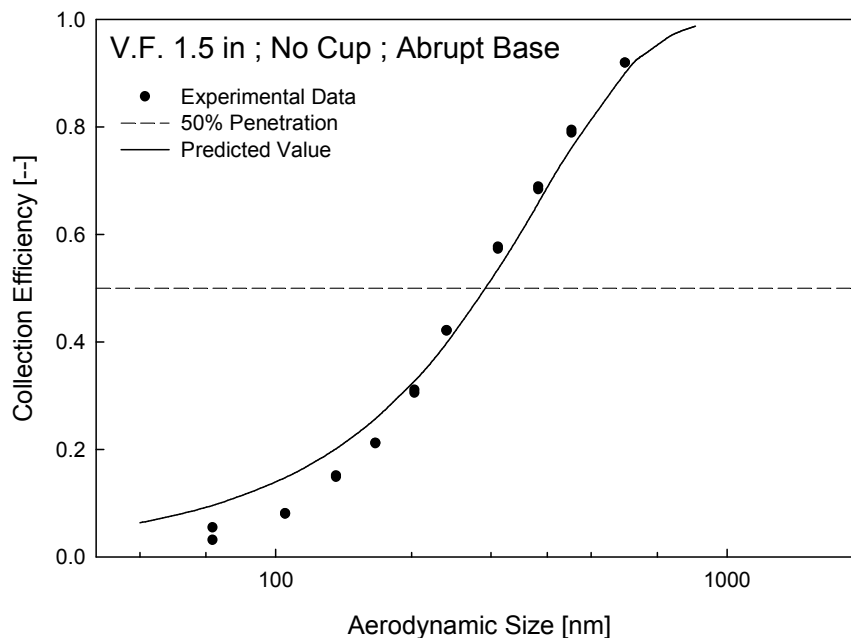
Figure 5.6   Comparison of experimental data with the predicted collection efficiency curve for the axial flow cyclone with the optimal configuration, operated at 50 lpm aerosol flowrate.

6. Summary:

The performances of axial flow cyclones of eight different configurations have been evaluated experimentally to investigate the effects of the upside-down cup, vortex finder (V.F.) length, and cyclone base geometry on the particle collection efficiency. The experiments revealed the effects of cyclone geometric dimensions on the axial flow cyclone performance are quite different from those for tangential flow cyclones. The particle cutoff sizes of cyclones with the upside-down cup are always larger than those of other cyclones, regardless of the cyclone base shape and V.F. length. It is believed the additional wall of the cup adds flow resistance. Consequently it slows down the flow swirling motion and reduces the centrifugal force for particle separation. Compound

127

effects of V.F. length and cyclone base shape are observed in our study. For the cases without the cup, an increase of V.F. length could either lead to the creation of bypass flow to the cyclone outlet or increase the particle residence time due to the additional turning of the upward vortex. These two possible scenarios depend on the shape of the cyclone base. The conical contraction base of the cyclones limits the downward vortex motion and results in aerosol flow bypass; hence the cyclone cutoff particle size is increased. For the abrupt contraction base, the outer vortex prefers to swirl downwards to the cyclone base and then re-turn upward to the V.F.. Particles of small sizes were therefore collected with the increase of particle residence time in cyclones. It is thus concluded that the optimal geometric configuration for axial flow cyclones is with an abrupt contraction base, without the upside-down cup, and with increased V.F. length.

A simple model has also been proposed to calculate the particle collection efficiency curve of an axial flow cyclone with the optimal configuration above and operated at high flowrate. Different from the models developed by Maynard (2000) [20] and Tsai et al. (2004) [16], the proposed model predicts the overall particle collection efficiency based on the separate estimations of particle collection in the vane section and cyclone body. The particle deposition expression in the 90° bend tube at high Reynolds numbers is used to estimate particle collection in the vane section. The simplified Leith and Litch approach is used to evaluate the collection efficiency of particles in the cyclone body. Reasonable agreement is achieved in the comparison between the experimental data and the predictions. Further, the proposed model well predicts the cutoff particle size of axial flow cyclones operated at high aerosol flowrates.

7. References

[1] Barth, W. (1956) Design and layout of the cyclone separator on the basis of new investigations. *Brennstoff-Warme-Krafat.* 8:1-9.

[2] Leith, D. and Licht, W. (1972) The collection efficiency of cyclone type particle collectors. *AIChE Sym.* Ser. 68:196-206.

[3] Saltzmann, B. E. and Hochstrassser, J. M. (1983) Design and performance of miniature cyclones for respirable aerosol sampling. *Environ. Sci. Technol.* 17:418-424.

[4] Moore, M. E. and McFarland, A. R. (1993) Performance modeling of single-inlet aerosol sampling cyclones. *Environ. Sci. Technol.* 27:1842-1848.

[5] Lidén, G. and Gudmundsson, A. (1997) Semi-empirical modelling to generalise the dependence of cyclone collection efficiency on operating conditions and cyclone design. *J. Aerosol Sci.* 28:853-874.

[6] Hsiao, T. C., Chen, D. R. and Son, S. Y. (2009) Development of mini-cyclones as the size-selective inlet of miniature particle detectors. *J. Aerosol Sci.* in press.

[7] Kim, J.C. and Lee, K.W. (1990). Experimental study of particle collection by small cyclones. *Aerosol Sci. Technol*, 12:1003-1015.

[8] Kenny, L. C. and Gussman, A. (2000) A direct approach to the design of cyclones for aerosol-monitoring applications. *J. Aerosol Sci.* 31:1407-1420.

[9] Lidén, G. and Gudmundsson, A. (1996) Optimisation of a cyclone to the 1993 international sampling convention for respirable dust. *Appl. Occup. Env. Hyg.* 11:677-688.

[10] Zhu, Y. and Lee, K. W. (1999) Experimental study on small cyclones operating at high flow rates. *J. Aerosol Sci.* 30:1303-1315.

[11] Xiang, R., Park, S. H. and Lee, K. W. (2001) Effects of cone dimension on cyclone performance. *J. Aerosol Sci.* 32:549-561.

[12] Zhu Y., Kim, M. C., Lee, K. Y., Park, Y. O., and Kuhlman, M. R. (2001) Design and performance evaluation of a novel double cyclone. *Aerosol Sci. Technol.* 34:373-380.

[13] Lim, K. S., Kim, H. S. and Lee, K. W. (2004) Characteristics of the collection efficiency for a cyclone with different vortex finder shapes. *J. Aerosol Sci.* 35:743-754.

[14] Wedding, J. B., Welgand, M. A., and Carney, T. C. (1982) A 10 μm cutpoint inlet for the dichotomous sampler. *Environ. Sci. Technol.* 16:602-606.

[15] Vaughan, N. P. (1988) Construction and testing of an axial flow cyclone pre-separator. *J. Aerosol Sci.* 19:295-305.

[16] Tsai, C. J., Chen, D. R., Chein, H., Chen, S. C., Roth, J. L., Hsu, Y. D., Li, W. and Biswas, P. (2004) Theoretical and experimental study of an axial flow cyclone for fine particle removal in vacuum conditions. *J. Aerosol Sci.* 35:1105-1118.

[17] Hinds, W. C. (1998) Aerosol technology (2nd ed.) New York: Wiley.

[18] Qian, F. and Zhang, M. (2005) Study of the natural vortex length of a cyclone with response surface methodology. *Comp. & Chem. Eng.* 29:2155-2162.

[19] Liu, B. Y. H. and Rubow, K. L. (1984) A new axial flow cascade cyclone for size characterization of airborne particulate matter. In: Liu, B. Y. H., Pui, D. Y., and Fissan, H. J. (Eds.), *Aerosols* (pp. 115-118). Amsterdam: Elsevier.

[20]   Maynard, A. D. (2000) A simple model of axial flow cyclone performance under laminar flow conditions. *J. Aerosol Sci*. 31:156-167.

[21]   Nieuwstadt, F. T. M. and Dirkzwager, M. (1995) A fluid mechanics model for an axial cyclone separator. *Industrial Engineering and Chemical Research*, 34:3399-3404.

[22]   Pui, D. Y., Romay-Novas, F. and Liu, B. Y. H. (1987) Experimental study of particle deposition in bends of circular cross section. *Aerosol Sci. Technol*. 7:301-315.

[23]   Alexander , R. M. (1949) Fundamentals of cyclone design and operation. *Proc. Aus. Ins. Min. Met.* NS 152-153, 203-228.

Chapter 6

Development of a Multistage Axial Flow Cyclone

1. Introduction

Long term human habitation on the Moon or Mars is one important vision for NASA's space exploration. However, the environments on the Lunar and Martian surfaces are very dusty. In most dust samples returned by Apollo and other Lunar missions, about 25 wt% of the lunar regolith is less than 20 μm, and it composed of sharp fragments of broken glass, basalt fragments, and agglutinates [1]. These lunar dusts could cause severe problems for life supporting equipment in space, such as seal failure, material abrasion, and vision obscuration. In addition, they have the potential to produce adverse physiological effects in human respiratory systems [2]. John Young, Apollo 16 astronaut, cautioned that "dust is the number one concern in returning to the moon". For the development of equipment and systems to be used in NASA's exploration missions, as well as for research on the health effects attributed to the dusts, simulants of Lunar and Martian dusts are used for testing and evaluation. Various dust effects on hardware and biological systems depend on particle sizes. In some cases interference from unwanted particles often complicates the R&D effort. Therefore, a reliable and efficient device to classify Lunar or Martian dust simulants from 20 μm to the ultrafine particle size range is needed.

To classify dry powders, the common technologies can be roughly categorized in two groups. One is sieving or screening, the other is air classification. Sieving has the advantage of setting a sharp upper limit on particle size, but it is slow and inefficient for particle sizes smaller than 20 μm [3]. For air classification, the general separation mechanism is to utilize the force balance between gravitational or centrifugal force and air drag. The air classification techniques are usually applied to particles in the super-

micrometer and upper sub-micrometer size ranges. Cyclones are the well-known centrifugal counter-flow air classifiers, widely used as particle collectors in a variety of industrial sectors because of their reliable performance and low operating and maintenance costs. In addition, cyclones are less prone to particle bounce and overloading, making them suitable for long term particle collection. Conventional cyclones introduce particle-laden flow tangentially into the cyclone body, with the outlet tube arranged perpendicularly to the inlet. Multi-stage cyclones of the above type have also been developed for particle classification [4]. Due to the tangential aerosol introduction of these multi-stage cyclones the overall configuration and flow pathway are bulky and rather complex.

In the other type of cyclones, axial flow cyclones, the aerosol flow both enters and exits cyclone body axially. Axial flow cyclones generally utilize a helix channel or a spindle vane to generate the swirling vortex motion for separating particles in the cyclone body. The primary advantage of axial flow cyclones is their relative ease of connect on with other devices or other axial cyclones in line. Similar to cascade impactors, several individual axial flow cyclones can be easily cascaded together to form a multi-stage cyclone to classify and collect particles with different sizes.

In this chapter we report a new multistage axial flow cyclone developed for the classification of NASA Lunar and Martian dust simulants. The developed cyclone has one impaction stage and five axial cyclone stages. The operational flowrate of the first three stages was 50 lpm. By operating the last two stages under low pressure, the cyclone is capable of classifying particles of aerodynamic size down to 40 nm. An empirical

model for the cutoff particle sizes of the axial flow cyclone stages under different Reynolds numbers was also established.

2. Axial Flow Cyclones

Compared to tangential flow cyclones, limited experimental data and models have been reported for axial flow cyclones. Wedding et al. (1982) [5] proposed a 10 μm cutpoint inlet for an axial flow dichotomous sampler operated at a flowrate of 16.7 lpm to collect masses representative of human thoracic particles. The inlet was termed an omni-directional cyclone, in which a swirling tube was utilized. The inlet design is essentially a variant of the axial flow cyclone for collecting particles with sizes larger than 10 μm. The collection efficiency curve of the inlet is close to that of thoracic deposition, but no model was reported to predict the performance of the inlet.

Vaughan (1988) [6] developed simple axial flow cyclones consisting of a helix channel, a 10 mm cylindrical body, and a flow oulet tube in each cyclone. Six different cyclone configurations with three body lengths and two channel depths were tested under aerosol flowrates ranging from 1.1 to 4.16 lpm. The cutoff size (d_{50}) of the tested cyclones was varied between 1.25 and 6.5 μm. The study also found that poor correlation between the particle cutoff size and the flow Reynolds number based on the inlet dimension. Vaughan used an empirical method proposed by Chan and Lippmann (1977) [7] to describe the particle penetration as a function of particle size. He also claimed that the axial flow cyclones could separate particles of smaller diameter and have higher pressure drop than tangential flow cyclones of comparable sizes. The above superior performance of axial flow cyclones was explained by three co-existing concentric

vortexes in the cyclone body. Nieuwstadt and Dirkzwager (1995) [8] investigated axial flow cyclones of another type for removing liquid droplets from a gas/liquid stream. The difference between the cyclone tested by Nieuwstadt and Dirkzwager (1995) [8] and Vaughan's is in the outlet design. The vortex finder typically installed from the cyclone base in cyclones was not used in the Nieuwstadt and Dirkzwager cyclone, allowing the entire flow stream to directly pass through the cyclone body. For droplet separation, only the downward vortex was generated in the cyclone body. As a result, the droplet collection efficiency of above cyclones is low. Because of the weak vortex swirling motion, the particle laden flow is less disturbed and the pressure drop of the axial flow cyclones is smaller than that of tangential flow cyclones. The above observations on axial flow cyclones are different from Vaughan's conclusion. To prevent the droplets from breakup during the separation process, a liquid/liquid axial flow cyclone with a bored-through outlet design is preferred. Nieuwstadt and Dirkzwager also developed a model utilizing a simple time-of-flight concept to estimate the particle penetration through the cyclones, and calculated the pressure field along the cyclone wall.

Maynard (2000) [9] proposed a mathematical model to predict the particle penetration of an axial flow flow cyclone under laminar flow (i.e., a helix channel Reynolds number less than 2000). The model assumed the particle separation occurred in the vane section/helix channel and in the cyclone body. To estimate the particle penetration in the vane section, the radial displacement of particles was evaluated with the implicit assumption of no particle mixing at any cross section of the helix channel. To calculate the particle collection in the cyclone body, a method similar to that used by Nieuwstadt and Dirkzwager (1995) [8] was applied. The free vortex with a constant

circulation was used to calculate the flow/particle tangential velocity in the cyclone body. However, the rationale for the vortex circulation expression used in the derivation is not given in Maynard's article. Further, the overall equation for calculating the total particle penetration through an axial flow cyclone is not explicit, requiring numerical iteration schemes to obtain the penetration given an input condition. Brunazzi et al. (2003) [10] tested axial flow cyclones of three types experimentally and developed a different time-of-flight model to predict their particle separation efficiencies. The model is based on the approach of Litch (1980) [11], with two hypotheses, one assuming complete radial mixing, and the other assuming the absence of radial mixing. By comparing the theoretical calculation to the experimental data, it is shown that complete radial mixing is more realistic than no mixing under their tested conditions.

Tsai et al. (2004) [12] first investigated the performance of the axial flow cyclone under low pressure conditions. A semi-empirical model was further established to interpret the data on particle penetration efficiency. The geometric configuration of the tested axial cyclones was similar to that of Vaughan (1988) [6], except that the helix channel used in Vaughan's cyclone was replaced by a turning vane. The experimental results reveal the cutoff size decreases with decreasing pressure in the cyclone body, because less air drag force is imposed on particles under low pressure. The cutoff size approached 43.3 nm when the pressure was reduced to 6 torr in the cyclone body. A semi-empirical model was also developed to model the particle collection efficiency of the test axial flow cyclones. In the model, the particle penetration in the vane section was based on Maynard's expression, and the particle collection in the cyclone body was estimated by applying the same expression to the empirical estimation of the total particle

transit time in the cyclone body. The work also reports the effect of the annular Reynolds numbers (using the annular spacing between the cyclone wall and outlet as the characteristic length) on the cutoff particle size at 50% penetration. Hsu et al. (2005) [13] found that for particle aerodynamic sizes less than 40 nm the collection efficiency of Tsai's axial flow cyclone can further increase as the particle diameter decreases at low Peclet numbers. They hypothesized the above observation was due to particle diffusion deposition. Therefore, the simplified convection-diffusion equation was solved analytically for two extreme conditions (i.e., the centrifugal force and the diffusion dominant cases). Tsai et al. (2007) [14] further employed the Fluent CFD package to perform numerical simulation on the flow and pressure field of their axial flow cyclone. Brownian dynamics was applied to calculate the particle trajectory, taking into account both centrifugal and diffusional effects, to determine the particle collection behavior of the axial flow cyclone.

3. Design of the Multi-stage Axial Cyclone
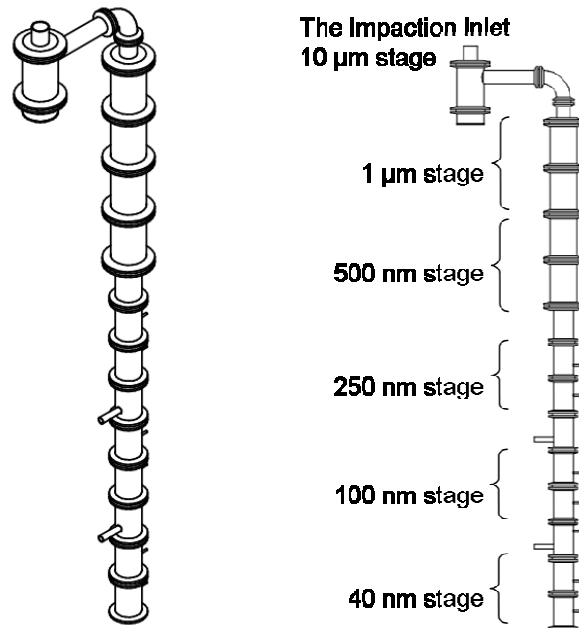
Figure 6.1a   Schematic diagram of the overall system of the prototype
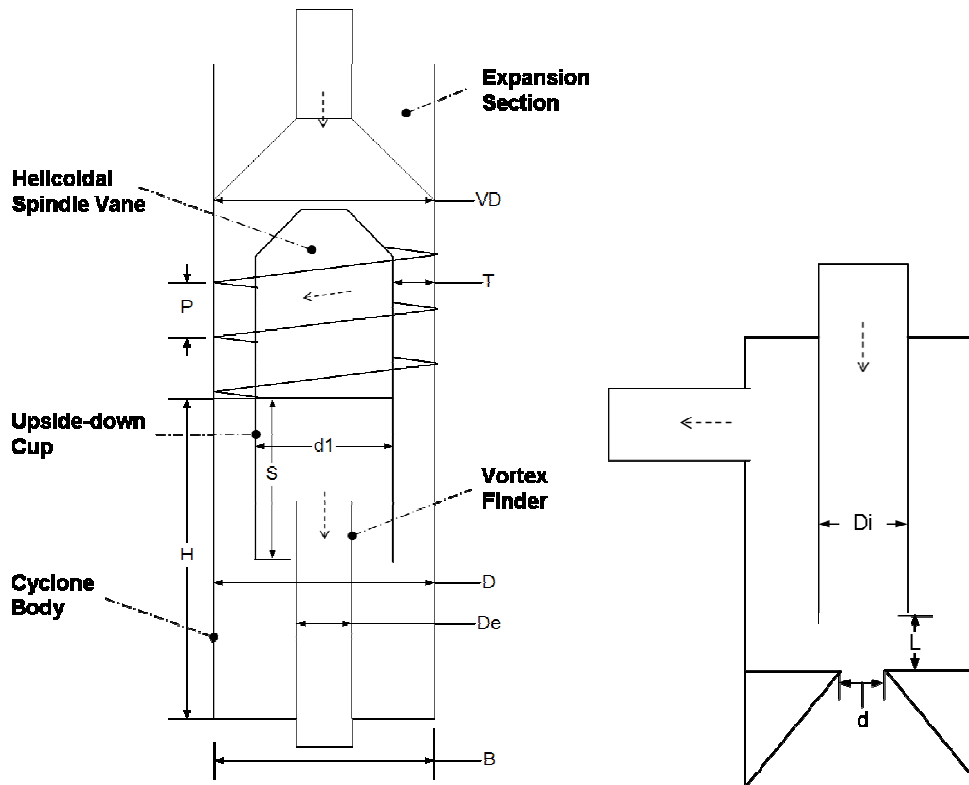
Figure 6.1b   Schematic diagram of an axial flow cyclone stage (Stages # 1-5)

Figure 6.1c   Schematic diagram of the impaction inlet

A schematic diagram of the prototype multi-stage axial flow cyclone is shown in Fig. 6.1a. The prototype consists of one impaction inlet and five axial flow cyclone stages (Stages# 1-5) corresponding to six nominal cutoff particle sizes of 10 μm, 1 μm, 500 nm, 250 nm, 100 nm, and 40 nm, respectively. The design of Vaughan's and Tsai's axial flow cyclones was used in the axial flow cyclone stages (shown in Fig 6.1b). Basically each cyclone stage comprises four components: an expansion section, helicoidal spindle vane, cyclone body with rectangular base, and a 1.5" long vortex finder/outlet tube. The above configuration providing the best particle collection performance was finalized after a series of evaluations of axial flow cyclones with various configurations in chapter 4. The aerosol stream enters each cyclone stage at the top inlet and is smoothly introduced into the vane section. The helicoidal channel in the vane section alters the direction of the axially incoming aerosol stream and generates vortexes in the cyclone body for particle separation and collection. In the cyclone body, particles first flow in the outer vortex and then continue to the inner vortex after reaching the end of the natural outer vortex length. The inner vortex spirals upward and exits the cyclone body through the vortex finder (outlet tube) to the following cyclone stage. Operating differently from Stage #1-5, the system inlet, shown in Fig. 6.1c, is in fact the impactor. To increase the dust loading capacity of the impaction stage of the impactor, a small hole connected to a dust collection chamber is centered on the impinging plate. A similar design was used to increase the particle loading capacity and to alleviate particle bounce of an earlier impactor [15]. Critical dimensions of all the stages in the prototype are listed in Table 6.1. The operational flowrate for the impaction inlet and Stages #1-3 was set at 50 lpm. The last two cyclone stages were operated at reduced aerosol flowrates even though 50 lpm

was the preferred flowrate since it matches the flowrate used for the impaction inlet and first three cyclone stages. The reduced flowrates for last two cyclone stages were a result of the limited capacity of the vacuum pumps used.

Table 6.1   Dimensions of the impaction inlet and each cyclone stage of the prototype

Stage		Impaction Inlet	Stage		# 1	# 2	# 3	# 4	# 5
Nominal d50		10 μm	Nominal d50		1 μm	500 nm	250 nm	100 nm	40 nm
Inlet Dia. (Di)	in	0.900	Vane Dia. (VD)	in	1.641	1.641	1.141	1.141	1.141
Impacting Length (L)	in	0.400	Pitch (P)	in	0.266	0.172	0.141	0.109	0.109
Dust Bin Hole (d)	in	0.400	Channel Depth (T)	in	0.321	0.180	0.149	0.149	0.149
			Body Dia. (D)	in	1.641	1.641	1.141	1.141	1.141
			Body Length (H)	in	3.000	3.000	2.300	2.300	2.300
			Outlet Dia. (De)	in	0.375	0.375	0.250	0.250	0.250

4. Experimental Setup
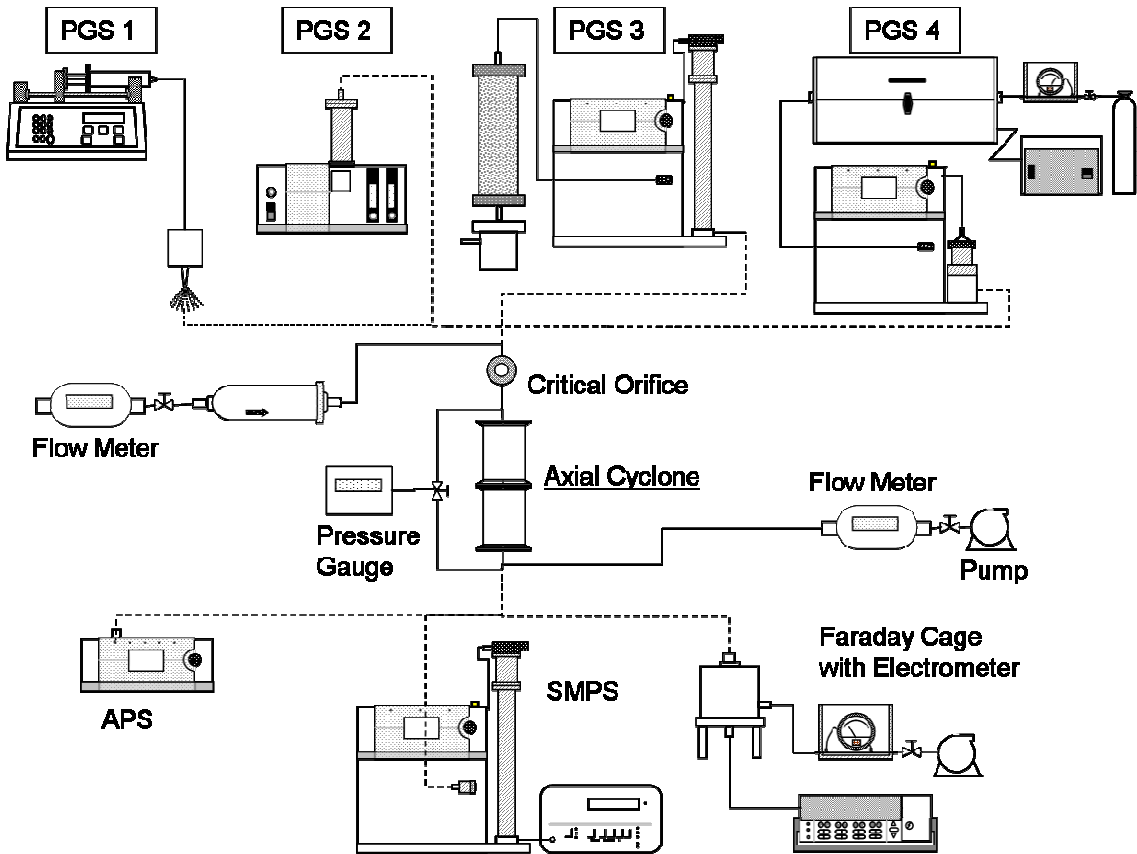
Figure 6.2   Schematic diagram of experimental setups for calibration of the impaction inlet and cyclone stages of the prototype

The performance of the prototype multi-stage cyclone was characterized by the particle collection efficiencies of the stages included. The efficiency of each stage was determined from upstream and downstream measurements of particle size distributions. The pressure drop across each stage was monitored by a barometric pressure gauge (626A13TAE, 1000 torr max or 626A11TAE, 10 torr max). The experimental setup shown in Fig. 6.2 was used to calibrate the cyclone performance. The particle generation system was immediately upstream of a tested stage, and the measurement systems for particle concentration or particle size distribution were immediately downstream. Since

the cutoff particle sizes of the prototype ranged from 40 nm to 10 μm, different particle generators and various particle sizing/counting instruments were used in the performance evaluation of individual stages.

In this study, four different particle generation systems (PGS) were employed to produce monodisperse or polydisperse particles in sizes ranging from supermicrometer to nanometer. PGS1 is an ultrasonic particle generator (Sono-Tek 8700) with solution fed by a syringe pump (Harvard 70-2000). PGS1 produced polydisperse potassium chloride (KCl) particles in the supermicrometer range. The ultrasonic nozzle was operated at 120 kHz. The number mean diameter (NMD) of produced particles was about 8 μm using KCl solution of 2.5% by volume. PGS2 is a fluidized bed aerosol generator (FBAG, TSI Model 3400A). Arizona fine dust (Powder Technology Inc. 12103-1 A2) was dispersed in air by PGS2 as challenge particles. The airborne aerodynamic size distribution of the Arizona fine dust had a mode size of around 1 μm and a geometric standard deviation (GSD) of 1.51. PGS3 includes a homemade collision atomizer and a differential mobility classifier (DMA TSI Model 3081). PGS3 was used to produce monodisperse KCl particles having electrical mobility sizes from 60 to 500 nm. For particles smaller than 60 nm, PGS4 included a tube furnace (Linburg/Blue Model 55322), and a Nano-DMA (TSI Model 3085) was utilized to generate monodisperse KCl particles. The ratio of the sheath flowrate to the aerosol in the electrostatic classifiers used in PGS3 and PGS4 was kept at 10. Because the operational flowrates of the prototype stages were generally larger than that used to operate the PGSs, filtered dry air was used to make up the flowrate difference between the PGSs and prototype stages. The flowrate of makeup air was monitored and controlled by a mass flow meter (TSI Model 4043) and a needle valve.

Along with four PGSs, two particle sizers and one aerosol count apparatus were applied to measure particle size distribution and concentration, respectively. For particles in the supermicrometer range, an Aerodynamic Particle Sizer (APS, TSI Model 3021) was used to measure particles with diameters ranging from 0.6 to 20 μm (aerodynamic size). A Scanning Mobility Particle Sizer (SMPS, TSI Model 3936) with a DMA (TSI Model 3081) and ultrafine condensation particle counter (UCPC TSI Model 3025) was used to measure particles in sizes from 10 to 700 nm (electrical mobility size). The SMPS measured the particle size based on the electrical mobility; hence, the particle density needed to be considered in converting electrical mobility particle size to aerodynamic size. The operational pressure of the last two stages of the prototype was below 200 torr, and the SMPS system described above was unable to operate at such low pressure level due to the limit of the UCPC. Accordingly, monodisperse particle testing was used to evaluate the performance of the last two stages of the prototype. PGS3 and PGS4 produced monodisperse test particles. Since particles classified by DMAs are electrically charged, a homemade Faraday cage with a sensitive electrometer (Keithley Model 6514) was ultilized to measure the current carried by the test particles. The particle concentration was then derived from the current measurement with the given volumetric sampling flowrate and particle charge status. The fraction of multiple-charged ones in DMA-classified particles was minimized by selecting the size in the right hand side of particle size distributions produced by PGS3 and PGS4.

The penetration curves of different stages of the prototype were determined by the combination of the above described PGSs and the particle sizing/counting instruments. The calibration setup for each stage is listed in Table 6.2. The vacuum pump (Leybold

Vacuum, Trivac B Rotary Vane Vacuum Pump, D65B) with a needle valve was used to control the flowrate needed during the calibration. Since the performance of stage cyclones (i.e., Stages #5 and #6) with a particle cutoff sizes less than 200 nm was strongly correlated with the pressure level in the stage body, orifices of different diameters were utilized to achieve the desired pressure conditions. A MKS Baratron type pressure gauge (626A13TAE, 1000 torr max and 626A11TAE, 10 torr max) was used to measure the absolute pressure before and after the test cyclone stage.

Table 6.2 Experimental setups for the individual calibration of the impaction inlet and cyclone stages

Stage #	Impaction Inlet	1	2	3	4	5
Aerosol Generator	PGS1	PGS2		PGS3		PGS4
Sizing or Counting Apparatus	Aerodynamic Particle Sizer (TSI 3021)		SMPS (TSI 3936)		Faraday Cage with Electrometer	

5. Results and Discussion

The measured particle collection efficiency curves for all the stages of the multi-stage prototype are shown in Fig. 6.3. The impaction inlet and Stages #1-3 were tested at an aerosol flowrate of 50 lpm and at near ambient pressure. Stages #4 and 5 were calibrated at flowrates of 20 and 1 lpm under absolute pressures of 274 and 21.8 torr, respectively. The aerodynamic cutoff sizes (d_{50}, defined as the particle size at 50% collection efficiency) are also summarized in Table 6.3. They are 11.3 μm, 1.0 μm, 500

nm, 290 nm, 161 nm, and 40.9 nm for impaction inlet and Stages 1-5, respectively. The sharpness of the penetration curves was in general characterized by the geometric standard deviation (σ_g), defined as the square root of the ratio of particle size with 84% collection efficiency to that of 16 % efficiency. The sharpness of the impaction inlet is about 1.43. The sharpness of Stages #1-4 was higher, ranging between 1.70~1.90. Because of the diffusion loss of small particles in the cyclone stage operated under low pressure, Stage #5 had the least sharp particle collection efficiency, exhibiting a slightly high collection value in the small particle size range. The above phenomenon was also observed in the work of Hsu et al. (2005) [13].
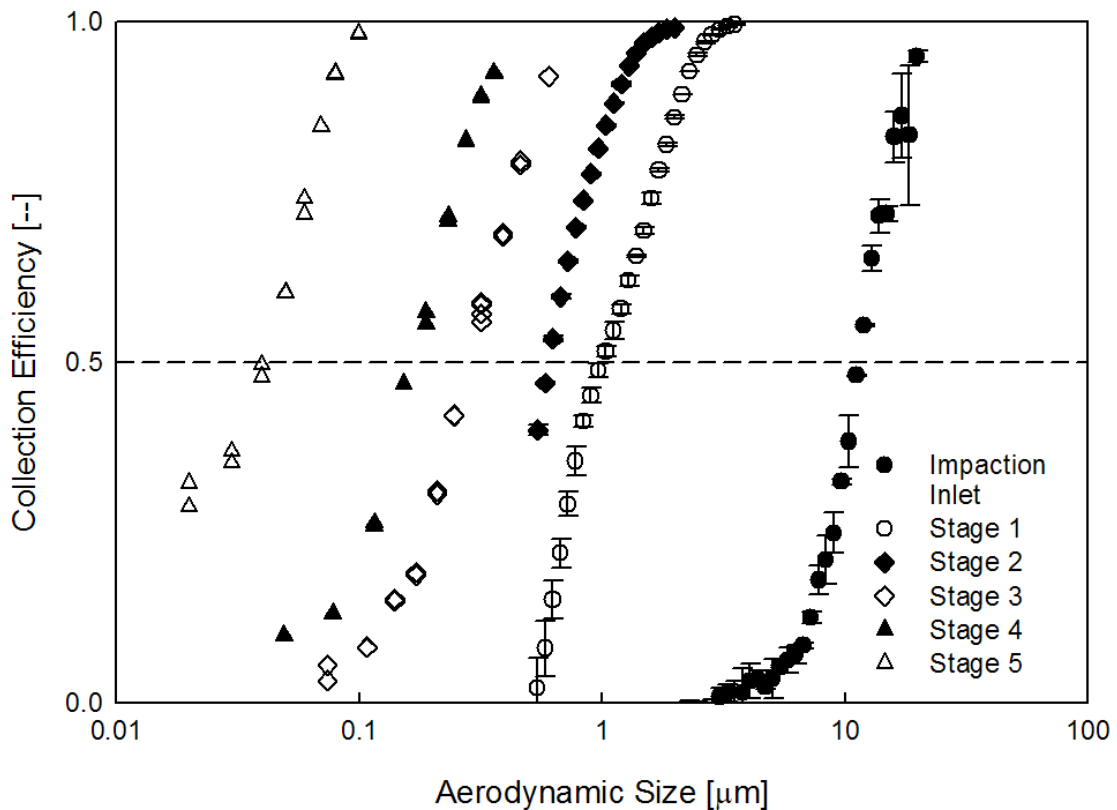
Figure 6.3 Measured collection efficiency curves of the impaction inlet and cyclone stages of the prototype at the designed flowrates

145

Table 6.3 Experimental cutoff particle sizes of the impaction inlet and cyclone stages

Stage #	Nominal d_{50}		Test Q [lpm]	up P [torr]	down P [torr]	Re # [–]	EXP d_{50aero}	
Impaction Inlet	10	µm	50	760	760	3046	11.3	µm
1	1	µm	50	760	760	41499	1	µm
2	500	nm	50	760	760	114241	500	nm
3	250	nm	50	760	578	117488	290	nm
4	100	nm	20	274	175	60423	161	nm
5	40	nm	1	21.8	6.7	3021	40.9	nm

Two designs of multi-stage cyclones have been reported. One is a five-stage tangential flow cyclone operated at 28.3 lpm flowrate, designed by Smith and Wilson (1979) [4]. The other one is a five-stage cascade axial flow cyclone operated at 30 lpm flowrate, developed by Liu and Rubow (1984) [16]. The smallest cutoff particle sizes in above two cyclones were 0.32 and 1.05 µm, respectively. Compared with these multi-stage cyclones, the prototype was operating under a higher flowrate of 50 lpm, covering a wider cutoff size range and collecting particles of smaller sizes. As expected, the smaller cutoff particle size of the prototype resulted in higher pressure drop that reported for the Smith and Wilson cyclone (i.e., 170.2 torr). No pressure data was published for the Liu and Rubow cascade axial cyclone. Note that comparable performance under higher operation flowrate was achieved by our prototype if Stages #4 and #5 were not used.

The cutoff particle sizes of Stages #4 and #5 were strongly influenced by the upstream pressure condition. Tsai et al. (2004) [12] already demonstrated that the cutoff size of an axial flow cyclone can be reduced to below 100 nm under low pressure operation. Two different pressure conditions were further tested for Stages #4 and #5.

146
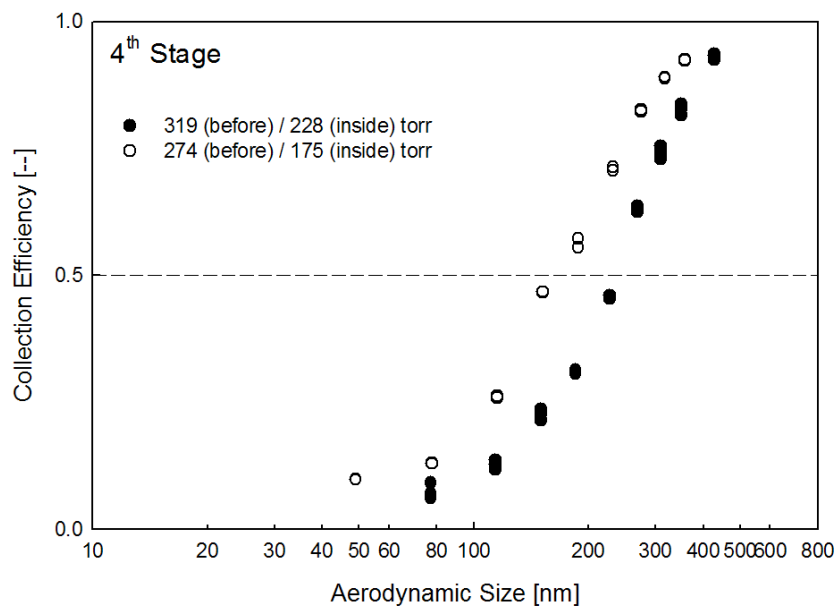
(6.4a)
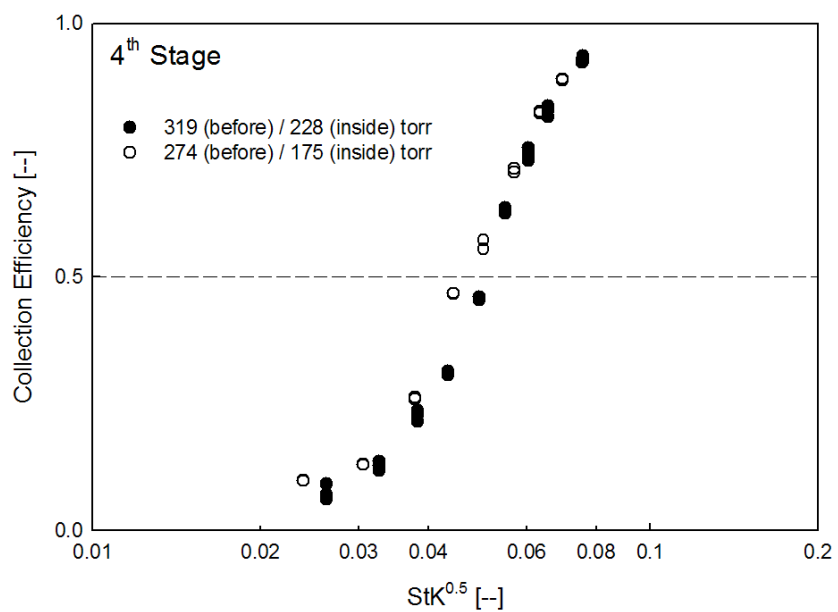
(6.4b)

Figure 6.4 Particle collection efficiency curves for the 4th cyclone stage under two different pressure conditions (i.e., 319 torr and 274 torr). (a) aerodynamic size as the abscissa; (b) square root of StK number as the abscissa

For Stage #4, the d_{50} decreased from 229 to 161 nm as the upstream pressure was reduced from 319 and 274 torr, as shown in Fig. 6.4a. Since cyclones utilize the balance between centrifugal force and particle drag to separate particles, the fact of d_{50} decreasing with upstream pressure can be explained by the smaller drag experienced by a particle at lower pressure. As a result, the cyclone can capture smaller particles under the lower pressure condition. This effect is embedded in the slip coefficient (C_c) of the particle Stokes number (StK). Reduction of the cyclone upstream pressure increases the mean free path (i.e., λ) of the carrier gas and the particles' Knudsen number, defined as $2\lambda/D_p$, consequently resulting in larger values of C_c and StK #. However, the characteristic cutoff Stokes number (StK$_{50}$) of an individual cyclone stage is only a function of the cyclone dimensions and flow conditions, not the cyclone's operational pressure. Fig. 5.4b plots the same data given in Fig. 6.4a, using the StK number as the abscissa. As expected, the collection efficiency curves at two different operational pressure levels collapse into one in Fig. 6.4b. Note that Tsai et al. (2004) [12] applied the average of upstream and downstream cyclone pressures for the StK number calculation. Different from the observation of Tsai et al. (2004) [12], we found the StK number calculated based on the upstream pressure of an individual cyclone stage better correlates the curves under different pressures.

Moreover the spread of the different particle collection efficiency curves of axial flow cyclone stages can be narrowed by using the square root of the Stokes number, which is also considered to be the dimensionless particle size ($\widetilde{d}_{50}$). Fig. 6.5 shows a plot of particle collection efficiency as a function of the square root of the particle Stokes

number. As expected, the $\tilde{d}_{50}$ s of different cyclone stages are not the same because of the different operation conditions, but the spread of the efficiency curves is much reduced.
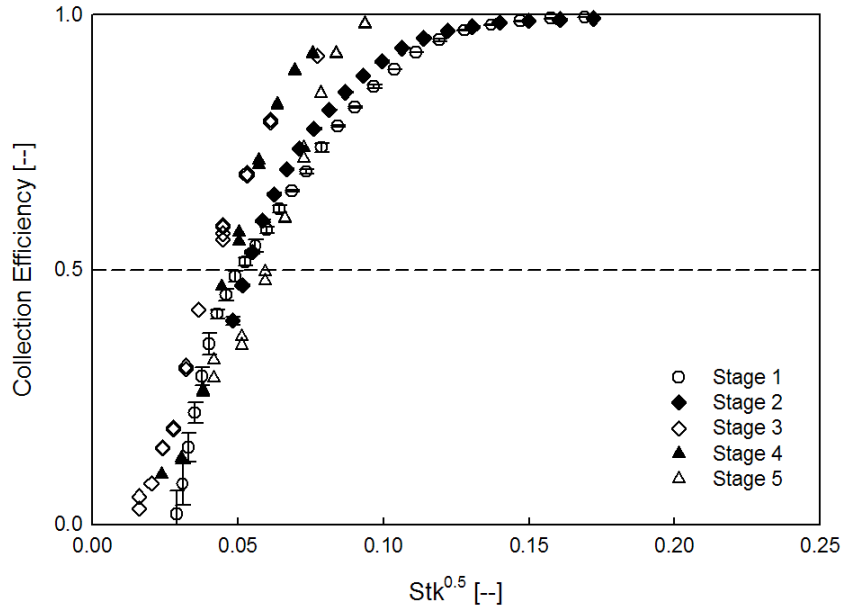
Figure 6.5   Collection efficiency curves as a function of the particle Stokes number
for all the axial flow cyclone stages of the prototype

To characterize the performance of different axial flow cyclone stages under the different flowrates, the $\tilde{d}_{50}$ s were plotted against the flow Reynolds number (Re#). The $\tilde{d}_{50}$ and the Re number are defined as

$$\tilde{d}_{50} = \sqrt{StK} = \sqrt{\frac{C_c \rho_p d_{50}^{\,2} V_i}{9\mu D_c}} \tag{6.1}$$

$$\mathrm{Re} = \frac{\rho_g V_i D_c}{\mu}, \tag{6.2}$$

where ρ_p and ρ_g are the particle and carry fluid density, V_i is the average flow velocity in the vane section, and μ is the fluid viscosity. The cyclone body diameter, D_c, is used as the characteristic length in the calculation of both $\tilde{d}_{50}$ and Re.
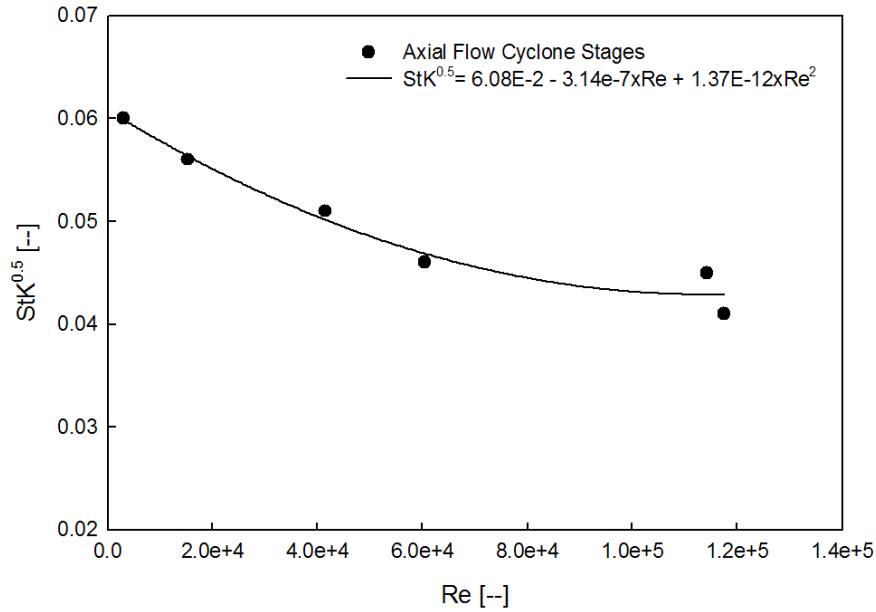
Figure 6.6   Dimensionless cutoff size (i.e., $\text{StK}_{50}{}^{0.5}$) vs. flow Reynolds number for all axial flow cyclone stages

As shown in Fig. 6.6, the $\tilde{d}_{50}$ decreased with increasing Re and then approached to a constant value of 0.043 as the cyclone was operated at Re larger than 10^5. This observation was also reported for tangential flow cyclones in previous literature [17-20]. Overcamp and Scarlett (1993) [19] further concluded that the $\text{Stk}_{50}{}^{0.5}$ generally falls between 0.025 and 0.05 for a tangential flow cyclone operating under high Reynolds number (Re> 10^5), and they suggested values within this range can be chosen as the preliminary cutoff $\text{Stk}_{50}{}^{0.5}$ for a new industrial tangential cyclone. Note that the definition of the StK given in Overcamp and Scarlett (1993) [19] is different from that used in our

study, and the proposed StK range will need to be revised if the current definition of the StK is used. The work further cautioned that the correlation between $\tilde{d}_{50}$ and Re is strongly related to the cyclone configurations. Since the stages of the prototype axial flow cyclone have similar geometric dimensional ratios, an empirical quadratic equation was used to express the correlation between $\tilde{d}_{50}$ and Re for Re up to $1.2*10^5$. The cutoff size of an axial flow cyclone with a similar dimensional ratio can therefore be estimated by this empirical model under different Reynolds numbers. When Re is larger than $1.2*10^5$, the $\tilde{d}_{50}$ can be assumed to be the constant value of 0.043. Expressed mathematically,

$$\tilde{d}_{50} = 6.083e^{-2} - 3.142e^{-7} \cdot \mathrm{Re} + 1.375e^{-12} \cdot \mathrm{Re}^2, \qquad \text{for } 0 < \mathrm{Re}\# < 1.2 \cdot 10^5, \text{ and}$$

$$\tilde{d}_{50} \cong 0.043, \quad \text{for Re } \# > 1.2 \cdot 10^5. \tag{6.3}$$

The experimental data reported above are for the impaction inlet and cyclone stages operated at the designed flowrates. Additional calibration was also done on the assembled prototype, because the pressure condition and the flowrate for the impaction inlet and cyclone stages are not identical to those in the stage calibration, especially for the last two cyclone stages. The flowrate discrepancy between the actual and designed conditions resulted from the limited load capacity of the vacuum pump used. As a result we operated the 4th cyclone stage at the flowrate of 11.0 lpm instead of the 20.0 lpm in the calibration. The upstream pressure of the 4th cyclone stage was 141.5 torr at a flowrate of 11.0 lpm. With lower upstream pressure than that during the calibration, the d_{50} of the 4th cyclone stage was therefore reduced to 109 nm. Fig. 6.7 shows the overall operation scheme for the prototype, given the limited load capacity of the vacuum pump used. To maintain different flowrates for cyclone stages #4 and #5 two additional small

vacuum pumps were connected to remove excess aerosol flow from the prototype. Orifices were installed before the last two axial flow cyclone stages to reduce the cyclone upstream pressure to the expected level and to control the flowrates for Stages #4 and #5.
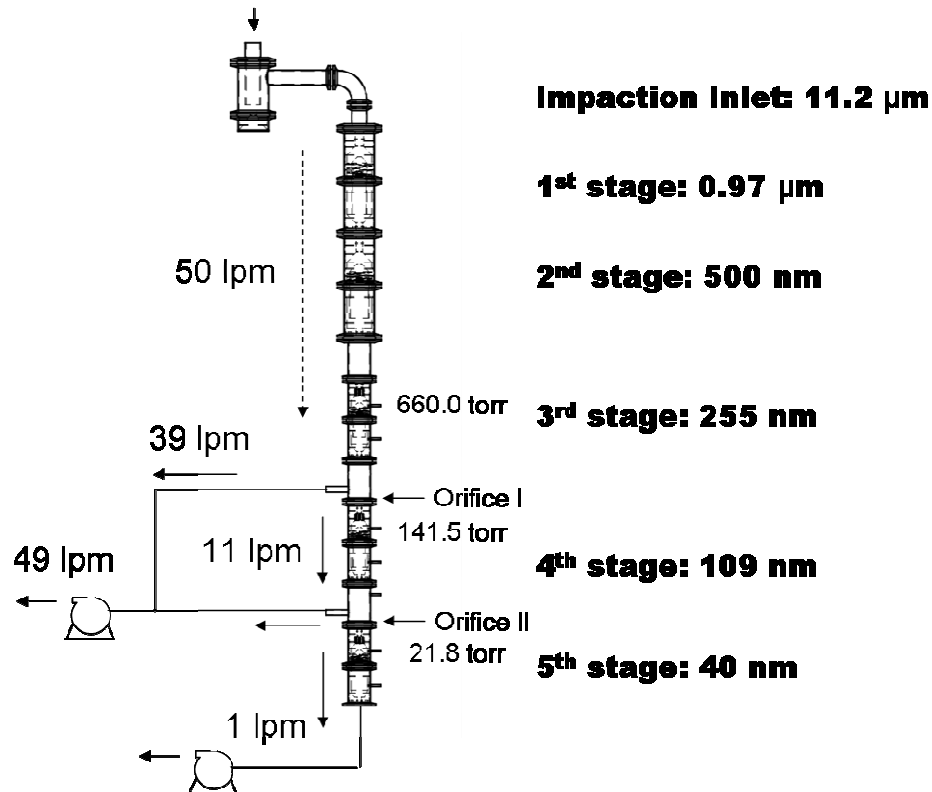
Figure 6.7   Overall operational scheme of the prototype and the corresponding cutoff sizes for the impaction inlet and cyclone stages

6. Summary

A prototype multi-stage cyclone system having an impaction inlet and five axial flow cyclone stages with cutoff sizes of 11.3 μm, 0.97 μm, 500 nm, 255 nm, 109 nm, and 40 nm has been developed to classify Lunar and Martian dust simulants for various NASA research and development work. To calibrate the impaction inlet and cyclone stages, four different particle generation systems (PGS1-4) were used to generate test

particles in sizes ranging from tens of micrometers down to several nanometers. Two particle size spectrometers (APS and SMPS) and an aerosol electrometer (consisting of a Faraday cage with a sensitive electrometer) were applied to measure the particle size distribution and concentration upstream and downstream of the impaction inlet and of each cyclone stage of the prototype. The calibration of each cyclone stage was done at the designed flowrate condition. The experimental cutoff sizes of several cyclone stages are slightly deviated from those targeted. However, adjustments to the operational flowrate and pressure of the assembled multi-stage cyclone system brought the cutoff particle sizes of each stage within 10% of the target sizes. Compared with two existing multi-stage cyclones, i.e., a five-stage tangential flow cyclone [4] and a five-stage cascade axial flow cyclone [16], the prototype has the advantages of covering a wider size range and collecting particles of smaller sizes at a higher flowrate. However, due to the lower particle cutoff size, the pressure drop across the prototype was greater than those of the earlier cyclones mentioned. Nevertheless, without the Stages #4 and #5, the performance and pressure drop of the prototype are comparable to those of Smith and Wilson's cyclone system.

The experimental data also reveal that the cyclone collection efficiency curves of Stages #4 and #5 varied with the operational upstream pressure. The cutoff sizes of Stages #4 and #5 decreased with a decrease of upstream pressure, because of less drag force acting on particles in a lower pressure environment. By converting the particle diameter to the square root of the particle Stokes number (i.e., dimensionless particle size, $\tilde{d}_{50}$), the particle collection efficiency curves of each cyclone stage (either Stage #4 or #5) under different pressure conditions can be nearly collapsed into one at the same flow

153

Reynolds number (Re#). In other words, the pressure effect on the cutoff particle sizes of Stages #4 and #5 can be mainly attributed to the change of the slip coefficient (C_c) in the Stokes number. This study found that, to better scale the collection efficiency curves under different pressure conditions, the upstream pressure should be used to calculate the particle Stokes number instead of the average of upstream and downstream pressures of the test cyclone stage. The relationship between the $\tilde{d}_{50}$ and Re for tangential flow cyclones was also observed for axial flow cyclone stages. For Re less than $1.2*10^5$, the $\tilde{d}_{50}$ decreased with an increase of Re. The value of $\tilde{d}_{50}$ approached a constant for Re larger than $1.2*10^5$. An empirical model was then derived to describe the correlation between $\tilde{d}_{50}$ and Re# with the given geometric dimensions of cyclones. The model can be used to predict the cutoff particle sizes for axial flow cyclones with similar dimensional ratios under different flow rates.

7. References

[1]   Johnson, S. W., Taylor, G. J. and Wetzel, J. P. (1992). Environmental Effects on Lunar Astronomical Observatories, The Second Conference on Lunar Bases and Space Activities of the 21st Century, NASA. Johnson Space Center 1:329-335.

[2]   Gaier, J. R. (2005). The Effects of Lunar Dust on EVA Systems During the Apollo Missions, NASA/Glenn Research Center, Cleveland, Ohio. TM—2005-21361.

[3]   Sung, M. D., Dent, N. M. and Kalechofsky, N. (2007). Ultra Fine Particle Size Classification via Sieving in Liquid Nitrogen, PARTEC 2007 International Congress on Particle Technology, Nuremburg, Germany, March, 2007.

[4]   Smith, W. B. and Wilson, R. R. (1979). The Five-Stage Cyclone System for in Situ Sampling, *Environ. Sci. Technol*. 13:1387-1392.

[5]   Wedding, J. B., Welgand, M. A. and Carney, T. C. (1982). A 10-μm Cutpoint Inlet for the Dichotomous Sampler, *Environ. Sci. Technol*. 16:602-606.

[6]   Vaughan, N. P. (1988) Construction and Testing of an Axial Flow Cyclone Preseparator, *J. Aerosol Sci.* 3:295-305.

[7]   Chan, T. and Lippmann, M. (1977). Particle Collection Efficiencies of Air Sampling Cyclones: an Empirical Theory, *Environ. Sci. Technol*. 11:377-382.

[8]   Nieuwstadt, T. M. and Dirkzwager, M. (1995). A Fluid Mechanics Model for an Axial Cyclone Separator, *Ind. Eng. Chem. Res.* 34:3399-3404.

[9]   Maynard, A. D. (2000). A Simple Model of Axial Flow Cyclone Performance Under Laminar Flow Conditions, *J. Aerosol Sci.* 31:151-167.

[10]   Brunazzi, E., Paglianti, A. and Talamelli, A. (2003). Simplified Design of Axial-Flow Cyclone Mist Eliminators, *AIChE J.* 49:41-51.

[11]   Licht, W. (1980). Air Pollution Control Engineering, Dekker, New York.

[12]   Tsai, C. J., Chen, D. R., Chein, H. M., Chen, S. C., Roth, J. L., Hsu, Y. D., Li, W. and Biswas, P. (2004). Theoretical and Experimental Study of an Axial Flow Cyclone for Fine Particle Removal in Vacuum Conditions, *J. Aerosol Sci.* 35:1105-1118.

[13]   Hsu, Y. D., Chein, H. M., Chen, T. M. and Tsai, C. J. (2005). Axial Flow Cyclone for Separation and Collection of Ultrafine Particles: Theoretical and Experimental Study, *Environ. Sci. Technol*. 39:1299-1308.

[14]   Tsai, C. J., Chen, S. C., Przekop, R. and Moskal, A. (2007). Study of an Axial Flow Cyclone to Remove Nanoparticles in Vacuum, *Environ. Sci. Technol*. 41:1689-1685.

[15]   Biswas, P. and Flagan, R. C. (1988). The Particle Trap Impactor, *J. Aerosol Sci.* 19:113-121.

[16]   Liu, B. Y. H. and Rubow, K. L. (1984). A New Axial Flow Cascade Cyclone for Size Characterization of Airborne Particle Matter. In: *Aerosols* (Edited by Liu, B. Y. H., Pui, D. Y. and Fissan, H. J.), 115-118. Elsevier, Amsterdam.

[17]   Moore, M. E. and McFarland, A. R. (1990). Design of Stairmand-Type Sampling Cyclones, *Am. Ind. Hyg. Assoc. J.* 51:151-159.

[18]   Scarlett, S. E. (1987). An Investigation of Cyclone Performance Using Dimensional Analysis. M.S. Thesis, Clemson University, Clemson, SC.

[19]   Overcamp, T. J. and Scarlett, S. E. (1993). Effect of Reynolds Number on the Stokes Number of Cyclones, *Aerosol Sci. Technol*. 19:362-370.

[20]   Lidén, G. and Gudmundsson, A. (1997). Semi-empirical Modeling to Generalise the Dependence of Cyclone Collection Efficiency on Operating Conditions and Cyclone Design, *J. Aerosol Sci*. 28:853-874.

Chapter 7

Dissertation Accomplishments and Recommendations for Future Work

1. Summary of Accomplishments

In this dissertation, two control technologies for airborne particles, aerosol filtration and inertial separation, were studied. For aerosol filtration, specific attension was paid to the loading behaviors (the pressure drop evolution curves) of filters challenged by liquid-coated particles. For inertial separation, fundamental studies of an axial cyclone and the development of a cascaded axial cyclone were described. These works will not only enhance researchers' understanding of specific particle control technologies, but also help engineers to develop better devices for solving current environmental problems or fulfilling industrial needs. The studies accomplished within this dissertation -- submicron liquid-coated particle loading, supermicron liquid-coated particle loading, the effect of geometric configuration on the collection efficiency for axial flow cyclones, and the development of a multistage axial flow cyclone -- are summarized as follows.

1.1   Submicron liquid-coated particle loading

Filter performance when loaded with submicron liquid-coated particles has been studied. To systematically perform such a study, we developed two liquid-coated particle generation systems. One uses the heating-evaporation-condensation method, in which solid nuclei mix with coating liquid vapor in a well-controlled temperature environment. The other uses co-solvent method, in which an aqueous salt solution mixes with oil/alcohol solution and then is atomized by a collison atomizer. Both systems can generate submicron liquid-coated particles of different liquid volume percentages, but they have different advantages and disadvantages. The particle size distributions

generated by the heating-evaporation-condensation method have smaller GSDs, but their total concentrations are less than those generated by the co-solvent method, because the condensation system included electrical classification of the upstream nuclei. One concern for the condensation system is oxidation. In the presence of oxygen, heating could change the properties, such as viscosity or surface tension, of coating liquids, and also create additional particles through oxidation, contaminating the coated particles. Therefore, the transition behaviors of loading curves can not be characterized under well controlled conditions.

The issue can be mitigated by replacing air with pure nitrogen. The anoxic co-solvent method was proved to be reliable for long term loading experiments, and the results show the loading behaviors of filters loaded with liquid-coated particles are very different from those loaded with completely solid or liquid particles, typically obtained in laboratory settings. As the liquid volume percentage increases, the loading behavior of liquid-coated particles transits from that of loading pure solid particles to that of loading pure liquid particles. It was also found that the transition behaviors change for test filters with different surface properties, such as oleophobic or oleophilic. Similar behaviors were reported for wettable (hydrophilic) and non-wettable (hydrophobic) filters by Agranovski and Braddock (1998). Therefore, the filter surface properties can play important roles in liquid-coated particle loading. However, unfortunately, we are unable to further characterize the effect of filter surface properties, since the effect of filter structure is difficult to exclude. To avoid the effect of filter structure, coating liquids with different properties, instead of filters with different surface properties, were tested, and the effects were explored for supermicron liquid-coated particle loading.

1.2   Supermicron liquid-coated particle loading

For supermicron liquid-coated particle loading, the co-solvent method was used and the coated particles were generated by ultrasonic aerosol generator. Several series of liquid-coated particle loading testes, from pure solid particle loading to pure liquid particle loading, were performed under different operation conditions to study the effect of the filter material, the coating liquid properties, the particle size, and the face velocity. The general transition behaviors of loading curves are similar to those observed for submicron cases.

We further examined the loaded filters under SEM, and found that the structure of the deposited particles changes from long dendrites to short dendrites and then to mixed clumps as the amount of the liquid in the liquid-coated particle increases. It is believed that at low liquid volume percentages, capillary force becomes important through the formation of liquid bridges. When the particle is coated with more liquid, viscous force and frictional force become dominant over capillary force because microscopic "debris flow" can occur on the filter fibers. Later, for pure liquid particle/droplet loading, the surface tension of the liquid is critical, since it determines the shape of coalesced loaded droplets. For cellulose filters, the scenario is more complex due to the additional mechanism of absorption by cellulose fibers.

Based on the experimental observation, the liquid volume percentage of 50% seems a critical value for supermicron liquid-coated particle loading behavior. When the liquid volume percentage is less than 50%, the loading curves for the coating liquids of low surface tension, DEHS, light mineral oil, and castor oil, at different liquid volume percentages, can converge into one as the total loaded particle volume is replaced by the

160

solid particle volume. This convergence directly evidences that the pressure drop is mainly caused by the solid core of liquid-coated particles. It is also found that by converting the loaded particle volume to the loaded particle surface area the loading curves of different particle sizes overlap. When the liquid-coated particle consists of more than 50% liquid, the loading curves for different coating liquids are spread out in the order of their viscosity, for both the glass fiber filter and the cellulose filter. In addition, the effect of face velocity seems to be insignificant for liquid-coated particles loaded on the cellulose filter in the range from 5 to 20 cm/s, and the absorption of liquid by cellulose could be the reason.

The behaviors of glycerol loading curves are unique due to its high surface tension and high viscosity, and their data were excluded for establishing the empirical model for predicting the overall transition behavior of liquid-coated particle loading. The model consists of two parts. For liquid volume percentages less than 50%, Bergman's model for solid particle loading is modified to predict the pressure drop evolution up to four times the initial pressure drop. Similar to Thomas et al's concept, the loaded filter is divided into two layers. One collects all challenge particles, and the pressure drop is estimated by Bergman's model. The other layer remains as a clean filter during the loading process, and the pressure drop is calculated by Davis' equation. The total pressure drop is the summation of those in these two layers. For coating liquid percentages larger than 50%, the experimental data is fitted by a power type equation with two parameters, the exponent (n) and the critical volume (V_{cr}). The correlations among these two parameters and the core diameter fraction (X) and the viscosity of coating liquid are established for the glass fiber filter and the cellulose filter. Notice that

161

the current model does not include the parameter of surface tension, and it is only applicable for coating liquids of low surface tension (< 35 mN/m).

1.3   Effect of Geometric Configuration on the Collection Efficiency for Axial Flow Cyclones

The particle collection efficiencies of axial flow cyclones with eight different geometric configurations, operated at 50 lpm aerosol flowrate, were evaluated. The geometric variation of test cyclones includes the optional addition of an upside-down cup, two vortex finder lengths, and two cyclone base shapes. Under various configurations, the cutoff aerodynamic particle size of axial flow cyclones changed from 272 to 448 nm. The results show that configuration effects on the collection efficiency of axial flow cyclones are different from those of tangential flow cyclones. The observation of different geometric effects on particle collection by axial and tangential flow cyclones is attributed to the flow pattern difference between cyclones of two types. It is further concluded that the optimal configuration for axial flow cyclones is with an abrupt contraction base, without an upside-down cup and with an increased vortex finder length. A simple model combining the model of Leith and Litch (1972) and the tubing loss in 90° bends at high Reynolds numbers has also been proposed to predict the particle collection efficiency curve of the optimal axial flow cyclone among those tested.

1.4   Development of a Multistage Axial Flow Cyclone

A multi-stage axial cyclone was developed for NASA to classify Lunar and Martian dust simulants for health studies, and the performance of each stage was

carefully calibrated. The multistage cyclone is comprised with six stages and the cutoff particle sizes are 11.3 μm, 0.97 μm, 500 nm, 255 nm, 109 nm, and 40 nm. The firs stage is an impactor , and the other five stages are cyclones with axial flow design. Each stage can be operated independently to connect to the other device in line or cascaded together to do the multiple-size particles classification and collection. The first four stages are designed to operate at 50 lpm under nearly ambient pressure, and the last two stages are required to operate at 11 lpm and 1 lpm under low pressure conditions to separate particles less than 200 nm.

Form the dimensionless analysis, it is found flow Reynolds number and Stokes number are two critical parameters to characterize the axial cyclone performance. The dimensionless cutoff size (square root of particle Stokes number) is a function of flow Reynolds number. In addition, for a fixed cyclone configuration, the collection efficiency curves are shifting toward left with decreasing the pressure before cyclone. However, by converting the particle diameter to the root of the Stokes number, the curves can be converged into one at the same Reynolds number.

2. Recommendations for Future Research

Liquid-coated particle loading is still a relative new field in filtration studies, and more work needs to be done to elucidate the behaviors and mechanisms. The following recommendations are for future research related to the liquid-coated particle loading inspired by the studies done within this dissertation:

   □   Directly inspect the dynamic development of liquid-coated particle dendrites
       or the coalescence process on filter fibers during loading tests

□ Measure the contact angles between coating liquids and particles or coating liquids and filter fibers

□ Explore the effect of surface tension, and extend the model to include the parameter of liquid surface tension

□ Perform the loading tests of externally mixed liquid droplets and solid particles

□ Test filters loaded with liquid droplets and solid particles by turns

□ Study the absorption characteristics of cellulose filters during liquid-coated particle loading

□ Re-examine the effect of face velocity on the glass fiber filter over a wider velocity range

For axial flow cyclones or traditional tangential flow cyclones, the prediction of cyclone performance still relies highly on empirical or semi-empirical models. Hence detailed numerical simulations of the flow field and the particle trajectory inside cyclones should be helpful for optimization of cyclone performance. In addition, the particle movement through the continuous, transition, and free molecular flow regions (fly through the Knudsen Layer) remains a challenging problem for fundamental study. In the field of cyclone design, a cyclone with multiple inlets has the potential to reduce the pressure drop of the cyclone, but remains little studied.

Appendix A

Development of Mini- Cyclones

as the Size-Selective Inlet of Miniature Particle Detectors

Ta-Chih Hsiao and Da-Ren Chen[*]

Department of Energy, Environmental and Chemical Engineering
Washington University in St. Louis
St. Louis, MO 63130

And

Sang Young Son

Department of Mechanical Engineering
University of Cincinnati
621 Rhodes Hall, P.O. Box 210072
Cincinnati, OH 45221-0072

1. Introduction

Substantive evidence has indicated that common human diseases, such as asthma, cardiovascular disease, and cancer, result from a complex interplay between genes and environmental factors, including chemical, particulate, and biological toxins. NIH had thus launched an institute-wide Genes and Environment Initiative (GEI) to understand such interaction between genes and environmental factors. However, much uncertainty is encountered in the surveyed data from population studies aimed at investigating the role of gene-environmental interaction in human health and disease, primarily due to the lack of measurement tools for assessing a person's exposure to these toxins. With the support of GEI, a variety of environmental sensors are currently under the development. A miniaturized condensation particle counter (CPC) is thus being developing for monitoring the number concentration of particles with diameters less than 1 $\square$m. As a part of the mini- CPC development, mini-cyclones will be used as the size selector included in the compact package of the mini-CPC. Further, personal assessment of particulate exposure is in strong demand for epidemiological studies in general. With the increasing evidence the toxicity of nanoparticles, one of the building blocks for Nanotechnology, the need for a miniature particle detecting device enabling nanoparticle monitoring at the personal level is gaining much attention, particularly for worker protection in nanoparticle manufacturing facilities.

Edwards et al. (2005) built a portable dual-chamber particle monitor, combining ionization chamber sensing and optical scattering sensing. Edward's device has been used to mitigate exposures of wildland firefighters. A personal nanoparticle sizer based on the particle electrical-mobility technique has also been developed by Qi, Chen, and

Greenberg (2008) to measure the size distribution of particles with diameters less than 300 nm. During measurement the removal of particles with the diameters larger than the upper size limit of these miniature particle devices remains a challenge, because of the low sampling flowrate operation of these miniature devices. The presence of large particles in sampled air and the deposition of large particles in these mini-devices will affect the device's performance or even damage the detection sensor. However, large particles are ubiquitously present in ambient air. A size selective inlet is therefore needed for miniature particle detectors. A cyclone is an efficient particle separation device for the removal of large particles, because of its high particle loading capacity and relatively low pressure drop.

Most commercially available small cyclones are designed primarily for personal sampling. The penetration curves of these cyclones generally attempt to match the recent CEN-ISO-ACGIH respirable or thoracic convention. The 50% cutoff sizes (d_{50}) of the respirable and thoracic conventions are 4 μm and 10 μm. Gorner et al. (2001) have studied the performance of 15 respirable aerosol samplers and reported the cutoff sizes of the cyclone samplers range from 1.89 to 5.81 μm. Further, the nominal operation flow rates of these respirable cyclones, typically in the range of 0.8 to 2.5 lpm, are much higher than those used in the miniature particle devices. Thus, we can not use these respirable cyclones as the size-selective inlet for miniature particle detectors. In this article we report the development of two prototype mini-cyclones to remove particles larger than 1 μm and 0.3 μm at a flowrate of 0.3 lpm. The design and experimental evaluation of prototypes are given. A comparison of mini-cyclone experimental data with two existing models for small cyclones is also made in this study. An empirical model for

the prediction of cyclone performance is further developed. The developed mini-cyclone model can serve as the tool for the design of future mini- cyclones.

2. Review of Cyclone Modeling

An accurate universal model for the prediction of the penetration curve and/or cutoff size (defined as the particle size at the 50% particle penetration) of a cyclone is needed for cyclone design. Cyclones for the removal or collection of particles larger than specific diameters have been investigated for several decades. Many semi-empirical models have been proposed in literature (e.g., Lapple, 1950; Barth, 1956; Leith and Licht, 1972; Dietz, 1981; Mothes and Löffler, 1988). The most common modeling approach is based on a force balance between the centrifugal force and drag force acting on particles (Barth, 1956; Dietz, 1981; Mothes and Löffler, 1988). The other approach is the so-called "time-of-flight approach" (Lapple, 1950; Leith and Licht, 1972), which considers the residence time of a particle traveling from its initial position to the cyclone wall. Both approaches reveal valuable understanding about how the device geometries and operating conditions affect the performance of a cyclone. However, the agreement on the prediction of cyclone performance among these cyclone models is typically less satisfactory when applied to cyclones with different configurations, especially small cyclones. Iozia and Leith (1989) have investigated five cyclone models, including Barth (1956), Dietz (1981), Lapple (1950), Leith-Licht (1972) and their own models, a refinement of Barth's model, for the prediction of the 50% cutoff particle size for different cyclones. The results showed that the ratio of the predicted and experimental cutoff sizes could be as large as three in some cases. Moore and McFarland (1990) further concluded that using these

169

models to predict the performance of a small cyclone would introduce large errors. It is believed that the observed deviation among the predicted and experimental data is because the models were developed for industrial cyclones. Small cyclones and industrial ones are typically operated at different flow regimes. Overcamp and Scarlett (1993) re-examined the Stokes numbers of cutoff particle sizes (Stk_{50}) of five cyclones from published literature and found that the Stk_{50} decreases with increasing flow Reynolds numbers in the lower Reynolds number regime. The observation is, however, inconclusive when cyclones were operated in the high Reynolds number flow regime. In other words, the effect of Reynolds number on the cutoff particle size could be significant for small cyclones. Moreover, several parameters embedded in these industrial cyclone models (for example, the effective number of turns of the flow in Lapple's model and the maximum tangential velocity in the Barth's model) rely on empirical estimation or assumption. These empirical parameters in the industrial cyclone models were difficult to correctly estimate and were often used as a factor to fit with the experimental data. It is thus tricky to use these models for the performance prediction of a new small cyclone.

The empirical model developed by Chan and Lippmann (1977) was the first model focusing on small cyclones. A hyperbolic tangent equation with four empirical constants was used to successfully fit the particle collection curves of six air sampling cyclones under different flow rates. However, these four empirical constants can not be calculated from the cyclone dimensions, so the model is limited to the studied cyclones. Another empirical/semi-empirical model has been extensively studied for small cyclones, establishing the correlation between the dimensionless cutoff size (i.e., $C^{0.5}D_{50}/D_c$ where C_c is the Cunningham correction and D_c is the cyclone body diameter) or Stk_{50}, and

different flow Reynolds numbers (Saltzmann and Hochstrassser, 1983; Saltzmann, 1984; Moore and McFarland, 1990, 1993, 1996; Overcamp and Scarlett, 1993; Liden and Gudmundsson, 1997; Kenny and Gussman, 1997, 2000). Beeckmans and Kim (1977) first introduced the correlation idea by fitting the collection curve of a sampling cyclone as a function of the Reynolds number (based on cyclone body diameter) and the Stokes number. Saltzman and Hochstrasser (1983) proposed a linear equation to describe the relationship between the dimensionless cutoff particle size (i.e., $C^{0.5}D_{50}/D_c$) and the outlet tube Reynolds number in a log-log scale. The outlet tube Reynolds number is calculated using the outlet diameter as the characteristic length. They tested fifteen variants of a 19.05 mm sampling cyclone and found the fitting constants varied little. Moore and McFarland (1990) suspected the monotonous fitting constants were due to the identical cyclone body utilized by all 15 cyclones in the work of Saltzman and Hochstrasser (1983). Four Stairmand-type sampling cyclones with different body diameters were then tested in McFarland's work. The collected data were interpreted as Stk_{50} against the cyclone body Reynolds number. It was shown that the relationship between the Stk_{50} and cyclone body Reynolds number becomes quadratic rather than linear in the log-log plot. The work further found the Froude number has a minor effect on the Stk_{50} vs. Reynolds number relationship in the range from 1.5 to 6.0. Moore and McFarland (1993) later extended the experiment to similar Stairmand-type sampling cyclones with different outlet diameters. Instead of establishing the quadratic logarithmic function between Stk_{50} and Reynolds number, a method similar to that used in Saltzman and Hochstrasser's study (1983) was applied to analyze the experimental result. They demonstrated the annular flow Reynolds number (i.e., the number using the annular spacing between the wall of cyclone body and

the outlet tube as the characteristic length) better correlates with dimensionless cutoff sizes. Kenny and Gussman (1997, 2000) simplified this type of modeling (i.e., the correlation between annular flow Reynolds number and dimensionless cutoff size) to predict the performance of a group of small cyclones with a pre-determined dimensional ratio (a cyclone family) operating at different sampling flow rates. The Reynolds number calculation was further reduced to the ratio of flow rate to the cyclone body diameter.

Liden and Gudmundsson (1997) pooled together the published data of four different types of cyclones, including the Stairmand cyclone, Lapple cyclone, German Z cyclone, and Southern Research Institute (SRI) cyclones II and III. They suggested the correlation of dimensionless cutoff size vs. the annular flow Reynolds number is more promising than that of Stk_{50} vs. the cyclone body Reynolds number. They also created a generalized correlation equation using the multi-linear regression method. One new parameter, the ratio of the vortex finder length to the cyclone body diameter, was introduced in the model.

As noted in the literature, most of cyclone models discussed above are practical for the performance prediction of a cyclone family. Only the models developed by Saltzman-Hochstrasser (1983), and Liden and Gudmundsson (1997) attempted to cover different configurations of cyclones. An interesting fact is that the coefficients associated with the Reynolds number in both models are the same, even though the Reynolds numbers defined in the models are different. The Saltzman-Hochstrasser model uses the outlet tube Reynolds number, while the Liden-Gudmundsson model employs the annular flow Reynolds number. These two models were thus used to estimate the cutoff particle size of prototype mini-cyclones during the mini- cyclone design phase. The comparison

172

between the model prediction and the experimental data for prototype mini-cyclones is presented in this article.

3. Design of Prototype Mini-cyclones

The target cutoff sizes for the two prototype mini- cyclones in this study are 1.0 and 0.3 μm, operated at a flow rate of 0.3 lpm. The selection of 0.3 lpm sample flow rate is primarily because of the flow operation of the prototype mini-CPC. It is also due to the load specification and energy consumption of the on-board mini-pump to be used in the mini-CPC, allowing an 8-hour operation per each battery charge.
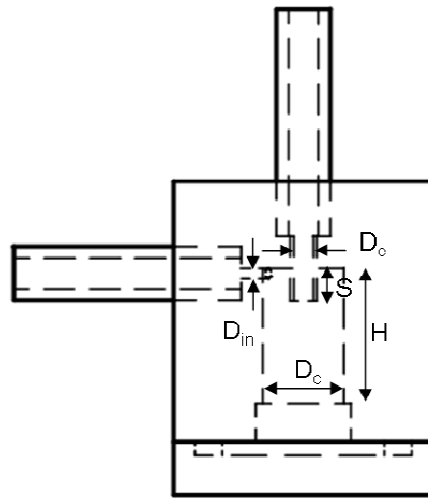
Figure 1. Schematic diagram of prototype mini-cyclones

The configuration of the prototype mini-cyclone is shown in Fig. 1. It is similar to those referred to the Extra-Sharp-Cut Cyclone (ESCC) series (Kenny and Gussman, 2000). Similar to the ESCC, the base of the prototypes is cylindrical rather than conical, and the cross section of the cyclone inlet is circular instead of rectangular. The ESCCs

were previously reported to give a sharp penetration curve with the advantages of easy manufacture and low maintenance. Note that the smallest model of the ESCC cyclone family reported has a cyclone body diameter of 0.321" with a cutoff particle size of 1.83 μm at a 1.0 lpm sampling flow rate. The other existing small ESCC cyclone is that used in front of the TSI Electrical Aerosol Detector (EAD, TSI 30b70A) for removing particles larger than 1 μm under a sampling flow rate of 2.5 lpm. Both small ESCC cyclones can not satisfy our desired cutoff size at the target sampling flowrate. Based on the empirical model given by Kenny and Gussman (2000), the body diameter of the ESCC cyclone should be 0.069" to reach a cutoff particles size of 0.3 μm at 0.3 lpm flowrate. It is difficult to manufacture a cyclone with the body diameter as calculated. The geometric dimensions of the prototype mini-cyclones developed in this study shall be considered as a new design, not a member of ESCC cyclone family.

Table 1. Geometrical dimensions for prototype mini-cyclones

Model	Dc [in]	Din [in]	De [in]	S [in]	H [in]
1.0 μm mini-cyclone	0.188	0.023	0.046	0.075	0.313
0.3 μm mini-cyclone	0.103	0.014	0.025	0.042	0.174

The geometric dimensions of the prototype mini-cyclones described here can be defined by five parameters: the inlet diameter (D_{in}), the cyclone body diameter (D_c), the outlet diameter (D_e), the vortex finder length (S), and the cyclone body length (H). The geometrical dimensions of prototypes are given in Table 1. Prior to the construction, the Saltzman-Hochstrasser and Liden-Gudmundsson models were initially applied to estimate the performance of different configurations of mini-cyclones with a cutoff size of 1.0 μm. The body diameters of the prototype mini-cyclones body are 0.1875" and

0.1031" for the cutoff sizes of 1.0 and 0.3 μm, respectively. The overall sizes of both mini-cyclones are less than the size of a U.S. quarter coin. It is believed that these prototype mini-cyclones are the smallest ever built.

4. Experimental Setup

The particle penetration curve and the pressure drop of a cyclone at different sampling flow rates are two primary data for the evaluation of cyclone performance. The pressure drop of the prototype mini- cyclones was measured by a mechanical pressure gauge at different flow rates. The sampling flow rate through the test cyclones was controlled by a vacuum pump with a needle valve and was monitored by a TSI mass flowmeter (TSI 4043). The primary flow calibrator (Gilian Gilibrator 2) was used to calibrate the TSI mass flowmeter.

To acquire the penetration curve and consequently determine the cutoff particle size of a prototype mini- cyclone at a specific sampling flow rate, the upstream and downstream particle size distributions of the cyclone were measured. The aerosol penetration through the mini-cyclones was then calculated by taking the ratio of the particle concentration at each size bin of the measured particle distributions, under the assumption that transport losses in the tubing are identical for both upstream and downstream size distribution measurements. Four different sampling flow rates (0.3, 1.2, 1.6, 2.0 lpm) were tested for the prototype 1.0 μm mini-cyclone, and three different flow rates (i.e., 0.25 , 0.3 and 0.35 lpm) were tested for the prototype 0.3 μm mini-cyclone. Most penetration measurements were performed using polydisperse potassium chloride (KCl) particles. Monodisperse PSL particles and/or classified monodisperse KCl particles

were also generated to further verify the 50% cutoff particle size, d_{50}, at the sampling flow rate of 0.3 lpm.
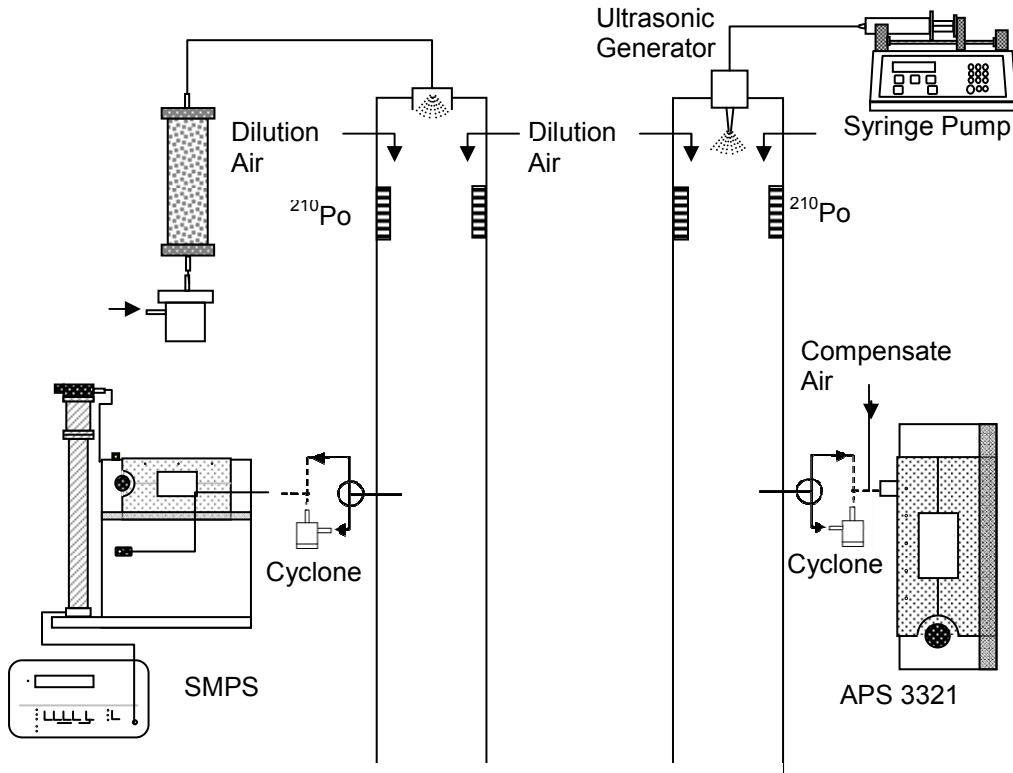
(a.) Submicron Particle Test System   (b.) Supermicron Particle Test System

Figure 2. Schematic diagram of experimental setups for the performance evaluation of mini-cyclones

To test the prototype mini-cyclones for a wide particle size range, two experimental setups were used to measure the penetration of particles. Fig. 2 shows the schematic diagram of both experimental setups. Polydisperse potassium chloride (KCl) particles were generated in both setups. The differences between the setups are (1) the particle generation methods and (2) the particle detecting instruments. For the submicron particle test system shown in Fig. 2(a), a homemade Collison atomizer was applied to

generate submicron KCl particles. Generated particles were passed through a neutralizer and diffusion dryer prior to entering the testing chamber. The neutralizer, with a radioactive Po^{210} source of 0.5 mCi, produced bi-polar ions and reduced the electrical charges on droplets to reach the equilibrium charge distribution. The diffusion dryer was used to remove water from droplets generated in order to form submicron test KCl particles. The Scanning Mobility Particle Sizer (SMPS, TSI 3096) was used to measure the particle size distributions upstream and downstream of the cyclones. Since the test flow rate for the mini-cyclones was not always equal to the aerosol sampling flow rate for TSI SMPS, an additional flow control was required to keep the aerosol sampling flow rate of SMPS constant. Prior to the penetration measurement, NIST-traceable 0.5 um PSL particles were used to check the SMPS sizing performance.

In the supermicron particle test setup shown in Fig. 2(b), an ultrasonic particle generator (Sono-Tek 8700) was used to produce supermicron KCl particles. The KCl solution was delivered by a syringe pump (Harvard 70-2000) to the ultrasonic generator. Four Po^{210} radioactive sources, located right under the ultrasonic nozzle, were installed along the test chamber wall to neutralize electric charges on droplets. Clean dry air was introduced into the testing chamber to completely evaporate the solvent (water) of the droplets to yield solid KCl particles. A TSI Aerodynamic Particle Sizer (APS, TSI Model 3321) was used to measure the particle size distributions upstream and downstream of the prototype cyclones. The APS was able to detect particles with aerodynamic sizes ranging from 0.6 to 20 μm. An additional flow control was needed to match the total 5.0 lpm sampling flow rate of APS. Supplemental air was cleaned by a HEPA grade filter before

mixing it with the aerosol flow, and the rate of added flow was controlled by a MKS mass flow controller (MKS 1479A).

The complete cyclone penetration curve for particles in the supermicron and submicron ranges was then compiled by combining the SMPS and APS data. Special attention was paid to the merger of the APS and SMPS data sets, because the operational principles for sizing particles are different for SMPS and APS. SMPS measures the electrical mobility size of particles, and APS detects the aerodynamic size of particles. Because the cyclone captures particles based on their aerodynamic properties, the electrical mobility size was converted to the aerodynamic particle size for merging the penetration data.

In addition, the pressure drop for the mini-cyclone could be significant at higher flow rates, and the pressure effect on the size distribution measurements by APS or SMPS need to be carefully handled. In this study, the APS is only used under the case of 1.0 μm mini-cyclone at 0.3 lpm, and pressure drop is as low as 1.8 in H_2O. Therefore, the pressure effect on the supermicron particle measurements is negligible. However, the SMPS was used under higher flow rates, and the pressure effect on the measurements needs to be considered. During the data processing, the concentration change due to the volume expansion under lower pressure condition was corrected based on the inline flow and pressure measurements. Furthermore, the pressure effect was also taken into account in the conversion from the particle electrical mobility size to the aerodynamic size.

5. Results and Discussion

Table 2. Cutoff sizes for prototype mini-cyclones under different flow rates

Model	0.3 lpm	1.2 lpm	1.6 lpm	2.0 lpm
1.0 μm mini-cyclone	898±42 nm	402±14 nm	284±13 nm	211±6 nm
Model	0.25 lpm	0.35 lpm		
0.3 μm mini-cyclone	395±9 nm	288±10 nm		

5.1 Penetration Curve
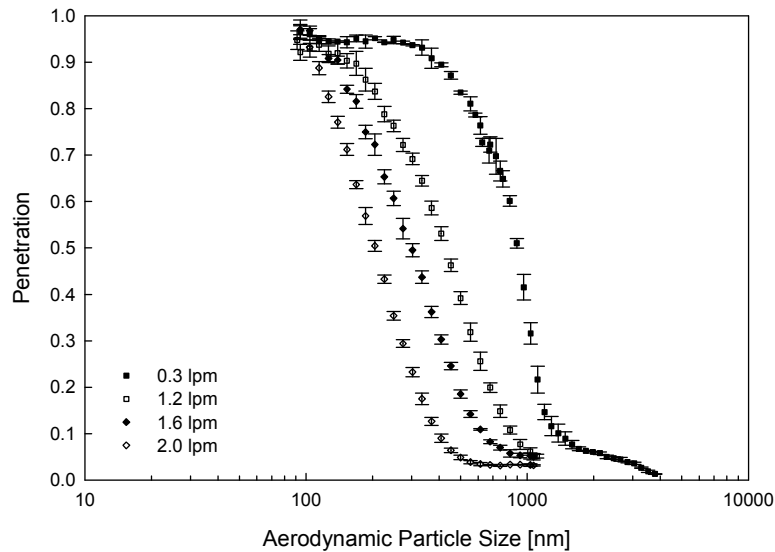
Figure 3.   Particle penetration as a function of aerodynamic particle size for the 1.0 μm mini-cyclone

Fig. 3 shows the particle penetration curves as a function of aerodynamic particle size for the prototype 1.0-μm mini- cyclone at different sampling flow rates. The aerodynamic cutoff sizes for the mini- cyclone were 0.898 um, 402 nm, 284 nm, and 211 nm at 0.3, 1.2, 1.6, and 2.0 lpm flow rates, respectively (Table 2.). For the 0.3 lpm flow rate, monodisperse Polystyrene Latex (PSL) particles of 1 μm in diameter were also used to verify the result obtained from the polydisperse particle testing. The penetration for 1-

μm PSL particles was 45% ± 1%, which is consistent with the polydisperse particle data. The decrease of cyclone cutoff particle size with the increase of sampling flow rate is attributed to the stronger centrifugal force created at the higher flow rate. Since inertial force is the primary mechanism for cyclone separation, the Stokes number (Stk) is usually used for characterizing this observation. The 50% cutoff Stokes number (Stk_{50}) for cyclone is defined as

$$Stk_{50} \equiv \frac{C_c \rho_p d_{p,50}^2 U_i}{9 \mu D_c},$$

where C_c is the Cunningham correction (dimensionless); ρ_p is the particle density (kg/m^3); $d_{p,50}$ is the aerodynamic particle size at the 50% penetration (m); U_i is the inlet velocity (m/s); μ is the fluid viscosity (kg/m-s); and D_c is the cyclone body diameter (m). However, the correlation between the Stk_{50} number and the cyclone body Reynolds number was poor for the data collected in our study.

The better correlation shown in Fig. 4 was found by using the dimensionless cutoff particle size and the annular flow Reynolds number. The linear relationship between the dimensionless cutoff size and the annular flow Reynolds number, reported by Moore and McFarland (1990), was also observed in this study. A linear regression equation for the collected data was also obtained and plotted. The slope and the interception constant of the linear equation are -0.6744 and -1.315, with a coefficient of determination (i.e., r^2 value) of 0.966. The same equation was then used to determine the cyclone body diameter of the prototype 0.3-μm mini-cyclone. The test result reveals that the cutoff sizes of the 0.3-μm mini- cyclone were around 395 nm and 288 nm under sampling flow rates of 0.25 and 0.35 lpm, which further confirms the feasibility of using

this equation to predict the cutoff particle size of the mini-cyclones with similar configuration and size. Moreover, by incorporating the data collected for the prototype 0.3-μm mini-cyclone in the linear regression model, the r^2 value was further improved to 0.970, and the slope and the interception constant were slightly modified, to -0.656 and -1.398, respectively.
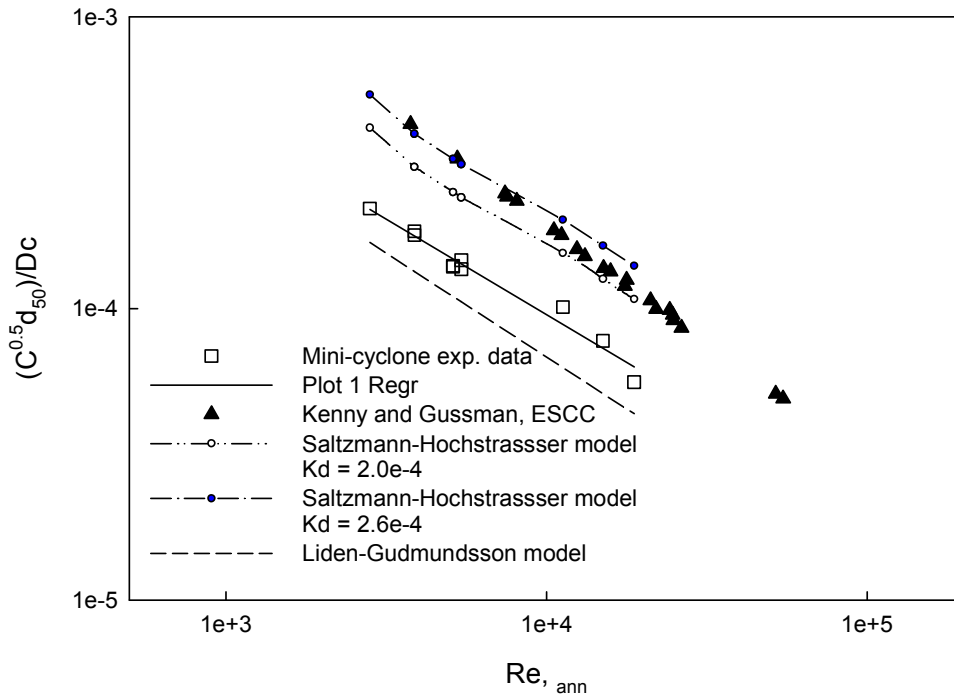
Figure 4. Dimensionless cutoff size ($C^{0.5}d_{50}/D_c$) vs. annular flow Reynolds number for the mini-cyclones and ESCC, and from the prediction from the Saltzmann-Hochstrasser and Liden-Gudmundsson models

For comparison, the predictions using the Saltzman-Hochstrasser and the Liden-Gudmundsson models are also included in Fig. 4. The correlation given in these two models result in similar predictions. The Saltzman-Hochstrasser model uses the outlet tube Reynolds number instead of the annular flow Reynolds number, and the Liden-

Gudmundsson model has an additional parameter of S/D_c. The correlations given in the Saltzman-Hochstrasser and Liden-Gudmundsson models are listed herein for reference:

(1) Saltzman-Hochstrasser model:

$$\log\left(\frac{d_{50}}{D_c}\right) = \log(K_d) - 0.713\log(\mathrm{Re}_{out}), \; K_d=2.0e4{\sim}2.6e4$$

(2) Liden-Gudmundsson model:

$$\ln\left(\frac{C^{0.5}d_{50}}{D_c}\right) = \ln(0.0414) - 0.713\ln(\mathrm{Re}_{ann}) - 0.172\ln\left(\frac{S}{D_c}\right)$$

We also include the data for ESCC cyclones in Fig. 4 because of the similar cyclone shape in ESCCs and the prototypes. The ESCC data were reproduced from the empirical equation and the test conditions given by Kenny and Gussman (2000). As seen in Fig. 4, the data calculated by the Saltzman-Hochstrasser model with the constant k_d of 2.6 $\times10^{-4}$ are at the upper bound of all the data sets, and reasonably characterize the performance of the ESCC family. The prediction of the Liden-Gudmundsson model is, however, located at the lower bound of all shown data. The data for prototype mini-cyclones were set between these two data bounds. The linear regression coefficients of the prediction by the above-mentioned models, and the data sets for ESCC and prototype mini-cyclones, are given in Table 3. Note that the slope (1st order coefficient) of linear regression varies slightly, but the interception constants vary considerably.

In addition to $d_{p,50}$, the pressure drop across mini-cyclones is the other key performance parameter. Fig. 5 shows the experimental data of the cyclone pressure drop as a function of the sampling flow rates. At the design flow rate (0.3 lpm) the pressure

drops are 1.8 and 20.0 inH$_2$O for 1.0-µm and 0.3-µm mini-cyclone, respectively. The mini-cyclone pressure drop increases quadratically with the sampling flow rate. By converting the sampling flow rate to the inlet velocity, the two pressure drop curves collapse into one (shown in Fig. 6). The pressure drop of mini-cyclones can therefore be modeled by the inlet dynamic pressure ($\rho_g V_i^2/2$) multiplied by a dimensionless loss coefficient (K_L). The fitted K_L values for the mini-cyclones range from 2.12 to 2.43.

Table 3. Regression coefficients for the correlation between dimensionless particle size and the annular flow Reynolds number

$$\log\left(\frac{C^{0.5}d_{50}}{D_c}\right) = b_0 + b_1 \times \log(\text{Re}_{ann})$$

	b_0	b_1
mini-cyclone	-1.398	-0.6556
ESCC	-0.469	-0.8108
Saltzman-Hochstrasser model Kd=2.0e4	-0.980	-0.6731
Saltzman-Hochstrasser model Kd=2.6e4	-1.094	-0.6731
Liden-Gudmundsson model	-1.317	-0.7125

5.2 Pressure Drop across Prototype Mini- cyclones
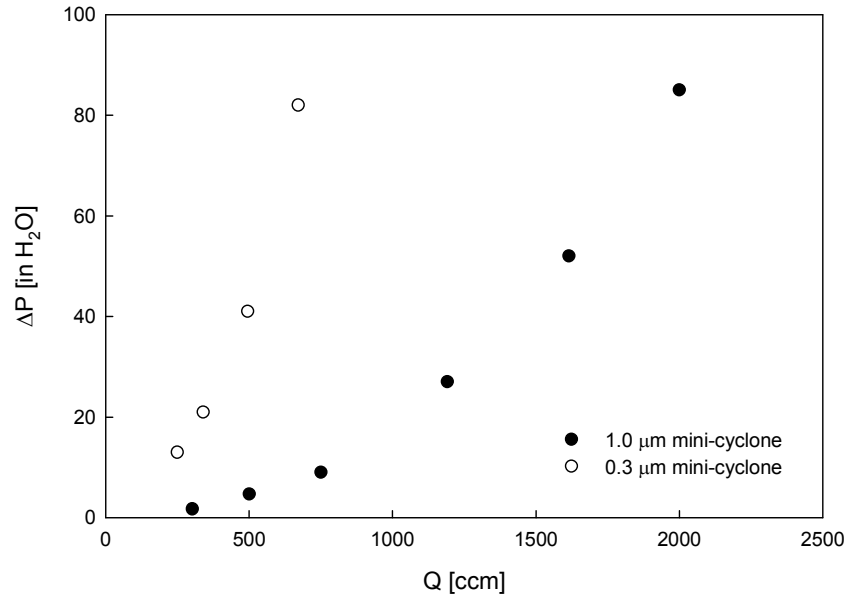
Figure 5. Pressure drop as a function of sampling flow rate for the prototype mini-cyclones
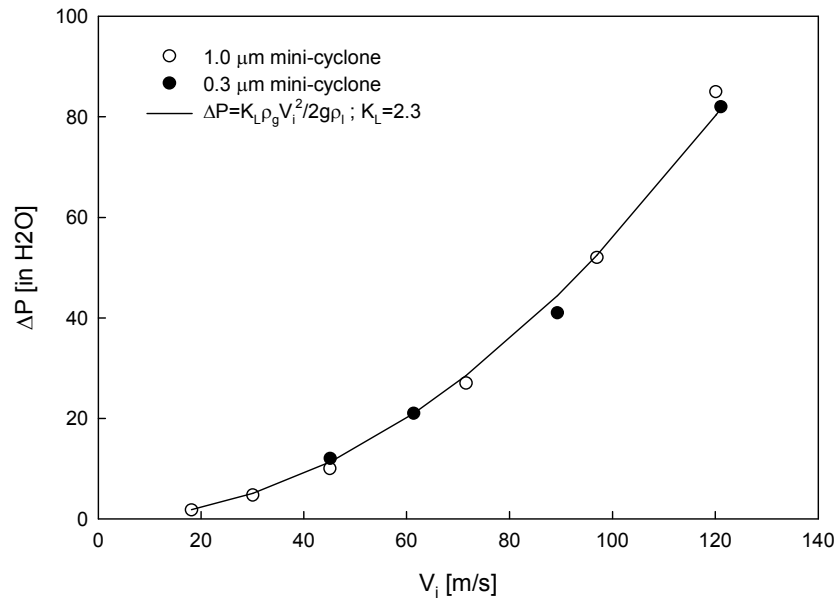
Figure 6. Mini-cyclone pressure drop as a function of inlet velocity

Several models for the prediction of cyclone pressure drop have been proposed (Shepherd and Lapple, 1940; Alexander 1949; First 1949; Stairmand 1949; Barth 1956; Casal 1983; Dirgo 1988; Avci and Karagoz 2005; and Chen and Shi 2007). In this study, the Dirgo and the Chen-Shi models were used to calculate the value of K_L because of their accuracy over a wide range of cyclone designs. The Dirgo model was developed by statistically correlating the pressure drop with cyclone dimension ratios. The coefficient and exponents of the fitted equations were determined through statistical analysis of pressure drop data for 98 cyclones with a variety of designs. However, the loss coefficient should not be only a function of cyclone dimension ratios. It should also be related to the surface roughness and operating conditions (e.g., inlet velocity). Chen and Shi (2007) theoretically analyzed the cyclone pressure drop from fluid dynamics. The Chen-Shi model estimates K_L by summing up four partial coefficients from different flow aspects: (1) the flow expansion at the cyclone inlet (K_{L1}); (2) the flow contraction at the entrance of the cyclone outlet (K_{L2}); (3) the frictional loss, including the swirling loss due to the friction between the gas flow and the cyclone wall (K_{L3}); (4) the dissipation loss of the gas dynamic energy in the cyclone outlet (K_{L4}). This model considers more details of the flow field in the cyclone and allows us to examine the pressure drop in different parts of a cyclone. The final working equations of the Dirgo and Chen-Shi models are given as follows:

(1) Dirgo Model

$$K_L = 19.7 \left(\frac{a \cdot b}{D_e^2} \right)^{0.99} \times \left(\frac{S}{D_c} \right)^{0.35} \times \left(\frac{H}{D_c} \right)^{-0.34} \times \left(\frac{h}{D_c} \right)^{-0.35} \times \left(\frac{B}{D_c} \right)^{-0.33}$$

(2) Chen-Shi model

$$K_L = K_{L1} + K_{L2} + K_{L3} + K_{L4},$$

$$K_{L1} = \left(1 - \frac{2k_i\tilde{b}}{1 + 1.33\tilde{b} - \tilde{d}_r}\right)^2,$$

$$K_{L2} = \frac{4.5 \cdot \left(1 - 3\tilde{d}_r^2\right)}{K_A^2},$$

$$K_{L3} = 1.11 f_0 K_A \tilde{F}_S \tilde{V}_{\theta w}^3 \tilde{d}_r^{-1.5n}, \text{ and}$$

$$K_{L4} = \frac{\tilde{V}_{\theta w}^2}{\left(\tilde{r}_c \tilde{d}_r\right)^n} + \frac{1}{K_A^2 \left(\tilde{d}_r^2 - \tilde{r}_c^2\right)^2},$$

where

$$\tilde{r}_c = 0.38\tilde{d}_r + 0.5\tilde{d}_r^2,$$

$$\tilde{V}_{\theta w} = \frac{1.11 K_A^{-0.21} \tilde{d}_r^{0.16} \text{Re}_{out}^{0.06}}{1 + f_0 \tilde{F}_S \sqrt{K_A \tilde{d}_r}}, \text{ and}$$

$$n = 1 - \exp\left[-0.26 \text{Re}_{out}^{0.12}\left(1 + \left|\frac{S-a}{b}\right|\right)^{-0.5}\right].$$

Since the inlet of the mini-cyclone is smaller than the diameter of the sampling tube, flow contraction is expected at the entrance. An additional term taking into account of such a flow contraction effect was therefore added to the above models:

$$K_0 = 0.5 \cdot \left(1 - A_i / A_{tube}\right).$$
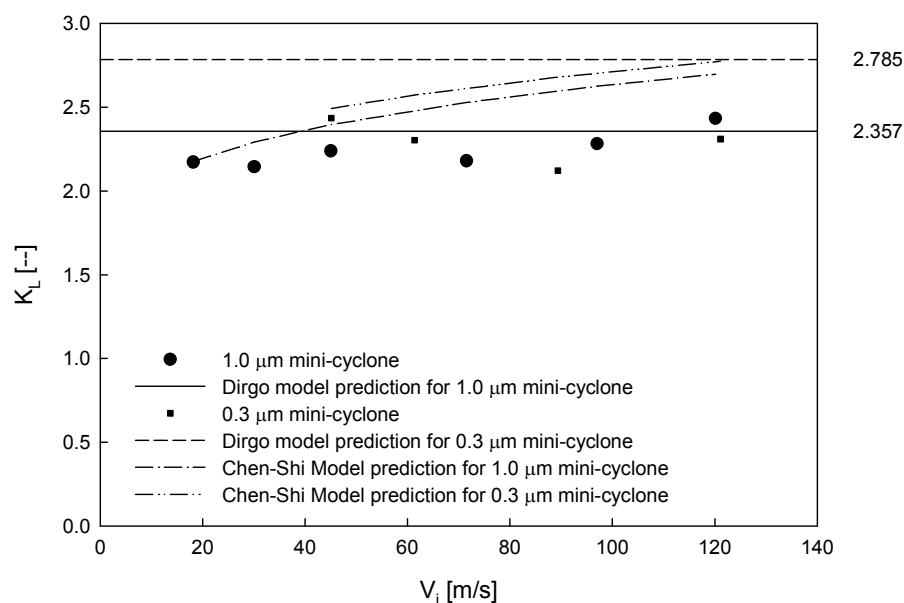
Figure 7.　　Comparison of the loss coefficient (K_L) as a function of inlet velocity for mini-cyclones, predicted by the Dirgo and Chen-Shi models

As shown in Fig. 7, the K_L value of mini-cyclones can be reasonably estimated by both models. Different predictions from Dirgo's model are due to the slightly different dimension ratios of the two mini- cyclones. For Dirgo's model, the K_L values do not vary with the inlet aerosol velocity. On the other hand, the K_L predicted by the Chen-Shi model monotonically increases with the increase of inlet velocity, because the swirling loss in a cyclone and the dissipation loss in the outlet are related to the flow Reynolds number.

The K_L value for the Stairmand and SRI I cyclones were also estimated using two theoretical models at the same inlet velocity and sampling flow rate operation conditions. The dimension ratios for all the compared cyclones, needed for the pressure drop prediction, are given in Table 4. Together with those of mini-cyclones, the estimated loss coefficients of the Stairmand and SRI I cyclones are presented in Table 5. Among all

187

three cyclone designs, the prototype mini-cyclones have the smallest K_L value under both

the same sampling flow rate and inlet velocity conditions. Further, the K_L values of mini-

cyclones are generally low compared with the experimental K_L data collected by Dirgo

(1988).

Table 4. Dimensional ratios for the mini-cyclones, SRI I cyclone, and Stairmand cyclone

Model	Dc	D_{in}/Dc	De/Dc	S/Dc	H1/Dc	H/Dc	B/Dc	Db/Dc	Hb/Dc
	[in]	[--]	[--]	[--]	[--]	[--]	[--]	[--]	[--]
Mini-cyclone	0.188	0.125	0.245	0.4	1.667	1.667	1	--	--
SRI I	0.188	0.284	0.336	0.351	0.501	1.555	0.421	0.996	0.503

Model	Dc	a/Dc	b/Dc	De/Dc	S/Dc	H1/Dc	H/Dc	B/Dc
	[m]	[--]	[--]	[--]	[--]	[--]	[--]	[--]
Stairmand	0.188	0.5	0.2	0.5	0.5	1.5	4	0.375

By comparing all the partial K_L values calculated by the Chen-Shi model, it is

found that the inlet expansion loss contributes the largest portion of the total K_L for the

mini-cyclones, while the energy dissipation loss in the outlet dominates over other losses

for the other two types of cyclone design. The comparison also indicats that the energy

dissipation loss in the cyclone outlet results in the major difference in the total K_L values,

not the cyclone inlet expansion loss.

Table 5(a). The loss coefficient K_L estimated by the Chen-Shi model and Dirgo model for the mini-cyclone, SRI I cyclone, and Stairmand cyclone under the same inlet velocity

Model	K_{Dirgo}	K_{C-S}*	K_{L1}	K_{L2}	K_{L3}	K_{L4}
	[--]	[--]	[--]	[--]	[--]	[--]
Mini-cyclone	2.0754	1.8942	0.8114	0.0009	0.4580	0.6239
SRI I	11.2392	4.1624	0.5526	0.0194	0.5554	3.0350
Stairmand	4.6707	3.9109	0.7112	0.0182	0.6835	2.4980

*($K_{c-s} = K_{L1} + K_{L2} + K_{L3} + K_{L4}$)

Table 5(b). The loss coefficient K_L estimated by the Chen-Shi model and Dirgo model for the mini-cyclone, SRI I cyclone, and Stairmand cyclone under the same sampling flow rate

Model	K_{Dirgo}	K_{C-S}	K_{L1}	K_{L2}	K_{L3}	K_{L4}
	[--]	[--]	[--]	[--]	[--]	[--]
Mini-cyclone	2.0754	1.8926	0.8114	0.0009	0.4572	0.6231
SRI I	11.2392	3.3700	0.5526	0.0194	0.3738	2.4242
Stairmand	4.6707	3.0679	0.7112	0.0182	0.4303	1.9082

$*(K_{c-s} = K_{L1} + K_{L2} + K_{L3} + K_{L4})$

6. Summary

Two prototype mini-cyclones with cutoff particle sizes at the 50% penetration of 1.0 and 0.3 μm, respectively, and an aerosol flow rate of 0.3 lpm have been developed as size-selective inlets for miniature particle detectors. The pressure drops of the designed mini-cyclones are 1.8 and 20 inH$_2$O at the flow rate of 0.3 lpm. The physical sizes of these mini- cyclones are both less than a US quarter coin, perfect for inclusion in miniature particle detectors. Two experimental setups were used to evaluate the performance of the prototype mini-cyclones for a wide particle size range. One setup was for the testing of sub-micrometer particles and the other for super-micrometer particles. For the sub-micrometer particle testing, a homemade Collison atomizer was used to produce KCl particles and a TSI SMPS was applied to measure the particle size distributions upstream and downstream of the mini-cyclones. For the case of super-micrometer particles an ultrasonic nebulizer was utilized to generate super-micron KCl particles, and a TSI APS was used for particle size distribution measurements.

The experimental data collected on the 50% cutoff particle size at different cyclone-operation flow rates show that the performance of mini-cyclones can be better

interpreted by the correlation between the dimensionless cutoff size and the annular flow Reynolds number, rather than that between the Stokes number and the cyclone body Reynolds number. The above conclusion is consistent with the findings reported in previous studies for small cyclones (Moore and McFarland, 1993; and Liden and Gudmundsson, 1997). An empirical model for the prediction of cutoff particle size for mini-cyclones was thus established, which can be applied to design other mini-cyclones with the same dimension ratios. Collected cutoff particle size data under different mini-cyclone flow operations were also compared with those calculated by two other generalized cyclone models (the Saltzman-Hochstrasser model and the Liden-Gudmundsson model). It was found that none of these previous models could well predict the performance (i.e., the cutoff particle size at 50% penetration) of mini-cyclones. However, the prediction of these two models could serve as a reference to design a new small cyclone in the reported Reynolds number range.

A simple analysis shows that the pressure drop across mini- cyclones can be characterized by the inlet dynamic pressure drop ($\rho_g V_i^2/2$) multiplied by a dimensionless loss coefficient, K_L. The experimental K_L value of the mini-cyclones is around 2.12 to 2.43. The K_L value for the mini-cyclones can be reasonably estimated by the statistical model given by Dirgo (1988) and the theoretical model proposed by Chen and Shi (2007). For comparison, the K_L values of Stairmand and SRI I cyclones were also estimated by the Chen-Shi models. It was found the mini-cyclones have the lowest K_L for both the same flow rate and inlet velocity conditions. The K_L values of mini-cyclones are also considered low in comparison with the experimental K_L data collected in the Dirgo's cyclone database.

In addition to the cutoff size and pressure drop, the loading capacity is another important characteristic parameter of cyclone. Since the small size of the mini-cyclone, the loading capacity is expected to be limited. However, during the study, the performance of the mini-cyclone remains constantly stable under the challenging concentration of 10^4 particles/cm^3 for 60 minutes. In the next stage, the mini-cyclones will be tested for extended period (up to 8 hours) and study their loading capacity and loading behavior.

7. References

Alexander, R. M. (1949) Fundamentals of cyclone design and operation. *Aust. Inst. Min. Met. Proc*. 152-3:203-228.

Barth, W. (1956) Design and layout of the cyclone separator on the basis of new investigations. *Brennstoff-Warme-Krafat*. 8:1-9.

Beeckmans, J. M. and Kim, C. J. (1977) Analysis of the efficiency of reverse flow cyclones. *Can. J. Chem. Engng*. 55:640-643.

Casal, J. and Martinez-Benet, J. M. (1983) A better way to calculate cyclone pressure drop. *Chem. Engng*. 1:99-100.

Chan, T. and Lippmann, M. (1977) Particle collection efficiencies of air sampling cyclones: an empirical theory. *Environ. Sci. Technol*. 11:377-382.

Chen, J. and Shi, M. (2007) A universal model to calculate cyclone pressure drop. *Powder Technol*. 171:184-191.

Dietz, P. W. (1981) Collection efficiency of cyclone separators. *AIChE J*. 27:888-892.

Dirgo, J. (1988) Relationships between cyclone dimensions and performance. PhD Thesis, Harvard University, Cambridge, MA.

Dring, R. P. and Suo, M. (1978) Particle trajectories in swirling flows. *J. Energy*. 2:232-237.

Edwards, R., Johnson, M., Dunn, K.H., and Naeher, L.P. (2005) Application of real-time particle sensors to help mitigate exposures of wildland firefighters. *Arch. Environ. Occup. Health*. 60(1):40-43.

First, M. W. (1949) Cyclone dust collector design. *Am. Soc. Mech. Eng*. 49:127-132.

Görner, P., Wrobel, R., Mička, V., Škoda, V., Denis, J., and Fabriès, J. F. (2001) Study of fifteen respirable aerosol samplers used in occupational hygiene. *Ann. Occup. Hyg*., 45:43–54.

Iozia, D. L. and Leith, D. (1989) Effect of cyclone dimensions on gas flow pattern and collection efficiency. *Aerosol Sci. Technol*. 10:491–500.

Karagoz, I. and Avci, A. (2005) Modelling of the Pressure Drop in Tangential Inlet Cyclone Separators. *Aerosol Sci. Technol*. 39:857–865.

Kenny, L. C. and Gussman, A. (1997) Characterization and modelling of a family of cyclone aerosol preseparators. *J. Aerosol Sci*. 28:677-688.

Kenny, L. C. and Gussman, A. (2000) A direct approach to the design of cyclones for aerosol-monitoring applications. *J. Aerosol Sci*. 31:1407-1420.

Lapple, C. E. (1950) Gravity and centrifugal separation. *Ind. Hyg. Quart*. 11:40-48.

Leith, D. and Licht, W. (1972) The collection efficiency of cyclone type particle collectors. *AIChE Sym*. Ser. 68:196-206.

Lidén, G. and Gudmundsson, A. (1997) Semi-empirical modelling to generalise the dependence of cyclone collection efficiency on operating conditions and cyclone design. *J. Aerosol Sci*. 28:853-874.

Moore, M. E. and McFarland, A. R. (1990) Design of Stairmand-Type Sampling Cyclones. *Am. Ind. Hyg. Ass. J*. 51:151-159.

Moore, M. E. and McFarland, A. R. (1993) Performance modeling of single-inlet aerosol sampling cyclones. *Environ. Sci. Technol*. 27:1842-1848.

Moore, M. E. and McFarland, A. R. (1996) Design methodology for multiple inlet cyclones. *Environ. Sci. Technol*. 30:271-276.

Mothes, H. and Löffler, F. (1988) Prediction of Particle Removal in Cyclone Separators. *Int. Chem. Engng*. 28:231-240.

Overcamp, T. J. and Scarlett, S. E. (1993) Effect of Reynolds number on the Stokes number of cyclones. *Aerosol Sci. Technol*. 19:362–370.

Qi; C., Chen; D. R., and Greenberg, P. (2008) Fundamental study of a miniaturized disk-type electrostatic aerosol precipitator for a personal nanoparticle sizer. *Aerosol Sci. Technol*. 42:505–512.

Saltzmann, B. E. and Hochstrassser, J. M. (1983) Design and performance of miniature cyclones for respirable aerosol sampling. *Environ. Sci. Technol*. 17:418-424.

Saltzmann, B. E. (1984) Generalized performance characteristics of miniature cyclones for atmospheric particulate sampling. *Am. Ind. Hyg. Assoc. J*. 45:671-680.

Shepherd, C. B. and Lapple, C. E. (1939) Flow pattern and pressure drop in cyclone dust collectors. *Ind. Eng. Chem*. 31:972-984.

Stairmand, C. J. (1949) Pressure drop in cyclone separators. *Engineering*. 168:409-412.

Curriculum Vita

Ta-Chih Hsiao

EDUCATION

Ph.D.	**Washington University in St. Louis, St. Louis, MO, USA** Dept. of Energy, Environmental and Chemical Engineering Dissertation: Particle Control Technology – Filtration and Separation	**2009**
M.S.	**Stanford University, Stanford, CA, USA** Dept. of Civil and Environmental Engineering	**2003**
B.S.	**National Taiwan University, Taipei, Taiwan** Dept. of Civil Engineering	**1998**

HONORS AND AWARDS

Boeing Fellowship, McDonnell International Scholar Academy, U.S.A   **2006**

The Forest E. McGrath Scholarship, Washington University in St. Louis   **2004**

PROFESIONAL SOCIETIES

☐ American Association for Aerosol Research (AAAR)

☐ Air & Waste Management Association (AWMA)

☐ American Society of Civil Engineers (ASCE)

PUBLICATIONS

Accepted Journal Articles

Hsiao, T.C.; Chen, D.R. and Sang Young Son, Development of Mini-Cyclones as the Size-Selective Inlet of Miniature Particle Detectors, *Journal of Aerosol Science,* accepted, 2009.

Hsiao, T.C. and Chen, D.R., Performance of Filters When Loaded with NaCl and KCl Particles at Low Relative Humidity Environment, *Filtration*, accepted, 2009.

Chen, L.Y.; Jeng, F.T.; Chen, C.C.; **Hsiao, T.C.**, Hygroscopic behavior of atmospheric aerosol in Taipei, *Atmospheric Environment,* 2003, 37, 2069–2075.

Journal Articles Submitted or in Preparation

Hsiao, T.C., Chen, D.R., Street, K. W. and Greenberg, P., Development of a Multi-stage Axial Flow Cyclone, *Aerosol Science and Technology*, submitted, 2009.

Hsiao, T.C., Chen, D.R., Li, L., Street, K. W. and Greenberg, P., Effect of Geometric Configuration on the Collection Efficiency of Axial Flow Cyclones, *Particle and Particle System Characterization*, submitted, 2009.

Hsiao, T.C. and Chen, D.R., Filter Loading Behavior for Cellulose Filter Loaded with Supermicron Liquid Coated Particle, in preparation, 2009.

Hsiao, T.C. and Chen, D.R., The Effect of Surface Property on Filter Loaded with Submicron Liquid Coated Particle, in preparation, 2009.

Conference Proceedings and Presentations (presenter)*

Hsiao, T.C.* and Chen, D.R., Development of a Mini-Cyclone for Miniaturized Particle Devices, *AAAR Conference*, Orlando, FL, 2008.

Hsiao, T.C.* and Chen, D.R., Filter Loading Characteristics of Supermicron Liquid-Coated Particles, *AAAR Conference*, Orlando, FL, 2008.

Hsiao, T.C.* and Chen, D.R., Development of a Multi-stage Axial Cyclone for Dust Separation, *AFS conference,* Valley Forge, PA, Mar. 2008.

Hsiao, T.C.* and Chen, D.R., Low Efficiency Filter Performance in the Low Humidity Environment, *AFS conference,* Valley Forge, PA, Mar. 2008.

Hsiao, T.C.* and Chen, D.R., Filter Performance under the Liquid-Coated Particle Loading, *AFS conference proceeding,* Orlando, FL, Mar. 2007 / *AAC conference*, Kaoshung, Taiwan, 2007.

Hsiao, T.C.* and Chen, D.R., Effect of Relative Humidity on the Performance of Filters Loaded with Supermicron-Sized Sodium Chloride Particles, *IAC conference*, St. Paul, MN, 2006.

Hsiao, T.C.* and Chen, D.R., Neutralization of Charges on Electric Filter Media Fibers by Bipolar Ions, *AAAR Conference*, Austin, TX, 2005.